



1-1-2015

Nanophotonics of 2-Dimensional Materials

Jason C. Reed

University of Pennsylvania, jasreed@seas.upenn.edu

Follow this and additional works at: <http://repository.upenn.edu/edissertations>

 Part of the [Mechanics of Materials Commons](#)

Recommended Citation

Reed, Jason C., "Nanophotonics of 2-Dimensional Materials" (2015). *Publicly Accessible Penn Dissertations*. 1965.
<http://repository.upenn.edu/edissertations/1965>

This paper is posted at ScholarlyCommons. <http://repository.upenn.edu/edissertations/1965>
For more information, please contact libraryrepository@pobox.upenn.edu.

Nanophotonics of 2-Dimensional Materials

Abstract

2-Dimensional materials are of great interest because of novel and intriguing properties that emerge at the monolayer limit in comparison to bulk materials. To that end, this thesis is split into the study of two different 2-dimensional materials in the realm of nanophotonics. First, graphene is utilized for both passivating the surface of metallic nanoparticles from oxidation and as a platform for functionalization and integration into specific molecule sensing. The nanoparticles act as plasmonic nanoantennas, enhancing the electric field near the surface of the antenna. It is shown that graphene-encapsulated silver nanoantennas are oxidation resistant and optically stable over a 30 day period. The performance of the graphene-passivated silver nanoantennas outpaces that of the traditional material, gold, by ~60% in sensing bulk index changes in the range of $n = 1.40$ to 1.45 . Graphene encapsulation can be extended to other plasmonic metals such as aluminum and copper, as well as fully integrate graphene-passivated Ag nanoantennas into biomolecular sensing devices. The second topic of this thesis is to study and enhance the luminescence of molybdenum disulfide (MoS₂), a 2-dimensional semiconductor. Atomic layer deposition of SiO₂ was used to encapsulate and then effectively etch a layer of bilayer MoS₂ through reactive processes, which result in a chemically-doped MoS₂ monolayer with enhanced luminescence properties. This new enhanced layer is two orders of magnitude more luminescent than the original material and one order of magnitude over that of an exfoliated monolayer. By coupling the enhanced MoS₂ to an optical microdisk cavity, highly narrow emission can be produced from the original, broad luminescence. These sharp peaks can be utilized in biomolecule sensing through functionalization of the MoS₂ layer. The effects of high-intensity optical pumping of the MoS₂ in these microdisk cavities are also studied. Heat generation from non-radiative recombination causes thermally enabled oxidation of the optical material. This effect is shown to be not limited to MoS₂, but affects WSe₂ as well. This effect is shown to be minimized through the use of pulsed excitation, and the luminescence from high Q-factor microdisks was investigated using high-fluence femtosecond optical pulses.

Degree Type

Dissertation

Degree Name

Doctor of Philosophy (PhD)

Graduate Group

Materials Science & Engineering

First Advisor

Ertugrul Cubukcu

Subject Categories

Mechanics of Materials

NANOPHOTONICS OF 2-DIMENSIONAL MATERIALS

Jason C Reed

A DISSERTATION

in

Materials Science and Engineering

Presented to the Faculties of the University of Pennsylvania

in

Partial Fulfillment of the Requirements for the

Degree of Doctor of Philosophy

2015

Supervisor of Dissertation

Ertugrul Cubukcu, Assistant Professor, Materials Science and Engineering

Graduate Group Chairperson

Shu Yang, Professor, Materials Science and Engineering

Dissertation Committee

Ritesh Agarwal, Professor, Materials Science and Engineering

Nader Engheta, Professor, Electrical and Systems Engineering

Christopher B. Murray, Professor, Materials Science and Engineering, Chemistry

DEDICATION

To my parents, without whom I would have never come this far.

ACKNOWLEDGMENTS

Prof. Ertugrul Cubukcu, my advisor. First and foremost, I would like to thank my Ph.D. advisor and mentor. The guidance and support that you gave me during the course of my study is what made this work possible. The freedom, trust, and willingness to try new things that you gave me were what made this research exciting and worthwhile. Building up a new lab with you (and sadly bringing it to a close at Penn) was an invaluable experience and has helped me develop a myriad of skills and experience. The things that you have taught me will be the basis of all of my future endeavors, and I am truly grateful for them.

Profs. Ritesh Agarwal, Christopher Murray, and Nader Engheta, my thesis committee. Thank you for taking the time out of all of your very busy schedules to help oversee the research direction of my Ph.D. The many helpful discussions over the course of my study gave insight to many different aspects of my Ph.D. work and experience.

Prof. Shu Yang, my former mentor and current graduate group chair. Thank you for responding to the email of an inexperienced freshman undergraduate and allowing me to whet my research appetite. Without such a positive first experience with research, I may not have gone down this path. You gave me a chance and believed in my ability that has encouraged me this entire way.

Prof. Ju Li, former graduate group chair. You helped me with guidance and support during my first year as a graduate student. No matter was too small to discuss with you personally and I truly appreciated that.

Yutong Zhu, (Justin) Hai Zhu, Fei Yi, Stephanie Malek, Euijae Shim, Qiushi Guo, Guanqing Hao, and Yichen Lu; my group-mates. Thank you all for support on my projects and for making the research group the interesting place it was. Many discussions about research as well as all topics of life were had and led to a simulating environment of work and friendship.

Iulian Cordreanu, Kyle Keenan, Hiro Yamamoto, Eric Johnson, Charlie Veith, Gerald Lopez, and Meredith Metzler; the cleanroom staff. A great deal of my work over the years was in the cleanroom and you all helped keep things working smoothly. Thank you for all the support you all have given me.

Noah Clay, director of the Nanofab. Along with the rest of the cleanroom staff, I would like to acknowledge the resources afforded to support the research I have undertaken these years. Additionally, I would like to thank you for pertinent professional discussions and opportunities that you have afforded me that have been of the utmost importance to my professional development.

Pat Overend, Vicky Lee, and Irene Clements; the MSE staff. I would like to thank all three of you for making this department feel like home for myself and all the other students. You looked out for us as if we were family and supported us with all the small things that can easily become overwhelming. The dynamic of this department would not be nearly as welcoming without you all.

Jamie Ford, Matt Brukman, and Steve Szewczyk; research staff. Thank you for training me and keeping all the tools needed for my research up and running. Although it may have been hard to find some of you (Steve), you were all willing to help out whenever needed.

Fred Helmig and Rico Vargas, the LRSM building managers. Thank you to both of you for managing the facilities at the LRSM, where many of the facilities and labs are located in which I performed my research.

Robert Ferrier, Michael O'Reilly, Carlos Aspetti, Kate Murphy, Vicky Doan-Nguyen Pavan Nukala, Lisa Chen, Brian Piccione, David Kim, and Chi-Mon Chen; my MSE and CBE upperclassmen. You all helped welcome me and serve as, in one way or another, mentors for a range of topics from life in Philadelphia to advice in coursework and qualification exams. Thank you for making this department as fun and welcoming as it has been.

Robert Middleton, Frank Streller, Nicholas Greybush, Jacob Berger, Daksh Agarwal, Dan Magagnosc, (Cathy) Han-Chang Yang, Emmabeth Parrish, Danny Strickland, Spencer Thomas, Ted Trigg, Boris Rasin, Nadia Krook, James Pressley, and Luke Shi; my MSE underclassmen. I want to thank you all for the sense of community and enlightening conversations that I've had with all of you.

Ashley Gaulding, Sharon Sharick, Ryan Wade, (Jim) Chia-Chun Lin, (Walter) Wei-Shao Tung, Jiechang Hou, Joohee Park, Eric Wong, Amber Sexton, Roshni Thomas, Øydis Gadeholt, Jason Wang, Nicholas Chen, and Nathaniel Berry, my classmates and cohorts. We all started graduate school together and pressed through the fiery crucible that is first year courses. We spent many hours working together and many hours in each other's company in less academic settings as well. You all are the defining group of people that have made the Ph.D. experience what it was, and I thank you all for that.

Elaine Lee and Rahul Agarwal, my closest companions. You two have been my closest companions throughout the entire Ph.D. process and I could not have completed it without the support and friendship that we have developed along the way. I want to thank you two especially for the great conversations about research, coursework, and life in general.

My mom, dad, and brother. Lastly, I would like to thank my family as you have been the support from the day I was born and I know I will have your support in all my endeavors in life.

ABSTRACT

NANOPHOTONICS OF 2-DIMENSIONAL MATERIALS

Jason C Reed

Ertugrul Cubukcu

2-Dimensional materials are of great interest because of novel and intriguing properties that emerge at the monolayer limit in comparison to bulk materials. To that end, this thesis is split into the study of two different 2-dimensional materials in the realm of nanophotonics. First, graphene is utilized for both passivating the surface of metallic nanoparticles from oxidation and as a platform for functionalization and integration into specific molecule sensing. The nanoparticles act as plasmonic nanoantennas, enhancing the electric field near the surface of the antenna. It is shown that graphene-encapsulated silver nanoantennas are oxidation resistant and optically stable over a 30 day period. The performance of the graphene-passivated silver nanoantennas outpaces that of the traditional material, gold, by ~60% in sensing bulk index changes in the range of $n = 1.40$ - 1.45 . Graphene encapsulation can be extended to other plasmonic metals such as aluminum and copper, as well as fully integrate graphene-passivated Ag nanoantennas into biomolecular sensing devices. The second topic of this thesis is to study and enhance the luminescence of molybdenum disulfide (MoS_2), a 2-dimensional semiconductor. Atomic layer deposition of SiO_2 was used to encapsulate and the effectively etch a layer of bilayer MoS_2 through reactive processes, which result in a chemically-doped MoS_2 monolayer with enhanced luminescence properties. This new enhanced layer is two orders of magnitude more luminescent than the original material and one order of magnitude over that of an exfoliated monolayer. By coupling the enhanced MoS_2 to an

optical microdisk cavity, highly narrow emission can be produced from the original, broad luminescence. These sharp peaks can be utilized in biomolecule sensing through functionalization of the MoS₂ layer. The effects of high-intensity optical pumping of the MoS₂ in these microdisk cavities are also studied. Heat generation from non-radiative recombination causes thermally enabled oxidation of the optical material. This effect is shown to be not limited to MoS₂, but affects WSe₂ as well. This effect is shown to be minimized through the use of pulsed excitation, and the luminescence from high Q -factor microdisks was investigated using high-fluence femtosecond optical pulses.

TABLE OF CONTENTS

ACKNOWLEDGMENTS	iii
ABSTRACT	vi
LIST OF FIGURES	x
CHAPTER 1: Introduction and Background	1
1.1 Introduction and Outline	1
1.2 Localized Surface Plasmon Resonance (LSPR) in Metals	2
1.3 Graphene	11
1.4 Whispering Gallery Mode Optical Microcavities	20
1.5 2D Transition Metal Dichalcogenides	27
1.6 References	33
CHAPTER 2: Graphene-Enabled Silver Nanoantenna Sensors	38
2.1 Introduction	39
2.2 Results and Discussion	40
2.3 Conclusions	55
2.4 References	56
CHAPTER 3: Wavelength Tunable Microdisk Cavity Light Source with a Chemically Enhanced MoS₂ Emitter	59
3.1 Introduction	59
3.2 Theoretical Analysis of Microdisk Design	62
3.3 Results and Discussion	65
3.4 Conclusions	78
3.5 References	79
CHAPTER 4: Cavity-Coupled 2-Dimensional Semiconductors: A Photothermal Analysis	81
4.1 Introduction	81
4.2 Results and Discussion	82

4.3 Conclusions	93
4.4 Methods	94
4.4.1 MoS ₂ & WSe ₂ Exfoliation	94
4.4.2 Microdisk Fabrication	94
4.4.3 Temperature dependent PL Measurement	94
4.5 References	95
CHAPTER 5: Future Directions and Summary	97
5.1 Aluminum and Copper Nanoantennas	97
5.2 Graphene-Enabled Ag Nanoantennas for Protein Sensing	102
5.3 Cavity-Coupled MoS ₂ Microdisks for Protein Sensing	105
5.4 Large Radius, High- <i>Q</i> Microdisk Cavities with CVD-Grown MoS ₂ for High-Fluence Optical Pumping	109
5.5 Summary	120
5.6 References	122
APPENDIX A: List of Publications	123
APPENDIX B: Catalog of Large-Radius MoS₂-Coupled Microdisk Samples	124

LIST OF FIGURES

Figure 1.1 Schematic of the displacement of the free electron cloud in a metal nanosphere relative to the ion core. Reproduced from Ref. ⁴	5
Figure 1.2 (a) Real, denoted ϵ_1 , and (b) imaginary permittivity, denoted ϵ_2 , for Al, Cu, Au and Ag. Reproduced from Ref. ²¹	10
Figure 1.3 A graphene sheet with 2D honeycomb-like lattice can serve as the basis for wrapping into (0D) buckyballs, rolled into (1D) nanotubes, and stacked back into (3D) graphite. Reproduced from: ²⁷	12
Figure 1.4 (a) Transmission spectra for 1 to 4 layers of graphene with the inset showing the transmission at $\lambda=550$ nm. Reproduced from Ref. ³¹ (b) Raman spectrum for both graphite and graphene samples with an excitation wavelength of $\lambda=514$ nm. Reproduced from Ref. ³²	14
Figure 1.5 Ambipolar field effect of graphene, showing decreasing resistivity, ρ , with increasing magnitude of the gate voltage, V_g . The inset shows graphical representations of the Dirac cones and Fermi energy position as a function of positive and negative gate biases as well as the intrinsic case. Reproduced from Ref. ³⁶	16
Figure 1.6 (a-c) A simulation using density functional theory (DFT) to show the reflection of a He atom with 18.6 eV of kinetic energy. Reproduced from Ref. ⁴² (d) Graph showing the permeability of different gas species through different thickness layers of graphite down to monolayer graphene. Reproduced from Ref. ⁴¹	18
Figure 1.7 (a) SEM and (b) high-resolution SEM images of graphene grown on Cu foils with (inset) TEM images of folded monolayer and bilayer graphene edges. (c-d) Images of transferred graphene films onto SiO ₂ /Si and glass substrates. Reproduced from Ref. ⁴⁵	20
Figure 1.8 Schematic of the spontaneous emission of a two-state system in (left) free space and (right) in a coupled cavity showing enhanced spontaneous emission rate. Reproduced from Ref. ⁵⁰	22
Figure 1.9 Eigenmode profiles for a cylindrical cavity for different mode numbers. Azimuthal mode number $m = 1$ for the top row and $m = 15$ for the bottom row. Radial mode increases from $N = 1$ in the leftmost column to $N = 4$ for the rightmost column. Reproduced from Ref. ⁵¹	25
Figure 1.10 SEM image of a micro-toroid optical cavity with Q of 1.00×10^8 . The inset shows the microdisk cavity before CO ₂ laser reflow. Reproduced from Ref. ⁶⁶	27
Figure 1.11 Periodic table showing the different elemental components that for MX ₂ TMDCs. The chalcogenides (S, Se, and Te) The solidly colored elements form layered	

compounds with all of the chalcogenides, while the half colored elements only form layered compounds with one or two of the chalcogenides. About 40 layered TMDC materials exist in this form. Reproduced from Ref.⁵⁴ 28

Figure 1.12 (a) Optical image of templated growth of MoS₂ flakes. The scale bar is 100 μm. (b) a higher magnification image of the MoS₂ flakes in panel (a) with an (inset) AFM scan of one of the flakes showing a sub-nm flake height. Scale bar is 20 μm. Reproduced from Ref.⁶⁵ 29

Figure 1.13 DFT calculations of the electronic band structure for sulfides of Mo and W both in the bulk and at the monolayer. Both bulk cases show a smaller, indirect bandgap, whereas the monolayer materials have a larger direct bandgap. Adapted from Ref.⁵² 30

Figure 1.14 (a) Vibrational modes in MoS₂. (b) Raman spectroscopy of different layer thicknesses of MoS₂ showing the (c) separation of the *E*2*g*1 and *A*1*g* modes as a function of layer thickness. Figure reproduced from Ref.⁵⁷; panel (a) reproduced from Ref.⁵⁸; panel (b-c) reproduced from Ref.⁷⁴ 31

Figure 1.15 (a) Photoluminescence spectra for both monolayer and bilayer exfoliated MoS₂ flakes. The inset shows the quantum yield as a function of number of layers. (b) An SEM image of a WS₂ flake grown through CVD methods. (c) Map of the photoluminescence intensity for the flake in (b). (d) Photoluminescence spectra at different points of the WS₂ flake as denoted in (c). The inset shows the Raman spectra. Scale bar is 5 μm. Adapted from Ref.⁷⁸ and Ref.⁷³ 32

Figure 2.1 (a) Illustration of graphene-passivated Ag nanoantennas fabricated in a square array. The graphene layer prevents the reaction of trace atmospheric H₂S and OCS with the surface of the Ag. (b) Illustration of bare Ag nanoantennas fabricated similarly. The lack of graphene allows the atmospheric sulfur compounds to react with the silver. SEM images of (c) graphene-passivated Ag nanoantennas and (d) bare Ag nanoantennas after 30 days; scale bars are 200 nm. 41

Figure 2.2 Energy dispersive x-ray spectroscopy (EDX) of unpassivated as well as graphene-passivated Ag (Gr-Silver) nanoantennas after 30 days of air exposure. The spectrum for the unpassivated Ag particles shows a sulfur peak from the sulfide formation, whereas such a peak is absent from that of passivated Ag. 43

Figure 2.3 An SEM image of an Ag nanoantennas array covered by graphene (colorized in blue). Statistical cracks in the monolayer film lead to small areas of uncovered nanoantennas (uncolored), where the Ag shows significant morphological changes from the exposure to sulfur compounds. The graphene-covered nanoantennas are protected from this chemical degradation. Partially covered nanoantennas show partial sulfidation. 44

Figure 2.4 An SEM image of an edge of a continuous Ag thin film partially covered by graphene (colorized blue). The area covered by graphene has a smooth edge, while the uncovered (uncolored) area shows the roughness changes through sulfidation. 44

Figure 2.5 Normalized reflection spectra of (a) graphene-passivated Ag and (b) bare Ag nanoantennas over the course of 30 days. Time evolution of the (c) resonance peak position and the (d) resonance peak width for both graphene-passivated and bare Ag nanoantennas over 30 days. 46

Figure 2.6 Optical reflectance spectra of bare Ag and graphene-passivated silver (Ag-Gr) nanoantennas after 30 days in ambient conditions. The slopes ($dI/d\lambda$) show the sensitivity of the array to small shifts. The well preserved Ag-Gr nanoantennas show a 2600% improvement in $dI/d\lambda$ over 30 days. 47

Figure 2.7 SEM Image of a representative transferred graphene layer on top of Ag nanoantennas (left). The cracks in the graphene layer were highlighted (right) and analyzed to be ~2% of the overall area. 48

Figure 2.8 (a) Raman spectra of graphene both on and off of the Ag nanoantenna array, with the relative intensities of the G and 2D bands suggest monolayer graphene. (b) Raman intensity map of the 2D band on the corner of a Ag nanoantennas array, showing the relative enhancement..... 49

Figure 2.9 The sensitivity of both graphene-passivated silver as well as gold nanoantennas arrays of the same dimensions to bulk index changes over a small index range. (a) Experimental data for the change in peak wavelength with index, showing a bulk sensitivity ($d\lambda/dn$) of 241 for Ag-Gr and 186 for bare Au. (b) Theoretical data from FDTD simulations showing a $d\lambda/dn$ of 142 for Ag-Gr and 98 for bare Au. (c) Plot of nearfield intensity profile from FDTD simulations of graphene-passivated silver nanoantennas as a function of position. The local enhancement of the electric field decays exponentially with a constant of 16.5 nm from the surface of the particle..... 51

Figure 2.10 (a) Scattering intensity of Ag oblate spheroids with varying shell thickness of Ag_2S calculated with the MLWA. (b) Scattering peak position as well as peak width derived from the calculated scattering spectra..... 53

Figure 2.11 SEM images of individual silver nanoantennas passivated by graphene (top row) and unpassivated (bottom row) over the course of 30 days. Scale bars are 100 nm.55

Figure 3.1 The $|E|$ for the microdisk (a) on-resonance at $\lambda = 532$ nm and (b) off-resonance at $\lambda = 537$ nm. The two colormaps are of the same scale. (c) A plot showing the spectral dependence of the excitation wavelength on the power absorbed by the MoS_2 flake coupled to the microdisk cavity. Plots of the power absorbed per unit volume of the MoS_2 flake for both the (d) on-resonant $\lambda = 532$ case as well as the (e) off-resonant $\lambda = 537$ case. The colormap scales for these two plots differ by a factor of ~20..... 65

Figure 3.2 (a) SEM image of a MoS₂-coupled microdisk cavity showing a false-colored, tilted view and with low accelerating voltage. The shaded lighter, orange area denotes the area with the MoS₂ flake coverage on the microdisk. Scale bar is 2 μ m. (b) SEM image of the same microdisk with top-down view and with higher accelerating voltage, showing the free-standing portion of the microdisk supported by a silicon pillar. The white dotted area shows the location of the MoS₂. Scale bar is 5 μ m. Field intensity profiles at 664 nm (on resonance) for a (c) perfect 3.8 μ m radius disk as well as a (d) notched disk. (e) FDTD simulations showing dipole excitation at 664 nm and the resulting notch emission from the cavity. (f) A plot from FDTD simulations showing the spectral dependence of the excitation wavelength on the power absorbed by the MoS₂ flake coupled to the microdisk cavity. 67

Figure 3.3 (a) Raman spectroscopy of the MoS₂ E_{2g}¹ and A_{1g} vibrational modes and their separation for monolayer (1L), bilayer (2L). The data plotted in red shows the change in Raman mode separation for enhanced bilayer (E-2L) as a function of added ALD SiO₂. The initially bilayer flake shows a narrowing of the mode separation which approaches the monolayer limit. The inset shows the Raman spectra and mode separation for 2L, 1L as well as E-2L MoS₂. (b) MoS₂ Raman-normalized PL for the E-2L MoS₂ with increasing amounts of ALD SiO₂ added. Here, bare represents data for as-exfoliated bilayer, 2L MoS₂. The data given by the dotted line is the PL for as-exfoliated monolayer 1L MoS₂ as a comparison. The inset shows the Raman-normalized peak intensities as a function of added SiO₂, reaching levels ~2 orders of magnitude larger than the initial values 70

Figure 3.4 (a) Confocal microscope spectroscopy of different areas of the coupled microdisk resonator; flake PL when illuminating and probing the MoS₂ flake (red curve), and notch emission when probing and illuminating the notch in the microdisk (black curve). (b) Histogram showing the quality factor of the modes and their frequency of occurrence across the samples used in this study. (c) Plot of the shift in notch emission peaks with the addition of SiO₂ to fully fabricated MoS₂ coupled microdisks, with a redshift in the spectra of 0.62 nm for each nanometer of SiO₂ added. 72

Figure 3.5 Plot of the free spectral range (FSR) for the different samples used in this study. The error bars represent one standard deviation for modes of the corresponding sample. The small variation across the samples shows relative consistency of the fabrication process. 72

Figure 3.6 This plot shows the FDTD simulation results for the change in the cavity-coupled MoS₂ PL peak as a function of added SiO₂ to the top of the microdisk structure. 73

Figure 3.7 (a) Plot of the PL coupled to a cavity mode showing a FWHM of 2.44 meV corresponding to a coherence length of 440 μ m (b) Calculated electric field intensity profile near the notch 1.0 μ m above the surface of the disk which matches well with a Gaussian fit. The inset shows a dotted orange line which shows the line scan direction relative to the disk from (d). Calculated electric field intensity at (c) the surface of the

disk and (d) 1.0 μm above the disk showing that the far-field radiated optical power originates from the notch. Spatial coherence is determined by the dimension of the notch. 75

Figure 3.8 FDTD simulations of the electric field intensity and PL spot width from a Gaussian source. 2-D FDTD plots of the electric field distribution at (a) the surface of the microdisk, (b) 0.5 μm above and (c) 1.0 μm above the surface. Plots of the horizontal cross section of the spot width at (d) 0.5 μm and (e) 1.0 μm from the surface (orange dotted line on (b) and (c), respectively). 76

Figure 3.9 FDTD simulations of the electric field intensity and PL spot width from a Dipole source. 2-D FDTD plots of the electric field distribution at (a) the surface of the microdisk, (b) 0.5 μm above and (c) 1.0 μm above the surface. Plots of the horizontal cross section of the spot width at (d) 0.5 μm and (e) 1.0 μm from the surface (orange dotted line on (b) and (c), respectively). These plots are analogous to those of Supp. Fig. 3, with the difference in the excitation source. 77

Figure 3.10 Graphs of the intensity of the WGM peaks at different excitation powers shown in (a) linear and (b) logarithmic scales. At these power levels, there is no indication of lasing action in this system. 78

Figure 4.1 (a-b) SEM images of a silicon dioxide microdisk at a tilted and top-down view, respectively. The false-colored purple areas denote the location of the MoS₂. Scale bars are 2 μm . (c) Cavity-coupled emission spectra collected at the microcavity notch as a function of excitation laser power. (d) Peak intensity of the 685 nm cavity mode as the excitation power is cycled to and from 22.8 mW in two consecutive cycles (in order: black squares, red circles, blue upward triangles and purple downward triangles). 83

Figure 4.2 (a) Emission spectra at low power (0.03 mW), at the damage threshold (12.3 mW) and high power beyond the damage threshold (22.8 mW) and the corresponding background PL overlaid. (b) Normalized background PL from panel (a) at the three different power levels. (c) The position of the PL peak wavelength of MoS₂ during heating to and cooling down from elevated temperatures. (d) The evolution of the PL spectra of MoS₂ at different temperatures. Intensity decreases and peak position red shifts with increasing temperature. 85

Figure 4.3 (a) Optical image of a monolayer (1L) WSe₂ flake. (b) Raman and (c) photoluminescence spectra that are characteristic of monolayer WSe₂. (d) The position of the PL peak wavelength of WSe₂ during heating to and cooling down from elevated temperatures. The data is averaged over multiple samples and error bars show standard deviation from the mean, showing reproducibility of the irreversible red shift. 88

Figure 4.4 Graph of the PL spectrum for WSe₂ at increasing temperatures up to 145° C showing a decrease in the overall intensity and red-shift of the main PL peak. 89

Figure 4.5 (a) COMSOL simulation result for 0.55 mW of heating of a silicon dioxide disk of radius 3.8 μm . (lower panel) Heat map of the temperature distribution throughout the microdisk with the heat source confined to the area outlined by the white dotted line. (upper panel) Line scan of the temperature along the horizontal axis of the microdisk. (inset) Cartoon of the microdisk geometry showing the stem radius. (b) Maximum temperature observed in the microdisk of a 2.5 μm stem radius at different absorbed power levels. (c) Maximum temperature observed for a microdisk of varying stem radius and 0.55 mW of absorbed power. 90

Figure 4.6 COMSOL simulation of a GaP photonic crystal membrane 125 nm in thickness with a pitch of 200 nm and hole radius 0.4 times the pitch. 0.55 mW of heat power was applied to the defect and shows a 48.09 K increase in temperature. 91

Figure 4.7 (a) COMSOL simulation result of a microdisk heating at short time scales. The temperature reaches a steady state with a decay time constant of 395 ns. The absorbed power was set to be 0.55 mW with a stem radius of 3.0 μm . (b) Experimental results for the change in temperature in the microdisk after illumination with a pulsed laser excitation of different pulse widths. The change in temperature was measured from the shift in the PL peak position of the MoS_2 on the microdisk. The change in temperature stabilizes with a decay time constant of 184 ns. 93

Figure 5.1 (a) Graph showing how Al particles smaller than 10 nm show fully oxidized particles, whereas particles larger than 10 nm show extended aging with a slow increase in the oxide thickness up to ~ 20 nm particles. Reproduced from Ref. ³ (b) Graph showing the LSPR peak shift with increasing particle oxidation over several months, with the inset showing the calculated peak shift with oxide layer thickness. Reproduced from Ref. ² ... 98

Figure 5.2 Optical spectra of Cu nanoparticles with 0 to 20s (t_1 to t_5) of acetic acid etching. Reproduced from Ref. ⁵ 100

Figure 5.3 (a) Reflection spectra as a function of time and (b) extracted LSPR peak position and width for bare Cu nanoparticles over a 13 day period. SEM images in (c) top down and (d) tilted view of Cu nanoantennas partially covered with monolayer graphene after 2 hours at 200 $^\circ\text{C}$ 101

Figure 5.4 Spectra of graphene-functionalized (a) gold nanoantenna (b) Si nanowire and (c) silver nanoantenna arrays with an A/G binding protein and increasing concentrations of IgG. Reproduced from Ref. ⁶ and Ref. ⁷ 103

Figure 5.5 (a) Top-down and (b) 52 $^\circ$ tilted SEM images of fabricated SiO_2 microdisk cavities with incorporated MoS_2 flakes. The darker, wrinkled portion in panel (a) is the location of the MoS_2 flake. 106

Figure 5.6 Optical spectra of an MoS_2 flake on a flat 285 nm SiO_2/Si substrate before protein functionalization, after binding protein functionalization, and after addition of 100 mM of target protein. 107

Figure 5.7 Cavity-mode emission from the microdisk notch before and after functionalization of the binding protein, as well as after addition of 100 mM of the target protein. Panels (a) and (b) show the same data with an offset in the latter added for clarity.	108
Figure 5.8 Optical image of fabricated large-radius microdisks with transferred CVD-grown MoS ₂ flakes. The sizes of the disks range from 5 to 50 μm in radius.	110
Figure 5.9 Cavity mode emission from CVD-grown MoS ₂ coupled to 10 μm radius microdisk cavities. The MoS ₂ is excited by a 405 nm pulse driven laser diode at 100kHz with a 750 ns pulse width. The power incident at the flake is (a) 0.50 mW and (b) 6.07 mW.	112
Figure 5.10 Magnified view of the optical spectra of presented in Figure 5.9b taken with a higher resolution diffraction grating showing the peak splitting that occurs with the high- Q cavity modes.	113
Figure 5.11 (a) Cavity-mode emission spectra of a 10 μm radius disk at different excitation power levels (in mW). Linear (a,d) and log-scale (c,e) measurement of the intensity vs pump power of the 675.9 nm and 763.6 nm resonant modes, respectively.	114
Figure 5.12 (a) Total emission and (b) emission normalized to the spectrum at 0.016 nJ pulse energy at an 8 MHz pulse repetition rate.	115
Figure 5.13 (a) Total emission and (b) emission normalized to the spectrum at 0.017 nJ pulse energy at an 800 kHz pulse repetition rate.	116
Figure 5.14 (a) Total emission and (b) emission normalized to the spectrum at 0.06 nJ pulse energy at an 80 kHz pulse repetition rate.	116
Figure 5.15 Integrated intensity of emission from notch plotted against pulse power for repetition rates of 80 kHz and 8 MHz.	117
Figure 5.16 Emission spectra from notch for varying pulse power at repetition rates of (a) 8 MHz and (b) 800 kHz. Intensity of peak at (c) $\lambda = 759$ nm and (d) $\lambda = 847$ nm as incident pulse power is varied for both repetition rates of 8 MHz and 800 kHz.	118
Figure 5.17 Spectrum taken from the notch of a different $r = 10$ μm microdisk using a pulse power of 0.25 nJ at a repetition rate of 800 kHz.	119

CHAPTER 1: Introduction and Background

1.1 Introduction and Outline

This dissertation is separated into five chapters and two appendices. **CHAPTER 1**, the current chapter, will discuss the background in the topics of LSPR in metals, graphene, WGM optical cavities, and 2D TMDCs. These topics serve as the basis behind the work presented in the proceeding chapters. **CHAPTER 2** discusses work in top-down fabrication of Ag nanonantennas passivated and enabled by monolayer graphene. These nanoantennas are shown to be chemically stable and retain excellent optical properties. The next two chapters discuss work involving 2D TMDC materials and optical cavities. **CHAPTER 3** reports on fabrication of microdisk optical cavities with chemically enhanced, atomically thin MoS₂ layers. The tunable cavity-coupled emission can reach quality factors of ~ 900 . **CHAPTER 4** investigates the photothermal effects of optical pumping in a microdisk cavity. Material degradation of the MoS₂, as well as WSe₂, is observed, modeled, and ultimately mitigated through pulsed optical excitation. **CHAPTER 5** and its subchapters delineate preliminary work for possible extensions for the preceding three chapters, with each subchapter comprising a different set of preliminary data for each extension. **APPENDIX A** is a list of relevant journal publications either directly or indirectly a result of the work presented in this dissertation. **APPENDIX B** is a catalog of large radius microdisk samples that were fabricated, characterized, and otherwise studied in **Section 5.4**.

1.2 Localized Surface Plasmon Resonance (LSPR) in Metals

Metal nanoparticles have fascinating properties at the nanoscale. Surface plasmons are collective oscillations of the conduction electrons in a metal in response to an electromagnetic (EM) field. Because of the small size of nanoparticles, these surface plasmons can be localized, causing resonances in the optical properties of the particles as well as local near-field electric field enhancements. These properties, their potential applications, and the advances in nanotechnology have made plasmonics a topic of intense study.

The fundamental relationships governing electrodynamics are given by Maxwell's equations:¹

$$\nabla \cdot \mathbf{D} = \rho \quad (1)$$

$$\nabla \cdot \mathbf{B} = 0 \quad (2)$$

$$\nabla \times \mathbf{E} = -\frac{\partial \mathbf{B}}{\partial t} \quad (3)$$

$$\nabla \times \mathbf{H} = \mathbf{j} + \frac{\partial \mathbf{D}}{\partial t} \quad (4)$$

in their “macroscopic” form. \mathbf{E} is the electric field, \mathbf{D} is the electric displacement field, \mathbf{B} is the magnetic flux density, \mathbf{H} is the magnetic field intensity, ρ is the free charge density, and \mathbf{j} is the free current density. Replacing \mathbf{B} and \mathbf{D} in equations (3) and (4), respectively, and assuming no charge and current densities, the relationships are now:

$$\nabla \times \mathbf{E} = -\mu_0 \mu_r \frac{\partial \mathbf{H}}{\partial t} \quad (5)$$

$$\nabla \times \mathbf{H} = \varepsilon_0 \varepsilon_r \frac{\partial \mathbf{E}}{\partial t} \quad (6)$$

where μ_0 is the permeability of free space, μ_r is the relative permeability, ε_0 is the permittivity of free space, and ε_r is the relative permittivity. Taking the curl of equation (5) and plugging in the curl of \mathbf{H} from equation (6) gives the wave equation:

$$\nabla \times (\nabla \times \mathbf{E}) = -\mu_0 \mu_r \varepsilon_0 \varepsilon_r \frac{\partial^2 \mathbf{E}}{\partial t^2} = \nabla^2 \mathbf{E} \quad (7)$$

with a form of:

$$\mathbf{E}(z, t) = E_0 e^{i(kz - \omega t)}, \quad k = \frac{2\pi}{\lambda} \quad (8)$$

where the wave is propagating in the z-direction, k is the wave vector, ω is the angular frequency, λ is the wavelength, and E_0 is the amplitude of the wave.

For bulk metals with free electrons, the oscillation of the electrons in response to an applied field can be modeled as a Lorentz dipole. The displacement in the x-direction of an electron oscillation from an x-polarized electromagnetic wave is calculated by:

$$m_0 \frac{d^2 x}{dt^2} + m_0 \gamma \frac{dx}{dt} = -e \mathbf{E}(z, t) \quad (9)$$

where m_0 is the electron mass and γ is the frictional damping. The solutions are of the form:

$$x = x_0 e^{-i\omega t} \quad (10)$$

and leads to displacement:

$$x = \frac{eE}{m_0(\omega^2 + i\gamma\omega)} \quad (11)$$

The total polarization, \mathbf{P} , of the electron cloud also depends on the number of electrons, N , as well as the charge of the electrons, e :

$$\mathbf{P} = -Nex \quad (12)$$

The polarization can then be related to the electric field and the electric displacement field by the following:

$$\mathbf{D} = \epsilon_r \epsilon_0 \mathbf{E} = \epsilon_0 \mathbf{E} + \mathbf{P} \quad (13)$$

where the permittivity is a function of frequency and can be separated into its real and imaginary components, ϵ_1 and ϵ_2 , respectively.

$$\epsilon(\omega) = \epsilon_0 \epsilon_r(\omega) = \epsilon_1(\omega) + i\epsilon_2(\omega) \quad (14)$$

Finally, combining equations (11), (12) and (13), an expression for the relative permittivity for metals is derived:

$$\epsilon_r(\omega) = 1 - \frac{Ne^2}{\epsilon_0 m_0} \frac{1}{(\omega^2 + i\gamma\omega)} = 1 - \frac{\omega_p^2}{\omega^2} ; \quad \omega_p = \left(\frac{Ne^2}{\epsilon_0 m_0} \right)^{1/2} \quad (15)$$

where ω_p is the plasma frequency. For frequencies near the visible regime, the damping $\gamma \approx 0$.² Since $\mu_r = 1$ at optical frequencies, the index of refraction, n , is simply:

$$n = \sqrt{\epsilon_r \mu_r} = \sqrt{\epsilon_r} \quad (16)$$

This means that for frequencies below the plasma frequency, n is imaginary and any incident light is reflected. When the frequency is above the plasmon frequency, n is real and incident light passes through the metal.³

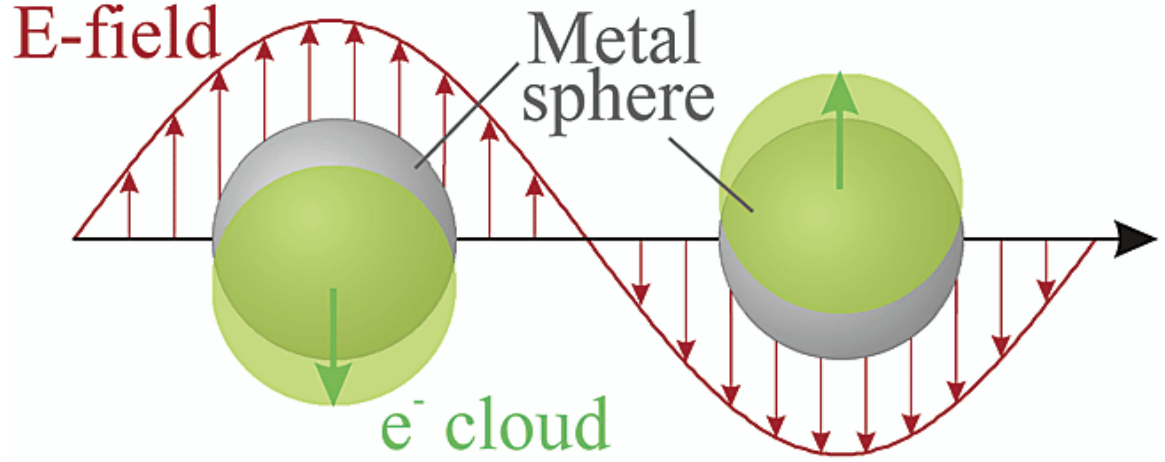


Figure 1.1 Schematic of the displacement of the free electron cloud in a metal nanosphere relative to the ion core. Reproduced from Ref.⁴

For metal nanoparticles, an incident electromagnetic (EM) field can cause coherent oscillations of the plasma of conduction electrons. These oscillations cause displacements of the electron cloud with respect to the nuclei of the metal nanoparticle, creating a dipole with a Coulombic restoring force. **Figure 1.1** shows a schematic of the displaced electron cloud for a plasmon oscillation. Using the quasistatic approximation, which assumes that the size of the particle is much smaller than the wavelength of the EM wave, the external electric field can be taken as a constant, and, therefore, the dipole approximation is valid.⁵ For a sphere of radius ‘ a ’, the dipole moment is related to the incident electric field by the polarizability, α :

$$\alpha = g_d a^3 \quad (17)$$

$$g_d = \frac{\varepsilon_m - \varepsilon_d}{\varepsilon_m + 2\varepsilon_d} \quad (18)$$

where ε_m is the permittivity of the metal and ε_d is the permittivity of the surrounding medium. The resulting extinction and scattering efficiencies are given as:

$$Q_{ext} = 4\hat{x}Im(g_d) \quad (19)$$

$$Q_{sca} = \frac{8}{3}\hat{x}^4|g_d|^2 \quad (20)$$

where,

$$\hat{x} = \frac{2\pi\sqrt{\varepsilon_d}}{\lambda} \quad (21)$$

There exists a resonance at the pole of equations (18)-(20) when:

$$Re[\varepsilon_m(\omega)] = -2\varepsilon_d \quad (22)$$

known as the Fröhlich condition.⁶ This resonance is known as the localized surface plasmon resonance, or LSPR, causing enhanced extinction around the resonance wavelength and electric field amplification within the near-field of the particle.

In order to explore the effects of particle size on the resonance, one must consider the modified long wavelength approximation.⁵ For particles large enough to fall outside of the quasistatic regime, one must consider the radiative correction field, \mathbf{E}_{rad} , where:

$$\mathbf{P} = \alpha[\mathbf{E} + \mathbf{E}_{rad}] \quad (23)$$

$$\mathbf{E}_{rad} = \frac{2}{3}ik^3\mathbf{P} + \frac{k^2}{a}\mathbf{P} \quad (24)$$

The radiative correction field is composed of two terms. The first term in equation (24) is from radiative damping caused by spontaneous radiation by the dipole. The second term is from depolarization; as the size of the metal nanoparticle is large enough that the electric field can no longer be considered constant. These effects influence the polarizability by a factor, F :

$$F = \left(1 - \frac{2}{3}ik^3\alpha - \frac{k^2}{a}\alpha\right)^{-1} \quad (25)$$

$$\mathbf{P} = \alpha F \mathbf{E} \quad (26)$$

$$\alpha F = \alpha_{size} = \frac{\alpha^3(\epsilon_i - \epsilon_0)}{3\epsilon_0 + (\epsilon_i - \epsilon_0)\left[1 - \frac{2}{3}(ka)^3i - (ka)^2\right]} \quad (27)$$

wherein the resonance condition is now a function of the particle size, but reduces to the Fröhlich condition for small values of ka .

In addition to the effects of particle size, the effect of geometry, composition and dielectric environment on the optical properties of the particles have also been experimentally determined by the works of Van Duyne *et al.*⁷⁻¹² Although these works addressed nanoparticle arrays, they did not address the coupling between the individual nanoparticles in the array. There are two main effects of inter-particle coupling on the optical properties of nanoparticle arrays: resonance energy or wavelength and bandwidth (FWHM). A semi-analytical model showed that the retarded dipole sum of all the nanoparticle interactions contains both real and imaginary portions. The dipole sum, S , is:

$$S = \sum_{dipole} e^{ikr} \left[\frac{(1-ikr)(3\cos^2\theta-1)}{r^3} + \frac{k^2\sin^2\theta}{r} \right] \quad (28)$$

where, r is the distance between two dipoles and θ is the angle between dipoles. The real portion determines the resonance wavelength of the nanoparticle arrays, and the imaginary portion gives rise to the bandwidth.¹³ The bandwidth or damping rate, Γ , is related to the plasmon dephasing time, often denoted as T_2 , by the relationship¹⁴:

$$\Gamma = \frac{2\hbar}{T_2} \quad (29)$$

where \hbar is the reduced Plank or Dirac constant. This is related to the plasmon decay time or plasmon lifetime, τ_{pl} by the simple relation:

$$T_2 = 2\tau_{pl} \quad (30)$$

Both the time domain dephasing time and the frequency domain bandwidth are manifestations of the plasmon damping. This damping is caused by two effects: radiative decay of the plasmons into photons and non-radiative absorption processes.⁶ Thus, the slower the plasmon decay time, the smaller the bandwidth, and the better for plasmonics applications. Another phenomenon that occurs when observing the optical properties of nanoparticle arrays arises from periodicity of the array itself.^{15,16} For particle arrays, coherent scattering of the light that is propagated into the plane of the nanoparticles can exhibit multiple scattering by the periodic particles.¹⁷ These grating effects can modify the homogeneously-derived spectral bandwidth, Γ , making it no longer only a function of the dephasing time T_2 .¹⁸

For plasmonic applications, an abundance of free electrons is of high importance. This is essential in the electric polarization in response to an applied electromagnetic

field,¹⁹ as seen in equations (12) & (13), and is governed by the electrical permittivity, ε , given by equation (14). The real portion, ε_1 , is indicative of the strength of the polarization of a material, and the imaginary portion, ε_2 , gives the loss associated with the polarization. Additionally, the quality factor, Q , is a unitless quantity which is often defined as:

$$Q = \frac{\lambda_{res}}{\Gamma} \quad (31)$$

where λ_{res} is the resonance frequency, and Γ is the bandwidth of the resonance. For a localized surface plasmon resonance, the quality factor represents a ratio of the enhanced local electric field to the total incident field. This quantity depends highly on the shape of the nanoparticle and is given by:²⁰

$$Q_{LSPR,Sphere}(\omega) = \frac{-\varepsilon_1(\omega)}{\varepsilon_2(\omega)} \quad (32)$$

$$Q_{LSPR,Oblate\ Sphereoid}(\omega) = \frac{\varepsilon_1(\omega)^2}{\varepsilon_2(\omega)} \quad (33)$$

where the higher aspect ratio particle can potentially yield higher quality factors because of the “lightning rod effect” and is more highly dependent on the value of the real component of the permittivity.¹⁹ Thus, for plasmonic applications, a suitable material needs to have a negative ε_1 by the Fröhlich condition in equation (22), but also small ε_2 to minimize losses as seen in equations (32) & (33). Metals are often the material of choice for plasmonic applications because of their abundance of free electrons and large negative real permittivity in the visible and telecommunication wavelength regimes. This

can be seen in **Figure 1.2**, for a variety of metals used in plasmonic applications in the visible and near-IR regimes.

All of these metals have very large negative real permittivities and various values for the imaginary permittivity across the visible and near-IR spectrum. We can see that for the visible regime, silver has very low loss, leading to superior plasmonic properties. Aluminum is ideal for plasmonics in the UV regime, but has large losses in the visible. Gold and copper, have relatively high losses at round 500 and 600 nm, respectively, from losses attributed to interband transitions. These losses occur when electrons jump to higher, unoccupied energy levels through photon absorption. Despite these losses and relative inferiority to silver, gold is most often used in plasmonic applications as the active material. This is because optical performance and lower material cost are traded for chemical stability

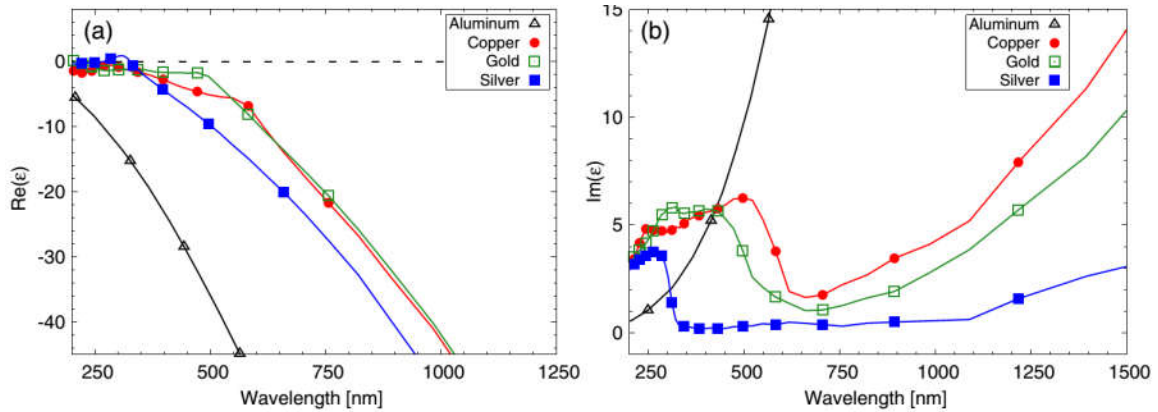


Figure 1.2 (a) Real, denoted ϵ_1 , and (b) imaginary permittivity, denoted ϵ_2 , for Al, Cu, Au and Ag. Reproduced from Ref. ²¹

Since LSPRs rely upon the interface between the metal and dielectric, the quality of the metal surface is of great importance. Silver tarnishes and forms Ag_2S on the surface from sulfur-containing gasses in air. Copper reacts with oxygen and forms a non-passivating oxide on the surface. Aluminum forms a thin layer of oxide almost immediately upon exposure to air, but can be thin and self-limiting. These dielectric layers alter the plasmonic properties of the metallic nanoparticles through increased surface roughness and scattering as well as increasing the losses seen by the nanoparticles. Gold is the only plasmonic material that is free of these issues in the long term.

1.3 Graphene

Graphene is the ubiquitous single layer of carbon atoms with sub-nanometer thickness. It had been theorized and concluded that graphene was not thermodynamically stable as a monolayer.^{22,23} The prevailing theory was that the thermal fluctuations of a 2-dimensional (2D) material would be on the order of the interatomic spacing of the graphene structure itself. Combined with the experimental evidence showing decreasing melting temperatures of thin films approaching the atomic limit, this gave rise to the belief that a flat graphene sheet would lead to lower energy configurations of curved carbon materials.²⁴ The only existence of 2D materials could form from epitaxial growth on an existing substrate with matched lattices.²⁵

History, has proven otherwise in terms of the possibility of these 2D materials, more specifically graphene. The first experimental realization came in 2004 by Novoselov and Geim.²⁶ Using highly-crystalline graphite and “mechanically exfoliation”

using adhesive tape, they were able to prove the existence of graphene by repeatedly cleaving bulk crystals in half normal to the weakly bonded c-axis. The resulting monolayer sheet has a hexagonal, honeycomb-like structure with each carbon having 120° sp^2 hybridized bonds to three other carbon atoms. **Figure 1.3** shows the structure of graphene and the basis it serves for forming other dimensional structures, such as buckyballs, carbon nanotubes, and back to graphite. Graphene also has delocalized π -bonds in the c-axis, which gives rise to interesting thermal, mechanical and electrical properties.

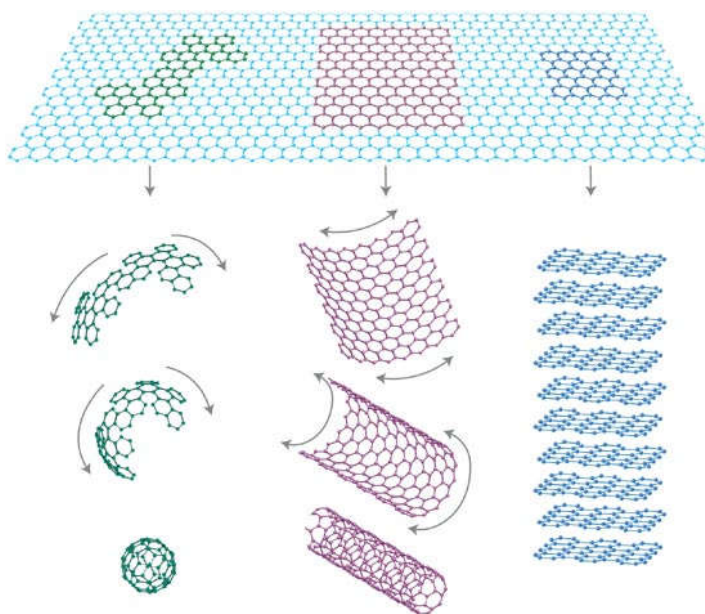


Figure 1.3 A graphene sheet with 2D honeycomb-like lattice can serve as the basis for wrapping into (0D) buckyballs, rolled into (1D) nanotubes, and stacked back into (3D) graphite. Reproduced from: ²⁷

Identification and verification of the monolayer nature of graphene is of utmost importance given the layer-dependent properties as well as the aforementioned theories

against its existence. One of the first methods of identification was to use atomic force microscopy (AFM) to look at the step height between the substrate and the graphene thickness. It was relatively well known that the step height between graphite layers was 0.35 nm, but resolution of the monolayer on substrate was more difficult to achieve because of the differences in the AFM tip interactions between insulating substrates and conductive graphene.²⁸ Because of this, reported values for the height of monolayer graphene sheets were on the order of 0.5 to 1 nm.²⁶ The first sub-0.5 nm measurement of the thickness of graphene came from monolayer flakes that had folded over upon itself during the mechanical exfoliation process. These led to AFM measurements of ~0.4 nm because of the consistent tip interactions.²⁹

Optical methods of the identification for graphene proved to be the most used and reliable tools for quickly determining whether a flake is monolayer or not. Optical transmission measurements have shown that each monolayer of graphene absorbs about 2.3% of the incident light, leading to an equal decrease in the transmission.³⁰ This has also been shown to scale linearly with an increasing number of graphene layers and can be seen in **Figure 1.4a**.³¹

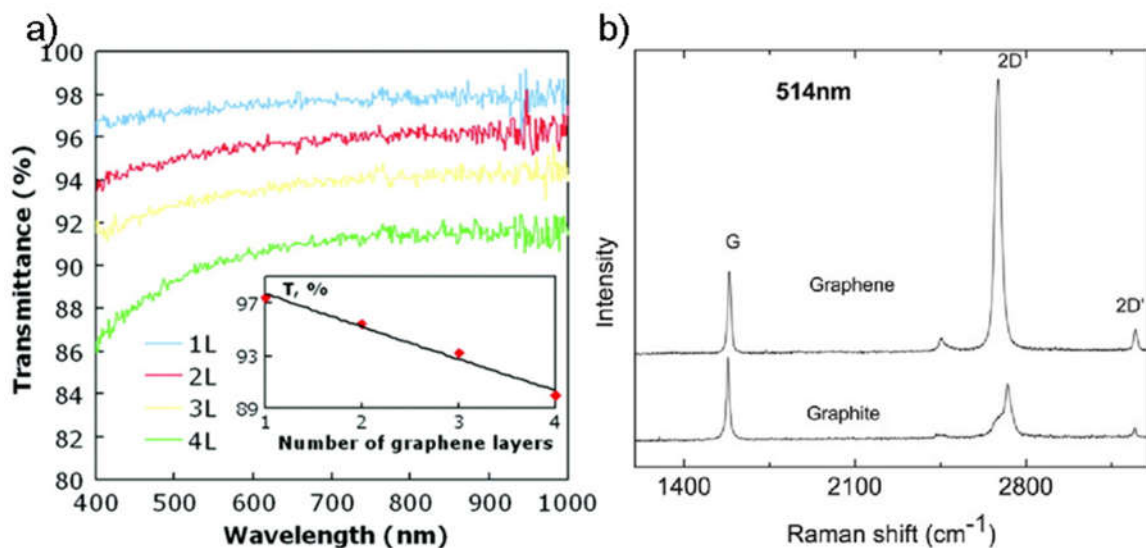


Figure 1.4 (a) Transmission spectra for 1 to 4 layers of graphene with the inset showing the transmission at $\lambda=550$ nm. Reproduced from Ref.³¹ (b) Raman spectrum for both graphite and graphene samples with an excitation wavelength of $\lambda=514$ nm. Reproduced from Ref.³²

The most commonly used method for identification of graphene monolayers is Raman spectroscopy. The number of stacked layers is reflected in transitions in the characteristics in the Raman signatures differentiating between graphite and graphene. The two most prominent vibrational modes occur around 1580 cm^{-1} and 2700 cm^{-1} ; these are referred to as the G and 2D peaks. For an excitation wavelength of 514 nm, representative Raman spectra for both graphene and graphite can be seen in **Figure 1.4b**. The G peak is present in all poly-aromatic hydrocarbons and is the result of bond stretching E_{2g} mode of sp^2 hybridized atoms in both ring and chain conformations.³² The 2D peak is the second order D peak, which is characteristic of the A_{1g} breathing mode in the same sp^2 hybridized atoms. The D peak, which is not Raman active in perfect crystalline samples, can be seen at edges, defects, and other symmetry breaking points

and is located around 1350 cm^{-1} . The 2D has also been referred to as the G' peak as it was the next highest intensity peak in graphene samples and erroneously thought to be the second order G peak. A third feature located around 3250 cm^{-1} is the second order of the intra-valley D' peak and consequently referred to as the 2D' peak. While much more analysis can and has been done for these Raman modes,^{32,33} these characteristic modes are used in simple intensity ratio comparisons to identify graphene. For graphite, the 2D peak is 1/4 to 1/2 of the intensity of the G band. Graphene on the other hand, has a 2D peak intensity that is about 4 times greater than that of its G peak. Because of this relatively simple identification method, Raman spectroscopy has been the method of choice for quick and accurate graphene identification

One of the most interesting properties of graphene is its unique electronic structure. Intrinsic graphene is a zero-gap semiconductor; its conduction and valence bands meet at what are known as Dirac points.³⁴ This occurs at six different points along the momentum space, where the Fermi level $E_F = 0$. Its linear energy dispersion is given by:

$$E = \hbar\gamma k \quad (34)$$

where k is the 2D carrier wave vector and γ is the Fermi velocity. In the intrinsic case, graphene has no free carriers. Under external gating voltage, the ambipolar nature of graphene's linear electronic structure leads to free carriers depending on the polarity of the gate voltage. The carrier density, n , from an external gate voltage is given by:

$$n = \frac{\kappa_s V_g}{4\pi t} \quad (35)$$

where V_g is the gate voltage, κ_s is the dielectric constant of the substrate, and t is the thickness of the substrate between the graphene and the external gate electrode. This gating process and introduction of free carriers ultimately changes the Fermi level of the graphene, changing what used to be a zero-bandgap material to one with a finite band gap. **Figure 1.5** shows that increase in external gate voltage leads to decreased resistivity and changing of the Fermi level. A similar effect of bandgap engineering can be achieved using chemical doping to introduce impurity centers.³⁵ This changes the intrinsic condition of the graphene and leads to higher conductivities and larger bandgaps at zero gate voltage.

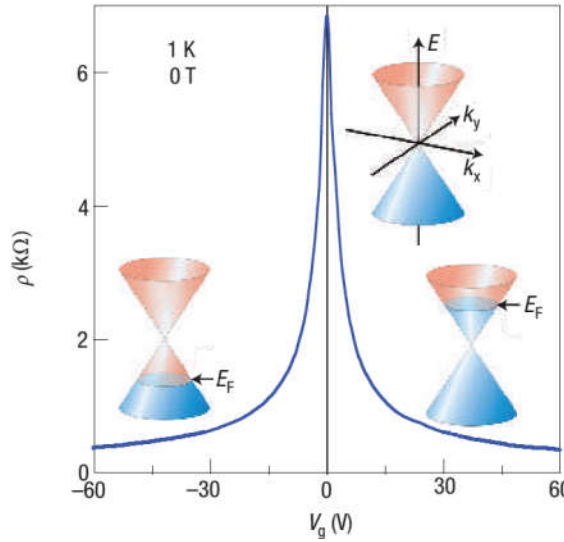


Figure 1.5 Ambipolar field effect of graphene, showing decreasing resistivity, ρ , with increasing magnitude of the gate voltage, V_g . The inset shows graphical representations of the Dirac cones and Fermi energy position as a function of positive and negative gate biases as well as the intrinsic case. Reproduced from Ref. ³⁶

Mobility of the free carriers in graphene can be simply calculated by:

$$\mu = \frac{1}{ne\rho} \quad (36)$$

where n is the carrier density, e the elementary charge, and ρ the sheet resistance of the graphene film. The highest reported mobility for graphene was reported by Bolotin *et al.* in 2008 at 200,000 cm²/Vs at an electron density of $\sim 2 \times 10^{11}$ cm⁻².³⁷ Such high mobilities were only able to be achieved by undercutting the underlying substrate to create a fully suspended graphene flake. Since mobility is limited by carrier scattering, eliminating the substrate also eliminates any substrate-related scattering phenomena. Thus, for suspended graphene, the intrinsic limit to mobility arises from electron-acoustic phonon scattering.³⁸ When confined to a substrate, namely SiO₂, this mobility limit decreases to 40,000 cm²/Vs from the interaction with the acoustic photons from the SiO₂ layer. These large mobilities in graphene are a direct result of the very low defect densities in graphene exfoliated from high quality Kish graphite.^{39,40}

This high quality “honeycomb” carbon sheet lends itself to other important attributes as well. One of these attributes is the inability of most gas molecules to diffuse through or penetrate the graphene lattice. This was first observed in the work by Bunch *et al.*⁴¹ when creating suspended graphene membranes on top of an enclosed SiO₂ cavity. They observed that when the graphene membranes were placed into an environment where there existed a pressure difference between the cavity and the environment, the membrane would bow outward or inward depending on the pressure differential. Simulations using density functional theory (DFT) have studied this effect and showed that because of the low defect density in graphene sheets, only hydrogen atoms can penetrate a pristine graphene sheet.⁴² DFT simulations showed that He atoms with kinetic energy of up to 18.6 eV are reflected by the graphene (**Figure 1.6a-c**). Similarly, this

phenomenon has been experimentally observed; bulk graphite and monolayer graphene sheets have the same permeability toward gaseous species and can be seen in **Figure 1.6d**. However, although hypothesized that only pristine, defect-free graphene, the aforementioned DFT calculations showed that defects do not automatically allow diffusion through the graphene structure. With increasing defect size, the energy barrier for penetration through the graphene decreases exponentially. This means that although pristine graphene is ideal for applications in which gas permeation should be limited; graphene with non-zero concentrations of defect densities can also be applicable.

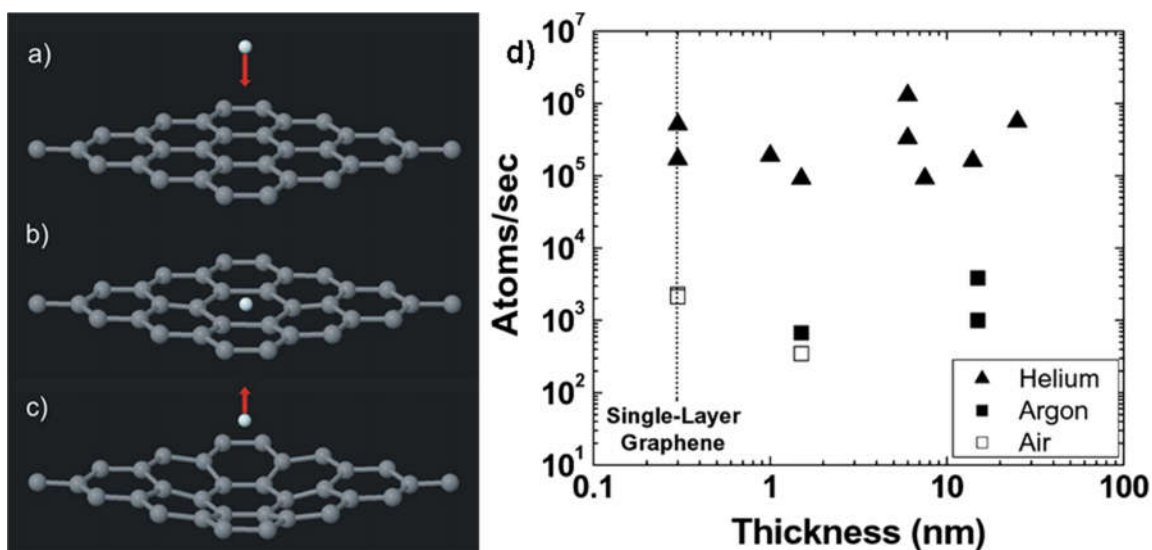


Figure 1.6 (a-c) A simulation using density functional theory (DFT) to show the reflection of a He atom with 18.6 eV of kinetic energy. Reproduced from Ref. ⁴² (d) Graph showing the permeability of different gas species through different thickness layers of graphite down to monolayer graphene. Reproduced from Ref. ⁴¹

Because of the myriad of interesting properties of monolayer graphene, there has been considerable interest in scalability. Thus, larger quantities of material needed to be

produced as an alternative to the traditional mechanical exfoliation techniques that low-yield, small-area monolayers. The most promising large area synthesis method is chemical vapor deposition (CVD). CVD methods rely upon deposition of carbon-based materials onto metal layers from a hydrocarbon source. This process has been well studied for reactive nickel surfaces but has traditionally yielded bulk graphite crystals. By reducing the thickness of the nickel film to the 100s of nm scale and carefully tuning the growth parameters, continuous sheets of few-layer graphene were able to be grown.^{43,44} By changing the growth substrate from Ni to Cu, CVD growth of graphene has been able to produce consistent monolayers of material. **Figure 1.7a-b** show SEM images of graphene growth on the surface of copper foils with its poly-crystalline nature. The switch to a copper growth substrate changes the growth mechanic from precipitation of the carbon onto the nickel surface to surface-catalyzed segregation of the carbon on the copper surface.⁴⁵ This not only allows for the facile growth of monolayers, but copper foils can be used to grow the monolayers without the need of a backing SiO₂/Si wafer. Since the graphene films are transferred by etching away the underlying metal film, the absence of the backing wafer facilitates the transfer process. The transferred graphene films can be seen in **Figure 1.7c-d**.

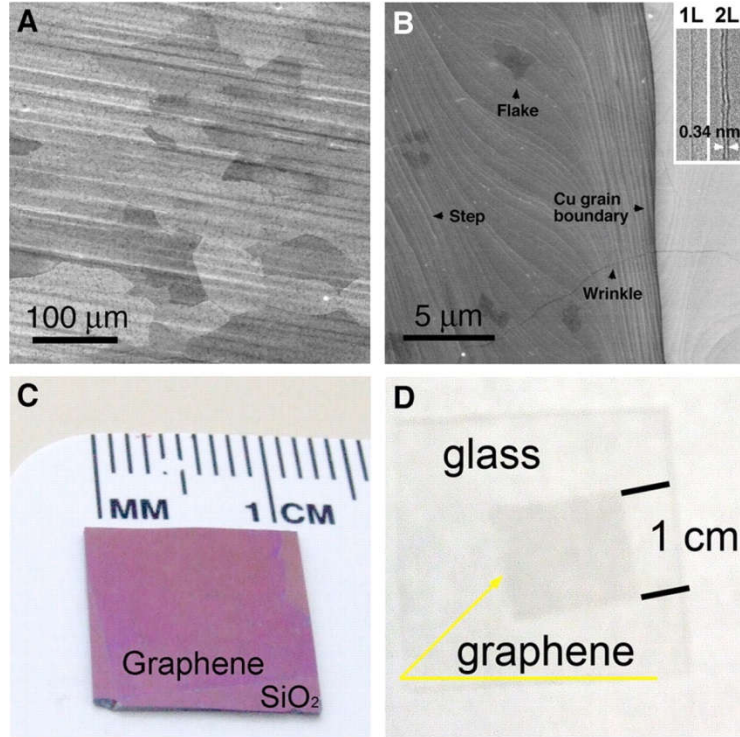


Figure 1.7 (a) SEM and (b) high-resolution SEM images of graphene grown on Cu foils with (inset) TEM images of folded monolayer and bilayer graphene edges. (c-d) Images of transferred graphene films onto SiO_2/Si and glass substrates. Reproduced from Ref.⁴⁵

1.4 Whispering Gallery Mode Optical Microcavities

Optical microcavities are structures analogous to acoustic resonators such tuning forks. In the case of the tuning forks, the shape of the fork determines the resonant acoustic mode. Similarly, in an optical microcavity, optical modes can be resonant depending on the how the cavity is engineered. The simplest cavity design is the Fabry-Pérot cavity which consists of two parallel reflectors separated by a specified distance. The light is confined inside the cavity by the reflections of the mirrors. The resonance condition, where the light with the same phase returns to its starting point, is determined by the cavity

geometry and dimensions. For non-parallel cavities, this reflection is satisfied through total internal reflection through the surfaces of the cavity and the outside medium.

The free spectral range (FSR) is the frequency step between adjacent modes in the optical cavity. The FSR is the reciprocal to the length of time it takes to make one “round trip” through the cavity, t_r . It is given by the equation:

$$FSR = \frac{c}{2n_r L_c} = \frac{1}{t_r} \quad (36)$$

where n_r is the cavity mode index, L_c is the round-trip length of the cavity, and c is the speed of light.⁴⁶ There are two ways to quantify the “quality” or efficiency of an optical cavity: finesse, \mathcal{F} , and quality factor, Q . These quantities are measured with respect to the bandwidth or FWHM, Γ and related through the equations:

$$\mathcal{F} = \frac{FSR}{\Gamma} \quad (37)$$

$$Q = \frac{\nu}{FSR} \mathcal{F} = \frac{\nu}{\Gamma} \quad (38)$$

where ν is the resonant frequency. These values quantify the deviation from ideality as a perfect cavity would have discrete resonant frequencies with zero bandwidth. The finesse is a measure of how many FWHM bandwidths can fit between adjacent resonant modes.⁴⁷ The quality factor is a measure of how much energy is stored within the cavity, or, conversely, the rate at which light energy leaks from the cavity.⁴⁸

An optical cavity can also enhance the emission rate of a two-state system by manipulation of the available density of states. When the two-state system is coupled to a

cavity, transitions that fall within the resonant frequencies of the optical cavity experience a higher density of states. The rate of transition is proportional to the density of states as stated by Fermi's golden rule. Additionally, off-resonant frequencies of the cavity-coupled system can experience a density of states lower than that of the free-space case. Because of this, spontaneous emission at unwanted, non-resonant frequencies can be suppressed.⁴⁹ The spontaneous emission enhancement factor, or Purcell factor, P , is given by:

$$P = \frac{3}{4\pi^2} \left(\frac{\lambda}{n} \right)^3 \frac{Q}{V} \quad (39)$$

where, λ is the resonant wavelength, n is the mode index, Q is the quality factor of the resonant mode, and V is the mode volume. To this end, a great deal of effort in engineering cavities with high quality factors and low mode volumes has been undertaken.

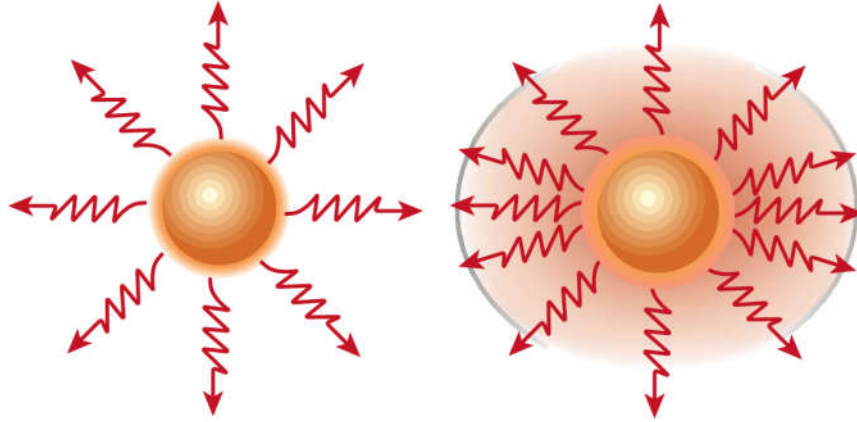


Figure 1.8 Schematic of the spontaneous emission of a two-state system in (left) free space and (right) in a coupled cavity showing enhanced spontaneous emission rate. Reproduced from Ref.⁵⁰

For cavities with axial symmetry, the modes that form are known as whispering gallery modes (WGMs). These are named after the famous acoustic modes that travel around a “whispering gallery” type manner along the circumference of the dome-shaped cathedral hall in St. Paul’s Cathedral. These WGMs are cylindrical in nature and are optically circulated along the circumference of the cavity by total internal reflection. Following the formalism of Gomilšek,⁵¹ we can solve for the eigenmodes and eigenfrequencies for these WGMs in a cylindrical cavity. First, however, we must start with the wave equation for a scalar or electromagnetic longitudinal wave. For a wave with field amplitude of $u(\vec{r}, t)$,

$$\nabla^2 u - \frac{1}{c^2(\vec{r})} \frac{\partial^2 u}{\partial t^2} = f(\vec{r}, t) \quad (40)$$

where $f(\vec{r}, t)$ is the complex wave field source, and $c^2(\vec{r})$ is phase velocity profile. Separating variables, we get,

$$u(\vec{r}, t) = \psi_\zeta(\vec{r}) e^{-i\omega_\zeta t}, \text{Re}(\omega_\zeta) \geq 0 \quad (41)$$

where ζ represents the indices of the mode numbers (N, m) . We can disregard the imaginary portion of the frequency, ω_ζ , as solutions with imaginary frequency decay exponentially. Combining equations (40) and (41) as well as identity $f(\vec{r}, t) \equiv 0$, results in the Helmholtz equation:

$$\nabla^2 \psi_\zeta + \frac{\omega^2}{c^2(\vec{r})} \psi_\zeta = 0 \quad (42)$$

In this equation, ω_ζ^2 represents the eigenmodes, and $\psi_\zeta(\vec{r})$ the eigenfunctions. In the case of a cylindrical cavity of radius a , a consequence of total internal reflection in a medium leads to $n = c_0/c_1$, where c_0 represents the speed of the wave outside the cavity, and c_1 the wave speed inside the cavity. This condition leads to two sets of the Helmholtz equation in equation (42):

$$\nabla^2 \psi_\zeta + k_{1,\zeta}^2 \psi_\zeta = 0 \quad , \quad r < a \quad (43)$$

$$\nabla^2 \psi_\zeta + k_{0,\zeta}^2 \psi_\zeta = 0 \quad , \quad r > a \quad (44)$$

to account for the two different wave speeds inside and outside the cavity. Here, the wavenumber, $k_{0,1,\zeta} = \omega_\zeta/c_{0,1}$. Next, we impose four boundary conditions:

- 1) ψ_ζ is finite everywhere.
- 2) No waves traveling from $r \rightarrow \infty$ to origin $r \rightarrow 0$.
- 3) $\psi_\zeta(\vec{r})$ is continuous at the cavity edge, $r = a$.
- 4) $\nabla \psi_\zeta(\vec{r})$ is continuous at the cavity edge, $r = a$.

From boundary conditions 1) and 2), as well as converting the wavefunctions into a cylindrical basis, the solutions come in the form of Bessel, J_m , and Hankel functions of the first kind, $H_m^{(1)}$:

$$\psi_\zeta(\vec{r}) = e^{im\varphi} A_\zeta J_{|m|}(nk_{0,\zeta}r) \quad , \quad r < a \quad (45)$$

$$\psi_\zeta(\vec{r}) = e^{im\varphi} B_\zeta H_{|m|}^{(1)}(k_{0,\zeta}r) \quad , \quad r > a \quad (46)$$

where m is an integer. Boundary condition 3) then leads to:

$$\frac{B_\zeta}{A_\zeta} = \frac{J_{|m|}(nk_{0,\zeta}a)}{H_{|m|}^{(1)}(k_{0,\zeta}a)} \quad (47)$$

Then applying boundary condition 4) gives the characteristic equation:

$$\frac{J'_{|m|}(nk_{0,\zeta}a)}{J_{|m|}(nk_{0,\zeta}a)} = \frac{1}{n} \frac{H_{|m|}^{(1)'}(k_{0,\zeta}a)}{H_{|m|}^{(1)}(k_{0,\zeta}a)} \quad (48)$$

with the prime signifying ordinary differentiation. This characteristic equation can only be solved numerically with ω_ζ representing the eigenfrequency. **Figure 1.9** shows the solutions to the characteristic equation for $m = 1$ and $m = 15$ and for $N = 1-4$. We can clearly see that increased azimuthal mode number m leads to greater mode localization toward the radius of the cylinder as well as less leaking outside the cavity. The opposite is true with increasing radial mode number, N . Generally, only $N = 1$ mode solutions are referred to as WGMs.

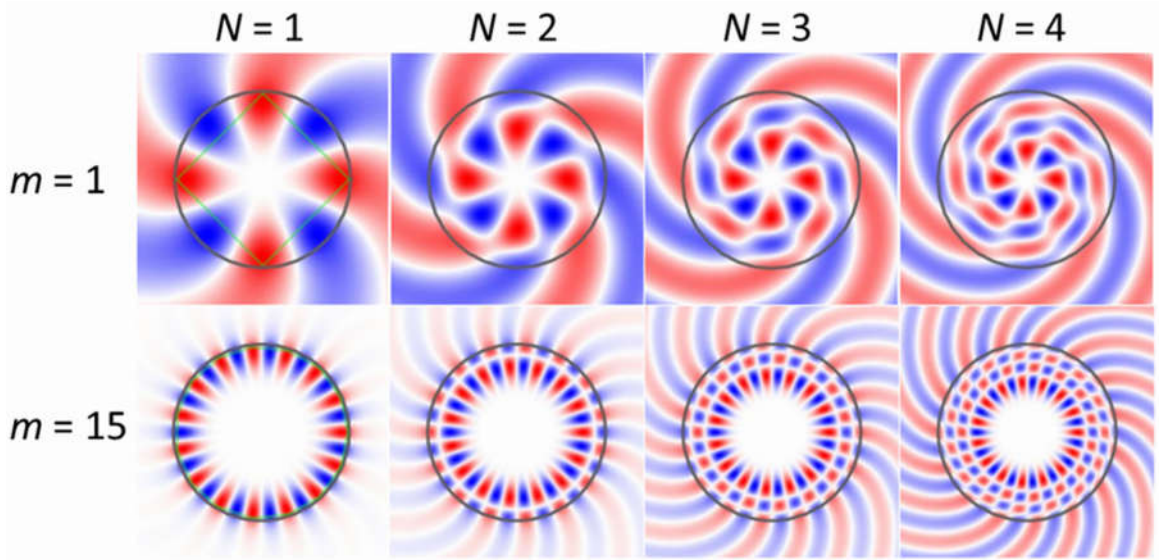


Figure 1.9 Eigenmode profiles for a cylindrical cavity for different mode numbers. Azimuthal mode number $m = 1$ for the top row and $m = 15$ for the bottom row. Radial mode increases from $N = 1$ in the leftmost column to $N = 4$ for the rightmost column. Reproduced from Ref.⁵¹

The quality factor of the resonance in a WGM resonator consists of three different mechanisms: material absorption, surface scattering, and bending losses. The higher the magnitude of these losses, the smaller the resulting quality factor. This leads to a larger contribution to the limiting factor of the overall cavity quality. These components can contribute to the quality factor as follows.⁵²

$$\frac{1}{Q} = \frac{1}{Q_{mat}} + \frac{1}{Q_{scatt}} + \frac{1}{Q_{bend}} \quad (49)$$

Q_{mat} refers to the absorption of the circulating energy by the cavity material itself. For visible frequencies, many of the dielectric materials used in microcavity fabrication are extremely low loss, leading to very high material-based quality factors, and conversely, contributes very little to the limiting factor determining the overall quality of the cavity.⁵³ Similarly, losses from bending, Q_{bend} , also do not contribute very much to the overall Q . WGM cavities in the visible and near-IR frequencies tend to be on the order of several to hundreds of microns.^{49,54,55} Typically, bending losses do not become appreciable until cavities become sub-micron in radius.⁵⁶ Thus, by far, the limiting factor for high-quality WGM cavities is the contribution from scattering and surface absorption. To this end, smooth cavity edges free of impurities are highly desired and have been achieved using various methods including fused silica microspheres,⁵⁷⁻⁶¹ laser reflow micro-toroid cavities (**Figure 1.10**),^{49,52,54,62} and thermally annealed polymeric microdisk cavities.⁶³⁻⁶⁵

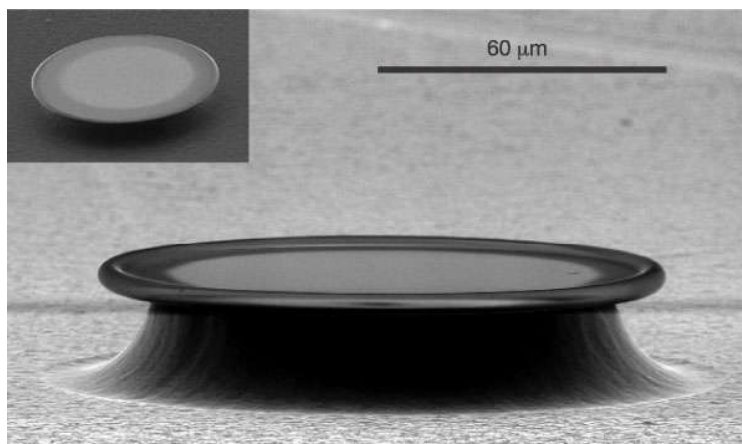


Figure 1.10 SEM image of a micro-toroid optical cavity with Q of 1.00×10^8 . The inset shows the microdisk cavity before CO_2 laser reflow. Reproduced from Ref.⁶⁶

1.5 2D Transition Metal Dichalcogenides

Transition metal dichalcogenides (TMDCs) are compounds that form with the chalcogen group of elements. The chalcogens are group VI elements with S, Se, and Te as the main constituent elements for forming the TMDCs. The chemical formula revolves around the template: MX_2 , with X being the chalcogen and M being the transition metal. **Figure 1.11** shows the list of transition metal elements that form layered chalcogenide compounds. Elements highlighted in groups 4-7 and 10 form the layered compounds, while group 9 as well as Ni only form some layered chalcogenides. The metals exist in their +4 oxidation state with the chalcogen in the complementary -2 state. The metal atoms form covalent bonds sandwiched between the chalcogen atoms to form the layered structure with relatively weak van der Waals bonds in-between layers. In total, there are around 40 candidate materials that fit this formula. The electronic characteristics of these materials can vary but generally fall within being semimetallic and semiconducting with a few candidates being superconducting.⁵⁹

H	MX ₂ M = Transition metal X = Chalcogen																He
Li	Be											B	C	N	O	F	Ne
Na	Mg	3	4	5	6	7	8	9	10	11	12	Al	Si	P	S	Cl	Ar
K	Ca	Sc	Ti	V	Cr	Mn	Fe	Co	Ni	Cu	Zn	Ga	Ge	As	Se	Br	Kr
Rb	Sr	Y	Zr	Nb	Mo	Tc	Ru	Rh	Pd	Ag	Cd	In	Sn	Sb	Te	I	Xe
Cs	Ba	La-Lu	Hf	Ta	W	Re	Os	Ir	Pt	Au	Hg	Tl	Pb	Bi	Po	At	Rn
Fr	Ra	Ac-Lr	Rf	Db	Sg	Bh	Hs	Mt	Ds	Rg	Cn	Uut	Fl	Uup	Lv	Uus	Uuo

Figure 1.11 Periodic table showing the different elemental components that for MX_2 TMDCs. The chalcogenides (S, Se, and Te) The solidly colored elements form layered compounds with all of the chalcogenides, while the half colored elements only form layered compounds with one or two of the chalcogenides. About 40 layered TMDC materials exist in this form. Reproduced from Ref.⁵⁴

Very much analogous to graphene and graphite, these layered crystalline materials with weak interlayer bonds can also be reduced to its monolayer form through the use of mechanical exfoliation. Other methods of chemical intercalation have also been used to form suspended sheets of monolayer material in solution, which can be cast into films on a substrate.^{60,61} While chemical intercalation can produce more monolayer material, this method, along with mechanical exfoliation, deposits flakes randomly on the surface of the target substrate and with varying thicknesses. Wide adoption of this material has come, like with graphene, with the development of chemical vapor deposition of single crystalline flakes of material on a substrate. These methods generally involve having the two precursors, usually an oxide of the transition metal and a source of the chalcogenide, heated in a tube furnace with a carrier gas that deposits the material as it flows over the surface of the substrate at elevated temperatures.⁶⁷⁻⁷¹ Recently, it has

been shown that templating the surface of the target substrate with the transition metal precursor can direct growth of the TMDC flakes in specific areas and patterns. **Figure 1.12** shows the templated growth of MoS₂ flakes in the shape of letters. This can further facilitate large scale production and layer-on-layer fabrication of devices.⁶⁵

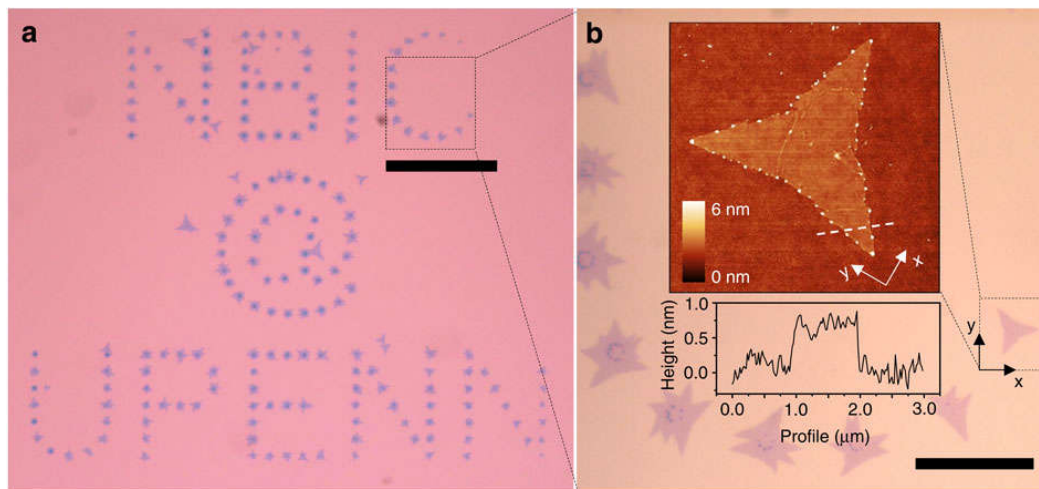


Figure 1.12 (a) Optical image of templated growth of MoS₂ flakes. The scale bar is 100 μm . (b) a higher magnification image of the MoS₂ flakes in panel (a) with an (inset) AFM scan of one of the flakes showing a sub-nm flake height. Scale bar is 20 μm . Reproduced from Ref.⁶⁵

Of these materials, MoS₂, MoSe₂, WS₂ and WSe₂ have stood out as more interesting materials because of their layer-dependent properties. In the bulk, these four materials are indirect bandgap semiconductors. **Figure 1.13** shows the band structure for MoS₂ and WS₂ for both the bulk and monolayer cases.⁵² The DFT calculations show the conduction band (in green) as well as the valence band (in blue) for these four cases. As the number of layers decreases, there is also a gradual shift from indirect to direct bandgap. Shifts in the energetic landscape allow for a larger but direct bandgap at the K point for both materials.

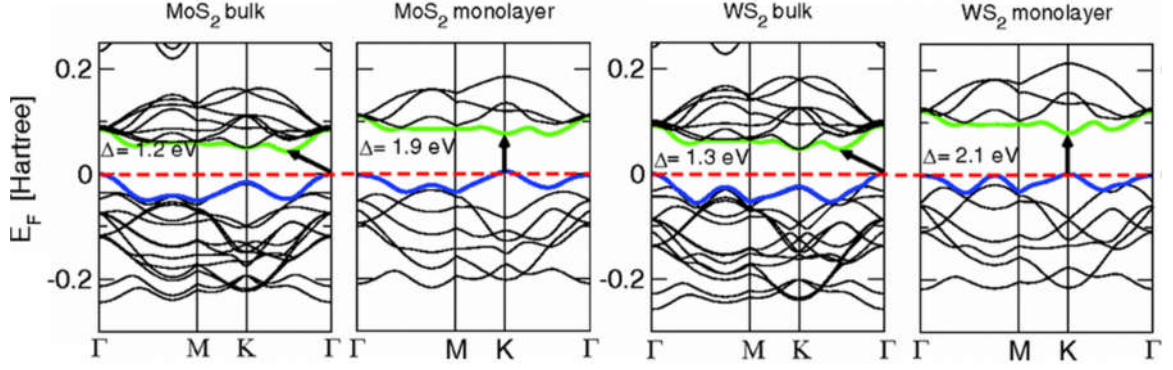


Figure 1.13 DFT calculations of the electronic band structure for sulfides of Mo and W both in the bulk and at the monolayer. Both bulk cases show a smaller, indirect bandgap, whereas the monolayer materials have a larger direct bandgap. Adapted from Ref.⁵²

In the case of MoS₂, the change in the band structure is attributed the hybridization of the electron orbitals as a result of quantum confinement.^{52,72,73} The confinement changes the way that the p_z orbitals in the S atoms as well as the d orbitals in the Mo atoms are hybridized. The antibonding p_z orbitals on the S atoms are greatly affected by the interlayer bonding. This causes a change in the conduction band near the Γ -point. On the other hand, the d orbitals of the central Mo atoms are not affected as much by the interlayer coupling as the orbitals are sandwiched between the S atoms. These orbitals contribute to the band structure near the K point and see a much smaller shift with regard to layer number.⁷² Quantum confinement as well as its effects on bonding orbitals explains similar effects on energetic transitions in MoSe₂, WS₂ and WSe₂.^{52,63,64}

In yet another analogy to graphene, identification of the monolayer nature of 2D TMDCs has also come to rely upon Raman spectroscopy and the related vibrational modes. **Figure 1.14a** shows the vibrational modes for MoS₂. Both the E_{2g}^1 and A_{1g}

modes produce discernable peaks in the Raman spectrum and can be seen for bulk all the way down the monolayer material in **Figure 1.14b**. The separation of these peaks changes with the layer thickness and is quantified in **Figure 1.14c**. For the case of MoS₂, these vibrational modes are heavily influenced by the number of layers and the number layers that exist in a sample flake of MoS₂ can be quantified by the separation of these two peaks.⁷⁴ Similar features in the Raman spectrum have been found in MoSe₂, WSe₂, and WS₂.⁷⁵⁻⁷⁸ Often, AFM measurements are also used to provide additional verification of the layer number characterization through optical means.

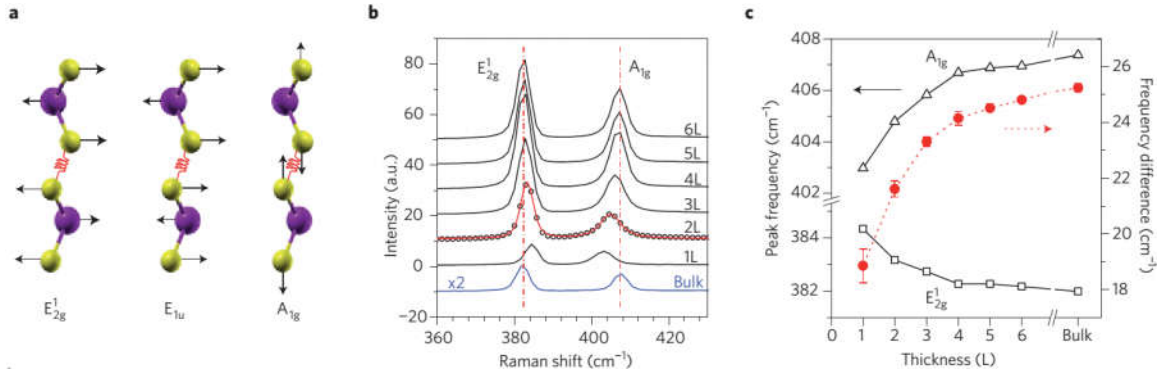


Figure 1.14 (a) Vibrational modes in MoS₂. (b) Raman spectroscopy of different layer thicknesses of MoS₂ showing the (c) separation of the E_{2g}^1 and A_{1g} modes as a function of layer thickness. Figure reproduced from Ref.⁵⁷; panel (a) reproduced from Ref.⁵⁸; panel (b-c) reproduced from Ref.⁷⁴

One of the most interesting aspects to the layer-dependent shift to direct bandgap in the Mo- and W-based TMDCs is the evolution of appreciable photoluminescence from the monolayer material. It was first discovered in MoS₂,^{72,73} and later in MoSe₂,⁷⁹ WSe₂, and WS₂.⁷⁷ **Figure 1.15a** shows the PL spectra for MoS₂ flakes produced through mechanical exfoliation, as well as the quantum yield (QY) for the photoluminescence process as a function of layer number. It is clear that as the layer number decreases to the

monolayer limit, the PL efficiency increases exponentially and appreciable light is emitted from monolayer MoS₂. Thus, it is clear that the transition from indirect bandgap to direct bandgap material has a large effect on the luminescence of the material. Quantum yield, however, is still relatively low, reaching 4×10^{-3} for the ideal, monolayer suspended case, and decreases drastically when in contact with the substrate.⁷³ WSe₂ and WS₂ have shown to have over an order of magnitude larger quantum yield over that of MoS₂, but yet still only reach 2×10^{-3} for the non-suspended, room-temperature case. WS₂ can reach a QY of $\sim 5 \times 10^{-3}$ when cooled to 10 K.⁸⁰

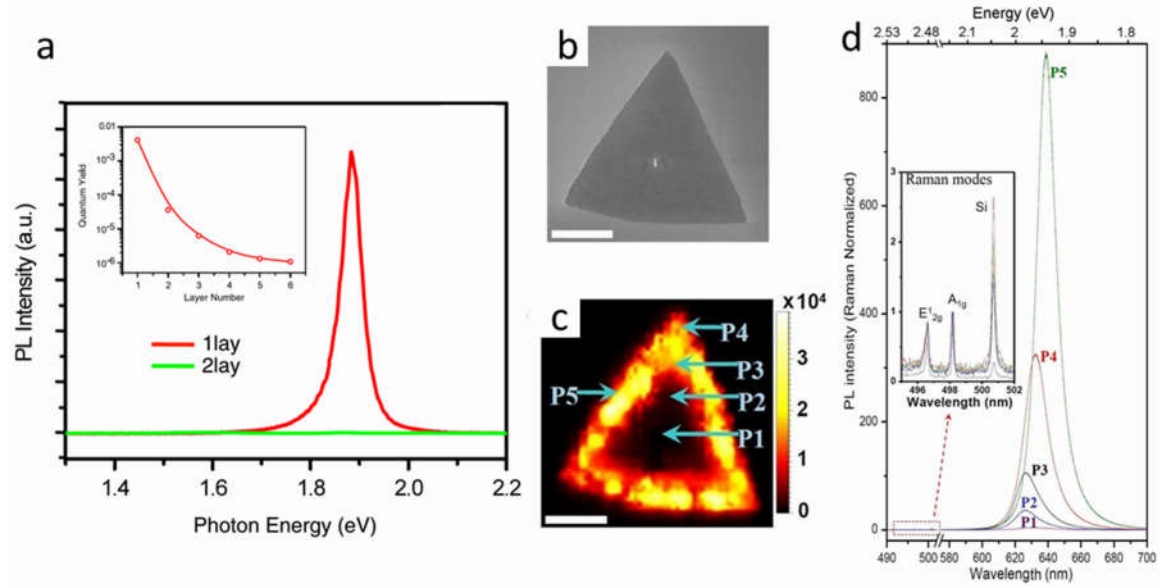


Figure 1.15 (a) Photoluminescence spectra for both monolayer and bilayer exfoliated MoS₂ flakes. The inset shows the quantum yield as a function of number of layers. (b) An SEM image of a WS₂ flake grown through CVD methods. (c) Map of the photoluminescence intensity for the flake in (b). (d) Photoluminescence spectra at different points of the WS₂ flake as denoted in (c). The inset shows the Raman spectra. Scale bar is 5 μ m. Adapted from Ref.⁷⁸ and Ref.⁷³

Figure 1.15b-d shows a CVD-grown WS₂ flake and the PL spectra at different locations at the flake. The entire flake, save for the centermost multilayer “seed”, is a monolayer crystal of WS₂. The spatially dependent PL intensity on what should be a uniform material suggests that the precise bonding structure or defect density will play a large role in the efficiency of the luminescence.^{78,81} Engineering efficient light production through either electromagnetic or chemical means of these 2D TMDC materials is key to not only increasing the quantum yield, but also their usefulness as a 2D source of light.⁸¹⁻

84

1.6 References

- 1 Fox, M. *Optical Properties of Solids*. Second edn, (Oxford University Press, 2010).
- 2 Hecht, E. *Optics*. Fourth edn, (Pearson, 2002).
- 3 Livingston, J. D. *Electronic Properties of Engineering Materials*. (John Wiley & Sons, 1999).
- 4 Kelly, K. L., Coronado, E., Zhao, L. L. & Schatz, G. C. "The Optical Properties of Metal Nanoparticles: The Influence of Size, Shape, and Dielectric Environment". *The Journal of Physical Chemistry B* **107**, 668 (2002).
- 5 Kelly, K. L., Coronado, E., Zhao, L. L. & Schatz, G. C. "The Optical Properties of Metal Nanoparticles: The Influence of Size, Shape, and Dielectric Environment". *The Journal of Physical Chemistry B* **107**, 668 (2003).
- 6 Maier, S. A. *Plasmonics: Fundamentals and Applications*. (Springer, 2007).
- 7 Hulsteen, J. C. & Van Duyne, R. P. "Nanosphere Lithography: A Materials General Fabrication Process for Periodic Particle Array Surfaces". *Journal of Vacuum Science & Technology A: Vacuum, Surfaces, and Films* **13**, 1553 (1995).
- 8 Jensen, T. R., Malinsky, M. D., Haynes, C. L. & Van Duyne, R. P. "Nanosphere Lithography: Tunable Localized Surface Plasmon Resonance Spectra of Silver Nanoparticles". *The Journal of Physical Chemistry B* **104**, 10549 (2000).
- 9 Jensen, T. R. *et al.* "Nanosphere Lithography: Effect of the External Dielectric Medium on the Surface Plasmon Resonance Spectrum of a Periodic Array of Silver Nanoparticles". *The Journal of Physical Chemistry B* **103**, 9846 (1999).
- 10 Hulsteen, J. C. *et al.* "Nanosphere Lithography: Size-Tunable Silver Nanoparticle and Surface Cluster Arrays". *The Journal of Physical Chemistry B* **103**, 3854 (1999).
- 11 Malinsky, M. D., Kelly, K. L., Schatz, G. C. & Van Duyne, R. P. "Nanosphere Lithography: Effect of Substrate on the Localized Surface Plasmon Resonance

- Spectrum of Silver Nanoparticles". *The Journal of Physical Chemistry B* **105**, 2343 (2001).
- 12 Haynes, C. L. & Van Duyne, R. P. "Nanosphere Lithography: A Versatile Nanofabrication Tool for Studies of Size-Dependent Nanoparticle Optics". *The Journal of Physical Chemistry B* **105**, 5599 (2001).
 - 13 Zhao, L. L., Kelly, K. L. & Schatz, G. C. "The Extinction Spectra of Silver Nanoparticle Arrays: Influence of Array Structure on Plasmon Resonance Wavelength and Width". *The Journal of Physical Chemistry B* **107**, 7343 (2003).
 - 14 Sönnichsen, C. *et al.* "Drastic Reduction of Plasmon Damping in Gold Nanorods". *Physical review letters* **88**, 077402 (2002).
 - 15 Lamprecht, B. *et al.* "Metal Nanoparticle Gratings: Influence of Dipolar Particle Interaction on the Plasmon Resonance". *Physical review letters* **84**, 4721 (2000).
 - 16 Felidj, N. *et al.* "Grating-Induced Plasmon Mode in Gold Nanoparticle Arrays". *The Journal of chemical physics* **123**, 221103 (2005).
 - 17 Auguie, B. & Barnes, W. L. "Collective Resonances in Gold Nanoparticle Arrays". *Physical review letters* **101**, 143902 (2008).
 - 18 Sönnichsen, C. *et al.* "Spectroscopy of Single Metallic Nanoparticles Using Total Internal Reflection Microscopy". *Applied Physics Letters* **77**, 2949 (2000).
 - 19 Maier, S. A. & Atwater, H. A. "Plasmonics: Localization and Guiding of Electromagnetic Energy in Metal/Dielectric Structures". *Journal of Applied Physics* **98**, 011101 (2005).
 - 20 West, P. R. *et al.* "Searching for Better Plasmonic Materials". *Laser & Photonics Reviews* **4**, 795 (2010).
 - 21 Lindquist, N. C., Nagpal, P., McPeak, K. M., Norris, D. J. & Oh, S.-H. "Engineering Metallic Nanostructures for Plasmonics and Nanophotonics". *Reports on Progress in Physics* **75**, 036501 (2012).
 - 22 Dresselhaus, M. S. & Dresselhaus, G. "Intercalation Compounds of Graphite". *Advances in Physics* **51**, 1 (2002).
 - 23 Shenderova, O. A., Zhirnov, V. V. & Brenner, D. W. "Carbon Nanostructures". *Critical Reviews in Solid State and Materials Sciences* **27**, 227 (2002).
 - 24 Venables, J. A., Spiller, G. D. T. & Hanbucken, M. "Nucleation and Growth of Thin Films". *Reports on Progress in Physics* **47**, 399 (1984).
 - 25 Evans, J. W., Thiel, P. A. & Bartelt, M. C. "Morphological Evolution During Epitaxial Thin Film Growth: Formation of 2d Islands and 3d Mounds". *Surface Science Reports* **61**, 1 (2006).
 - 26 Novoselov, K. S. *et al.* "Electric Field Effect in Atomically Thin Carbon Films". *Science* **306**, 666 (2004).
 - 27 Geim, A. K. & Novoselov, K. S. "The Rise of Graphene". *Nat Mater* **6**, 183 (2007).
 - 28 Allen, M. J., Tung, V. C. & Kaner, R. B. "Honeycomb Carbon: A Review of Graphene". *Chemical Reviews* **110**, 132 (2010).
 - 29 Meyer, J. C. *et al.* "The Structure of Suspended Graphene Sheets". *Nature* **446**, 60 (2007).
 - 30 Nair, R. R. *et al.* "Fine Structure Constant Defines Visual Transparency of Graphene". *Science* **320**, 1308 (2008).

- 31 Li, X. *et al.* "Transfer of Large-Area Graphene Films for High-Performance Transparent Conductive Electrodes". *Nano Letters* **9**, 4359 (2009).
- 32 Ferrari, A. C. "Raman Spectroscopy of Graphene and Graphite: Disorder, Electron–Phonon Coupling, Doping and Nonadiabatic Effects". *Solid State Communications* **143**, 47 (2007).
- 33 Ferrari, A. C. *et al.* "Raman Spectrum of Graphene and Graphene Layers". *Physical Review Letters* **97**, 187401 (2006).
- 34 Hwang, E. H., Adam, S. & Sarma, S. D. "Carrier Transport in Two-Dimensional Graphene Layers". *Physical Review Letters* **98**, 186806 (2007).
- 35 Liu, H., Liu, Y. & Zhu, D. "Chemical Doping of Graphene". *Journal of Materials Chemistry* **21**, 3335 (2011).
- 36 Geim, A. K. & Novoselov, K. S. "The Rise of Graphene". *Nature Materials* **6**, 183 (2007).
- 37 Bolotin, K. I. *et al.* "Ultrahigh Electron Mobility in Suspended Graphene". *Solid State Communications* **146**, 351 (2008).
- 38 Chen, J.-H., Jang, C., Xiao, S., Ishigami, M. & Fuhrer, M. S. "Intrinsic and Extrinsic Performance Limits of Graphene Devices on SiO₂". *Nat Nano* **3**, 206 (2008).
- 39 Novoselov, K. S. *et al.* "Electronic Properties of Graphene". *physica status solidi (b)* **244**, 4106 (2007).
- 40 Morozov, S. V. *et al.* "Giant Intrinsic Carrier Mobilities in Graphene and Its Bilayer". *Physical Review Letters* **100**, 016602 (2008).
- 41 Bunch, J. S. *et al.* "Impermeable Atomic Membranes from Graphene Sheets". *Nano Letters* **8**, 2458 (2008).
- 42 Leenaerts, O., Partoens, B. & Peeters, F. M. "Graphene: A Perfect Nanoballoon". *Applied Physics Letters* **93**, 193107 (2008).
- 43 Reina, A. *et al.* "Large Area, Few-Layer Graphene Films on Arbitrary Substrates by Chemical Vapor Deposition". *Nano Letters* **9**, 30 (2009).
- 44 Kim, K. S. *et al.* "Large-Scale Pattern Growth of Graphene Films for Stretchable Transparent Electrodes". *Nature* **457**, 706 (2009).
- 45 Li, X. *et al.* "Large-Area Synthesis of High-Quality and Uniform Graphene Films on Copper Foils". *Science* **324**, 1312 (2009).
- 46 Gagliardi, G. L., Hans-Peter. in *Springer Series in Optical Sciences* Vol. 179 (ed William T. Rhodes) 527 (Springer, Berlin, 2014).
- 47 Kippenberg, T. J. & Vahala, K. J. "Cavity Optomechanics: Back-Action at the Mesoscale". *Science* **321**, 1172 (2008).
- 48 Baba, T. "Photonic Crystals: Remember the Light". *Nat Photon* **1**, 11 (2007).
- 49 Sandoghdar, V. *et al.* "Very Low Threshold Whispering-Gallery-Mode Microsphere Laser". *Physical Review A* **54**, R1777 (1996).
- 50 Vahala, K. J. "Optical Microcavities". *Nature* **424**, 839 (2003).
- 51 Gomilšek, M. Whispering Gallery Modes. (2011).
- 52 Kuc, A., Zibouche, N. & Heine, T. "Influence of Quantum Confinement on the Electronic Structure of the Transition Metal Sulfide TS₂". *Physical Review B* **83**, 245213 (2011).

- 53 Lee, T.-K. *et al.* "Systematic Analysis of Whispering-Gallery Modes in Planar Silicon Nitride Microdisks". *Optics Communications* **322**, 188 (2014).
- 54 Chhowalla, M. *et al.* "The Chemistry of Two-Dimensional Layered Transition Metal Dichalcogenide Nanosheets". *Nat Chem* **5**, 263 (2013).
- 55 Reed, J. C., Zhu, A. Y., Zhu, H., Yi, F. & Cubukcu, E. "Wavelength Tunable Microdisk Cavity Light Source with a Chemically Enhanced Mos₂ Emitter". *Nano Letters* **15**, 1967 (2015).
- 56 Song, Q., Cao, H., Ho, S. T. & Solomon, G. S. "Near-Ir Subwavelength Microdisk Lasers". *Applied Physics Letters* **94**, 061109 (2009).
- 57 Wang, Q. H., Kalantar-Zadeh, K., Kis, A., Coleman, J. N. & Strano, M. S. "Electronics and Optoelectronics of Two-Dimensional Transition Metal Dichalcogenides". *Nat Nano* **7**, 699 (2012).
- 58 Molina-Sánchez, A. & Wirtz, L. "Phonons in Single-Layer and Few-Layer Mos₂ and Ws₂". *Physical Review B* **84**, 155413 (2011).
- 59 Wilson, J. A. & Yoffe, A. D. "The Transition Metal Dichalcogenides Discussion and Interpretation of the Observed Optical, Electrical and Structural Properties". *Advances in Physics* **18**, 193 (1969).
- 60 Eda, G. *et al.* "Photoluminescence from Chemically Exfoliated Mos₂". *Nano Letters* **11**, 5111 (2011).
- 61 Zeng, Z. *et al.* "Single-Layer Semiconducting Nanosheets: High-Yield Preparation and Device Fabrication". *Angewandte Chemie International Edition* **50**, 11093 (2011).
- 62 Hossein-Zadeh, M. & Vahala, K. J. "Free Ultra-High-Q Microtoroid: A Tool for Designing Photonic Devices". *Optics Express* **15**, 166 (2007).
- 63 Ding, Y. *et al.* "First Principles Study of Structural, Vibrational and Electronic Properties of Graphene-Like Mx₂ (M=Mo, Nb, W, Ta; X=S, Se, Te) Monolayers". *Physica B: Condensed Matter* **406**, 2254 (2011).
- 64 Ataca, C., Şahin, H. & Ciraci, S. "Stable, Single-Layer Mx₂ Transition-Metal Oxides and Dichalcogenides in a Honeycomb-Like Structure". *The Journal of Physical Chemistry C* **116**, 8983 (2012).
- 65 Han, G. H. *et al.* "Seeded Growth of Highly Crystalline Molybdenum Disulphide Monolayers at Controlled Locations". *Nat Commun* **6** (2015).
- 66 Armani, D. K., Kippenberg, T. J., Spillane, S. M. & Vahala, K. J. "Ultra-High-Q Toroid Microcavity on a Chip". *Nature* **421**, 925 (2003).
- 67 Lee, Y.-H. *et al.* "Synthesis of Large-Area Mos₂ Atomic Layers with Chemical Vapor Deposition". *Advanced Materials* **24**, 2320 (2012).
- 68 Zhan, Y., Liu, Z., Najmaei, S., Ajayan, P. M. & Lou, J. "Large-Area Vapor-Phase Growth and Characterization of Mos₂ Atomic Layers on a Sio₂ Substrate". *Small* **8**, 966 (2012).
- 69 Liu, K.-K. *et al.* "Growth of Large-Area and Highly Crystalline Mos₂ Thin Layers on Insulating Substrates". *Nano Letters* **12**, 1538 (2012).
- 70 Tongay, S. *et al.* "Tuning Interlayer Coupling in Large-Area Heterostructures with Cvd-Grown Mos₂ and Ws₂ Monolayers". *Nano Letters* **14**, 3185 (2014).
- 71 Huang, J.-K. *et al.* "Large-Area Synthesis of Highly Crystalline Wse₂ Monolayers and Device Applications". *ACS Nano* **8**, 923 (2014).

- 72 Splendiani, A. *et al.* "Emerging Photoluminescence in Monolayer MoS_2 ". *Nano Letters* **10**, 1271 (2010).
- 73 Mak, K. F., Lee, C., Hone, J., Shan, J. & Heinz, T. F. "Atomically Thin MoS_2 : A New Direct-Gap Semiconductor". *Physical Review Letters* **105**, 136805 (2010).
- 74 Lee, C. *et al.* "Anomalous Lattice Vibrations of Single- and Few-Layer MoS_2 ". *ACS Nano* **4**, 2695 (2010).
- 75 Tonndorf, P. *et al.* "Photoluminescence Emission and Raman Response of Monolayer MoS_2 , MoSe_2 , and WSe_2 ". *Optics Express* **21**, 4908 (2013).
- 76 Berkdemir, A. *et al.* "Identification of Individual and Few Layers of Ws_2 Using Raman Spectroscopy". *Scientific Reports* **3**, 1755 (2013).
- 77 Zeng, H. *et al.* "Optical Signature of Symmetry Variations and Spin-Valley Coupling in Atomically Thin Tungsten Dichalcogenides". *Sci. Rep.* **3** (2013).
- 78 Gutiérrez, H. R. *et al.* "Extraordinary Room-Temperature Photoluminescence in Triangular Ws_2 Monolayers". *Nano Letters* **13**, 3447 (2013).
- 79 Tongay, S. *et al.* "Thermally Driven Crossover from Indirect toward Direct Bandgap in 2d Semiconductors: MoSe_2 Versus MoS_2 ". *Nano Letters* **12**, 5576 (2012).
- 80 Ye, Y. *et al.* Monolayer Excitonic Laser. *ArXiv e-prints* **1503**, 6141 (2015).
- 81 Nan, H. *et al.* "Strong Photoluminescence Enhancement of MoS_2 through Defect Engineering and Oxygen Bonding". *ACS Nano* **8**, 5738 (2014).
- 82 Mouri, S., Miyauchi, Y. & Matsuda, K. "Tunable Photoluminescence of Monolayer MoS_2 Via Chemical Doping". *Nano Letters* **13**, 5944 (2013).
- 83 Sobhani, A. *et al.* "Enhancing the Photocurrent and Photoluminescence of Single Crystal Monolayer MoS_2 with Resonant Plasmonic Nanoshells". *Applied Physics Letters* **104**, 031112 (2014).
- 84 Gan, X. *et al.* "Controlling the Spontaneous Emission Rate of Monolayer MoS_2 in a Photonic Crystal Nanocavity". *Applied Physics Letters* **103**, 181119 (2013).

CHAPTER 2: Graphene-Enabled Silver Nanoantenna Sensors

Adapted with permission from: **J.C Reed**, H. Zhu, A.Y. Zhu, C. Li, and E. Cubukcu, “*Graphene-Enabled Silver Nanoantenna Sensors*”, Nano Letters, **12**, 4090, (2012). Copyright 2012 American Chemical Society.

Silver is the ideal material for plasmonics because of its low loss at optical frequencies, but is often replaced by a more lossy metal, gold. This is because of silver’s tendency to tarnish and roughen, forming Ag_2S on its surface, dramatically diminishing optical properties and rendering it unreliable for applications. By passivating the surface of silver nanostructures with monolayer graphene, atmospheric sulfur containing compounds are unable to penetrate the graphene to degrade the surface of the silver. Preventing this sulfidation eliminates the increased material damping and scattering losses originating from the unintentional Ag_2S layer. Because it is atomically thin, graphene does not interfere with the ability of localized surface plasmons to interact with the environment in sensing applications. Furthermore, after 30 days graphene-passivated silver (Ag-Gr) nanoantennas exhibit a 2600% higher sensitivity over that of bare Ag nanoantennas, and two orders of magnitude improvement in peak width endurance. By employing graphene in this manner, the excellent optical properties and large spectral range of silver can be functionally utilized in a variety of nanoscale plasmonic devices and applications.

2.1 Introduction

Many have studied and continue to study the optical properties of metallic nanoparticles for the collective light-matter interaction phenomenon known as localized surface plasmon resonance (LSPR)^{1,2}. Because of intense local electric field enhancements and sharp resonant extinction peaks, metallic nanoparticles are of great interest for bio/molecular sensors, non-linear optical studies, as well as surface-enhanced Raman spectroscopy³⁻⁷. In the visible regime, silver is the ideal plasmonic metal with lower losses and a higher operation frequency, due to lack of interband absorption, than that of either gold or copper⁸. However, when exposed to ambient air, trace amounts of atmospheric hydrogen sulfide (H_2S) and carbonyl sulfide (OCS) readily react with the surface of the silver, forming Ag_2S ⁹⁻¹². Not only does the sulfidation increase the material loss in the plasmonic nanoantennas, changes to the surface morphology lead to increased surface scattering loss as well^{13,14}.

Because of the chemical instability of silver, gold is often used instead despite having inferior plasmonic properties. While there have been efforts to encapsulate and passivate Ag surfaces to retain its excellent properties, the encapsulating layer is often as thick as or thicker than the nanostructures themselves^{15,16}. This poses a problem for LSPR sensing, as it relies on near-field interactions which are the strongest on the surface of the particle¹⁷. Among its many excellent properties enabling myriad different applications¹⁸⁻²², atomically thin graphene has been proven to be impenetrable to gas molecules as small as helium atoms^{23,24}. Thus, passivating the surface of plasmonic silver nanoparticles (or nanoantennas) with monolayer graphene could prevent the reaction of the silver surface

with sulfur compounds, preserving not only its excellent plasmonic properties, but also its LSPR sensing ability. The rising price of gold also needs to be considered for the commercialization of gold-based devices. Given the 58-times reduction in price of silver (July 2012) over that of gold and the advances in graphene synthesis, economics may drive the next generation of commercial plasmonic devices. Additionally, silver does not suffer from large losses at wavelengths shorter than 600 nm (in contrast to Au or Cu) and can be utilized over the entire visible range⁸.

2.2 Results and Discussion

To test the efficacy of graphene as an effective solution to the problem of silver sulfidation, silver nanoantennas were fabricated with a layer of graphene on top, as illustrated in **Figure 2.1a**. The Ag nanoantennas arrays were fabricated on cleaned glass substrates spin-casted with 50/50 nm of 950/495K molecular weight bilayer poly(methyl methacrylate) (PMMA). A 5 nm layer of Cr was thermally deposited on top of the PMMA to act as a charge dissipation layer. The patterns were written using an Elionix ELS-7500EX e-beam writer. 100x100 μm^2 areas were patterned with circles in a square array. The dimensions of the nanoantennas were 115 nm in diameter and 300 nm in interparticle spacing. After e-beam writing, the Cr layer was etched away using Transene Cr Etch 1020 and the samples developed in 1:3 methyl isobutyl ketone (MIBK) : isopropanol (IPA) for 60 seconds. After brief O₂ plasma cleaning, the samples were placed into an e-beam evaporator to deposit 3/30 nm of Ge/Ag. Acetone was used for metal liftoff with 10 s of sonication after a 30 minute soak.

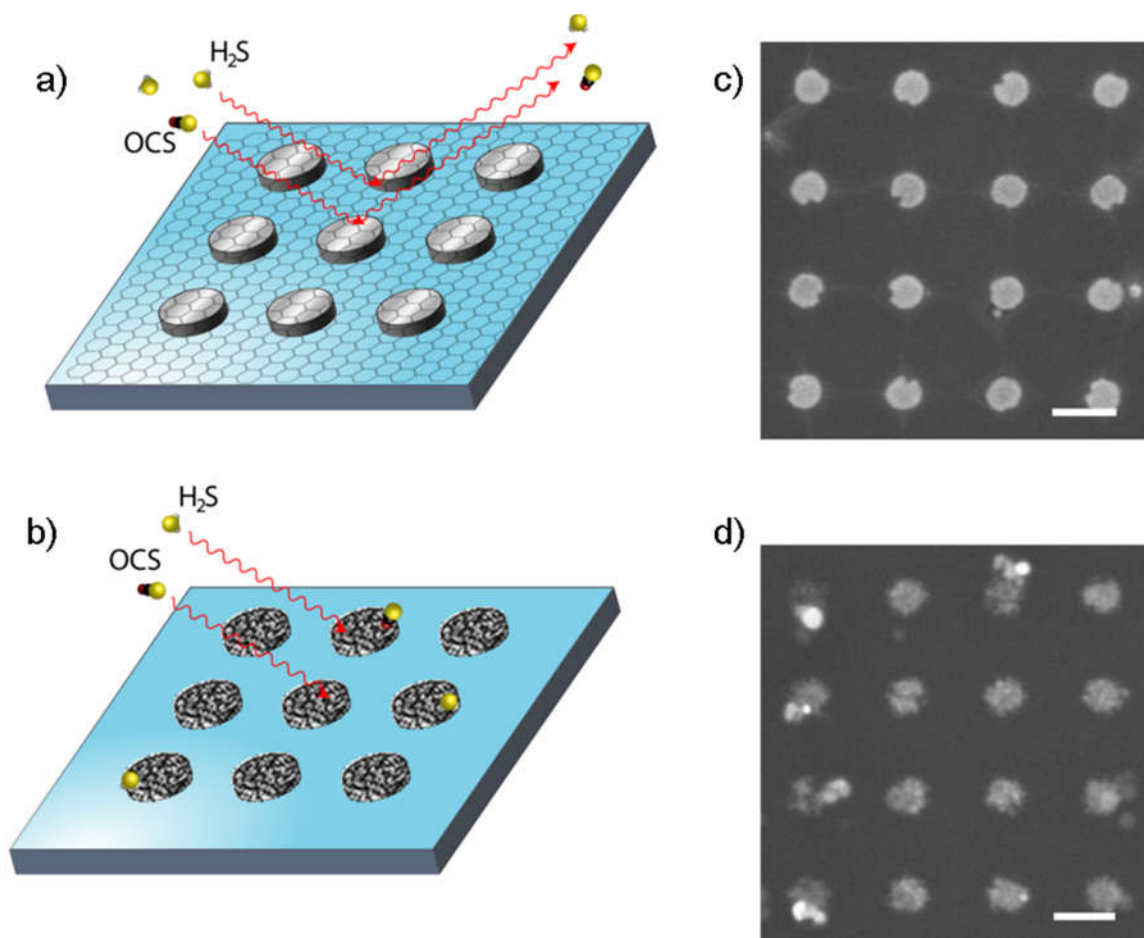


Figure 2.1 (a) Illustration of graphene-passivated Ag nanoantennas fabricated in a square array. The graphene layer prevents the reaction of trace atmospheric H_2S and OCS with the surface of the Ag. (b) Illustration of bare Ag nanoantennas fabricated similarly. The lack of graphene allows the atmospheric sulfur compounds to react with the silver. SEM images of (c) graphene-passivated Ag nanoantennas and (d) bare Ag nanoantennas after 30 days; scale bars are 200 nm.

Two silver nanoantenna arrays were identically fabricated. One of the nanoantenna arrays was covered with a layer of graphene while the second was left as bare Ag (**Figure 2.1b**). To transfer the graphene, CVD-grown graphene on copper foil was used as purchased (Graphene Supermarket). Following the methods of Ruoff *et al.*^{25,26}, PMMA (350K MW at 45mg/mL in anisole) was spin-cast (4000 RPM, 45s) onto the foil before etching the Cu foil with 1M iron chloride solution for 45 minutes at 75°C.

The PMMA/graphene film was then transferred to deionized water and washed multiple times. The graphene layer was then transferred to the Ag nanoantennas sample immediately after Ag metal liftoff and allowed to dry in vacuum. After drying, a drop of the PMMA solution was added and allowed to re-cure for 30 minutes in air before washing multiple times in acetone/IPA. The total time in ambient air after Ag film deposition and graphene coverage was one hour. Sulfidation of nanoscale Ag can be as much as 3 nm/day⁹, leading to, at most, a 1 Å layer of sulfide formation before graphene coverage. The two samples were then stored in ambient laboratory environment for 30 days. As shown in **Figure 2.1c**, the Ag nanoantennas covered by graphene did not show signs of sulfidation; the surfaces of the particles were smooth and kept their circular shape. Bare Ag nanoantennas, as seen in **Figure 2.1d**, show large morphological changes to the disks. The presence of sulfur on the surface of the unpassivated nanoparticles has also been confirmed through energy-dispersive x-ray spectroscopy (EDX) (**Figure 2.2**). Bare Ag nanoantennas showed a sulfur peak in the EDX data, while graphene-passivated Ag nanoantennas lacked that peak in the spectrum.

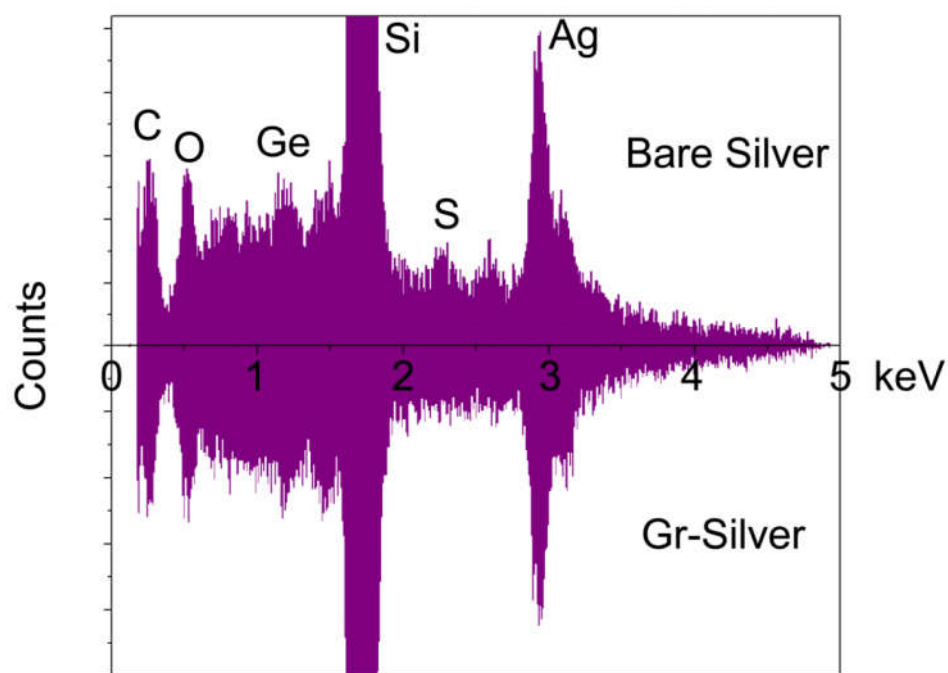


Figure 2.2 Energy dispersive x-ray spectroscopy (EDX) of unpassivated as well as graphene-passivated Ag (Gr-Silver) nanoantennas after 30 days of air exposure. The spectrum for the unpassivated Ag particles shows a sulfur peak from the sulfide formation, whereas such a peak is absent from that of passivated Ag.

The graphene passivation of the silver nanoantennas has a dramatic effect on its optical properties and morphology. The morphological changes that are prevented by the graphene passivation can be seen even within the same sample array. Particles covered by graphene show no signs of morphology changes, while those left uncovered by cracks in the graphene film show large changes in morphology (**Figure 2.3**). This is also true for continuous Ag films (**Figure 2.4**), where a well-defined boundary of sulfidation and surface roughness change formed at the edge of the graphene layer.

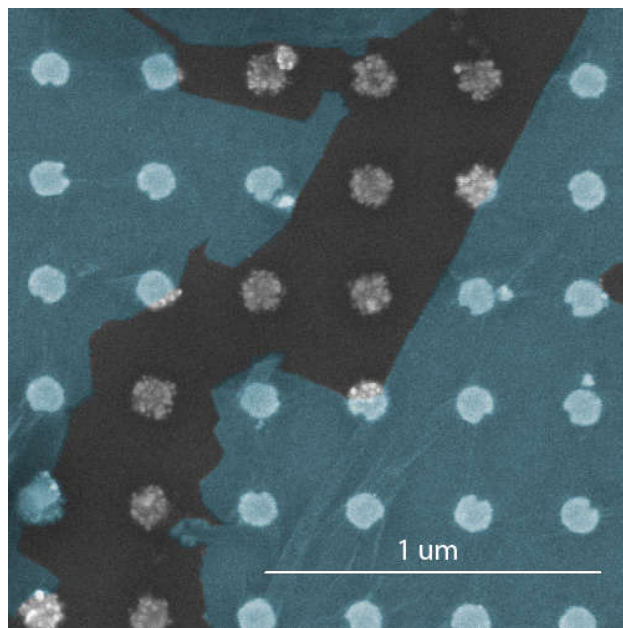


Figure 2.3 An SEM image of an Ag nanoantennas array covered by graphene (colorized in blue). Statistical cracks in the monolayer film lead to small areas of uncovered nanoantennas (uncolored), where the Ag shows significant morphological changes from the exposure to sulfur compounds. The graphene-covered nanoantennas are protected from this chemical degradation. Partially covered nanoantennas show partial sulfidation.

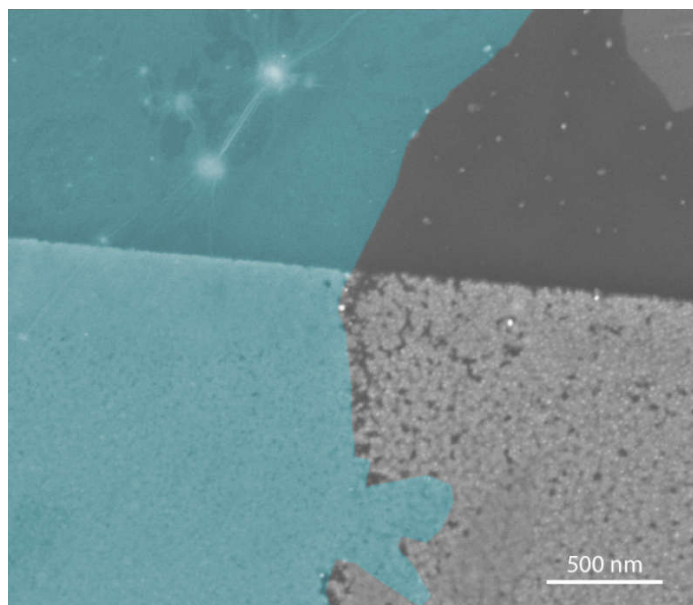


Figure 2.4 An SEM image of an edge of a continuous Ag thin film partially covered by graphene (colorized blue). The area covered by graphene has a smooth edge, while the uncovered (uncolored) area shows the roughness changes through sulfidation.

The optical spectra of the nanoparticle arrays were measured over 30 days in order to study how well graphene passivation retained the properties of Ag. Reflection spectra of the nanoantennas were taken using a homemade free-space microscope. A fiber-coupled light source (Ocean Optics LS-1) was collimated using a lens before passing through a 50:50 beam splitter. The light passed through a 50x objective (Mitutoyo, 0.42 NA) and focused onto the surface of the sample. The reflected light passed back through the objective and beam splitter and was imaged by a tube lens (Mitutoyo) and focused by a 10x objective (Olympus, 0.25 NA) into a fiber-coupled CCD spectrometer (Thor Labs CCS175). All measurements were normalized to the substrate without nanoantennas and sampled using 50 ms exposure time, 50x spectrum averaging and 50x boxcar averaging. **Figure 2.5a** shows the temporal evolution of the spectrum for graphene-passivated Ag nanoantennas, while **Figure 2.5b** shows that of as-fabricated Ag nanoantennas. Over a 30 day period, both the resonant peak position, λ_{max} (**Figure 2.5c**), as well as the resonant peak width, $\Delta\lambda$ (**Figure 2.5d**), increased dramatically for unpassivated Ag nanoantennas. In contrast, the Ag nanoantennas that were passivated by the graphene showed a much more robust preservation of the initial plasmonic properties. The shift in λ_{max} for the unpassivated Ag nanoantennas was 216 nm compared to 15 nm for that of graphene-passivated Ag nanoantennas. The increase in the peak width for bare Ag nanoantennas was 1748 nm, while only 11 nm for that of passivated Ag nanoantennas.

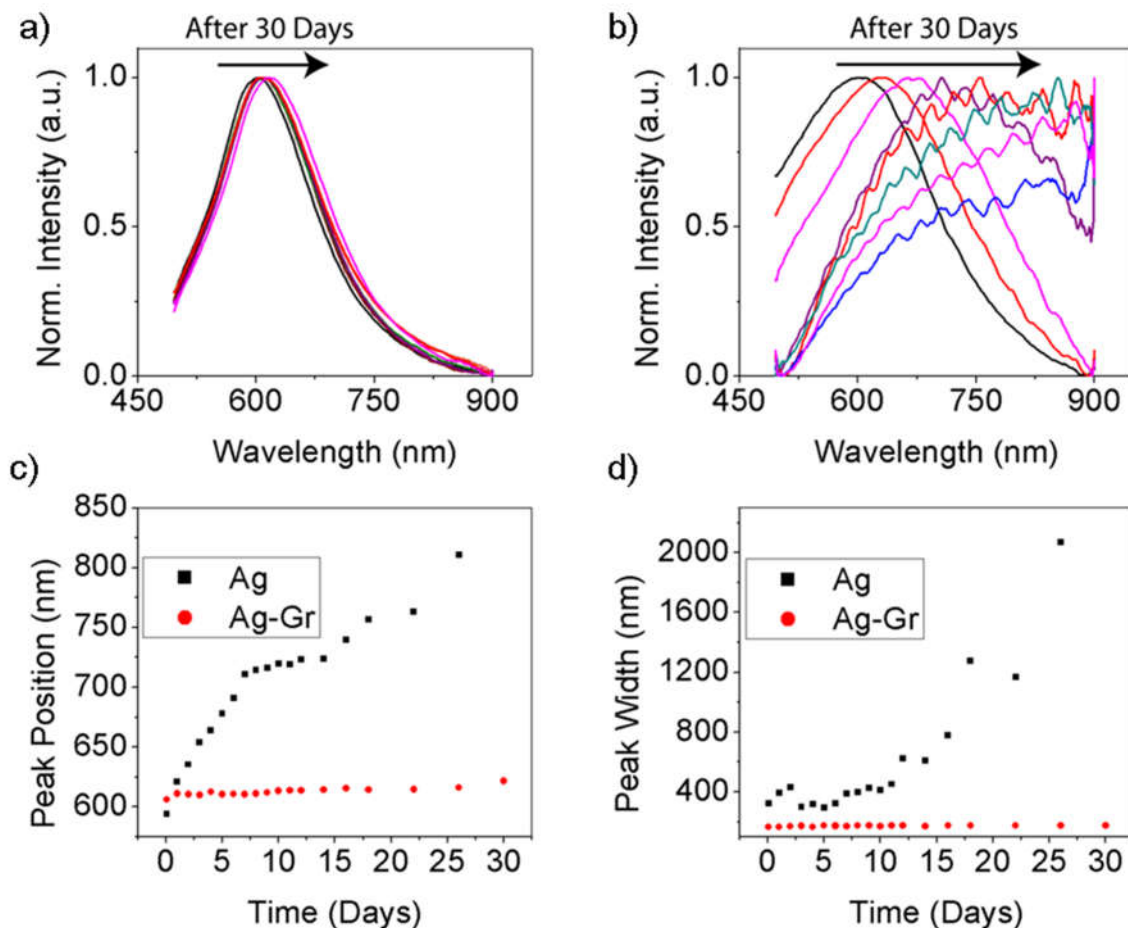


Figure 2.5 Normalized reflection spectra of (a) graphene-passivated Ag and (b) bare Ag nanoantennas over the course of 30 days. Time evolution of the (c) resonance peak position and the (d) resonance peak width for both graphene-passivated and bare Ag nanoantennas over 30 days.

The usefulness of plasmonic resonances for sensing applications depends highly upon the peak width. The graphene-passivated Ag nanoantennas show about a 160 fold resistance to peak width increases over the 30 day period. Additionally, the sensitivity to small shifts in the spectrum can be quantified by the slope of the resonant spectra ($dI/d\lambda$). After the 30 day period, the graphene-passivated Ag showed a 2600% higher $dI/d\lambda$ over that of unpassivated silver (**Figure 2.6**). Because of the impenetrability of graphene to

sulfur species, it is believed that any degradation of the optical properties for graphene-passivated Ag nanoantennas is a result of imperfect graphene coverage of the nanoantennas across the $100 \times 100 \mu\text{m}^2$ array. Cracks in the graphene sheet cause a small fraction of the nanoantennas to remain unpassivated, leading to some degradation even in the graphene protected sample. The cracks resulting from the graphene transfer process accounts for approximately 2% of the graphene area (**Figure 2.7**).

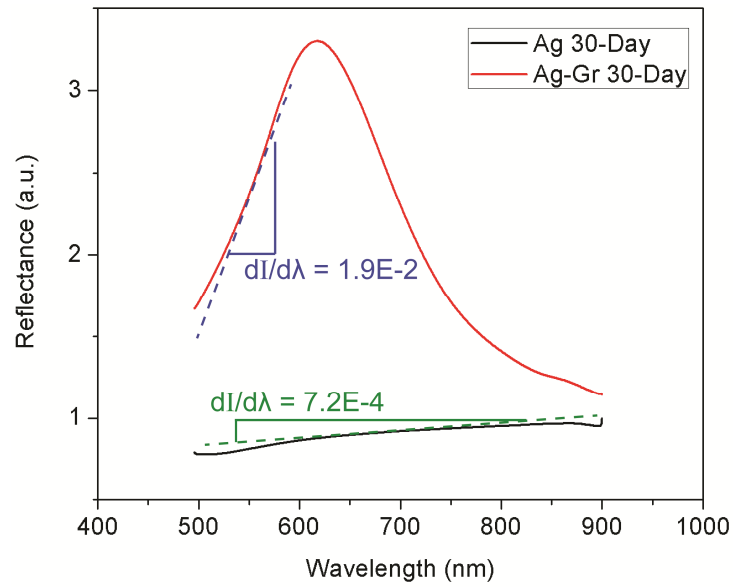


Figure 2.6 Optical reflectance spectra of bare Ag and graphene-passivated silver (Ag-Gr) nanoantennas after 30 days in ambient conditions. The slopes ($dI/d\lambda$) show the sensitivity of the array to small shifts. The well preserved Ag-Gr nanoantennas show a 2600% improvement in $dI/d\lambda$ over 30 days.

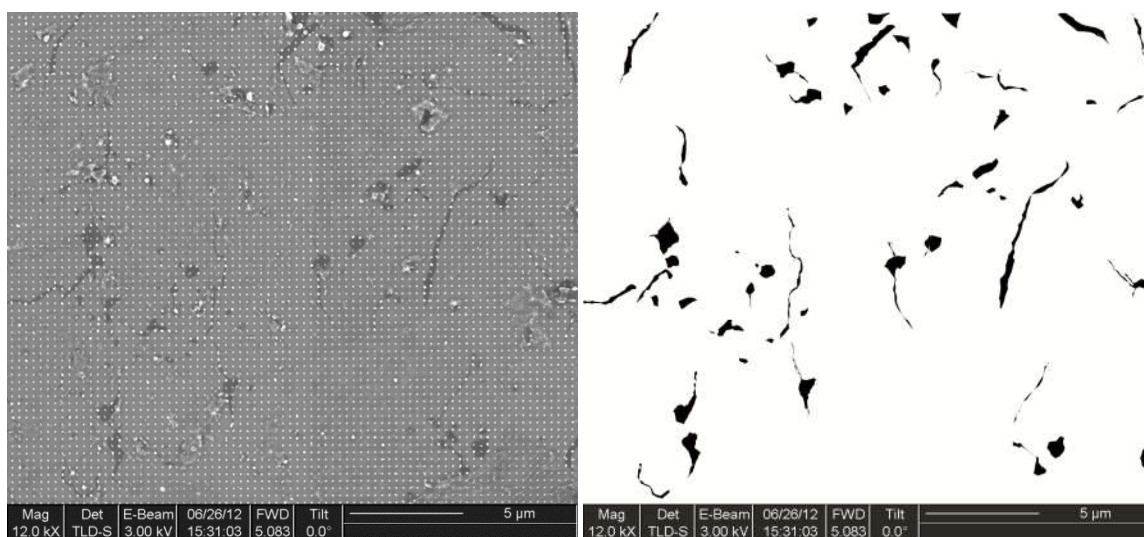


Figure 2.7 SEM Image of a representative transferred graphene layer on top of Ag nanoantennas (left). The cracks in the graphene layer were highlighted (right) and analyzed to be ~2% of the overall area.

Raman spectroscopy was used to confirm the presence of graphene on the surface of the nanoantennas. **Figure 2.8a** shows the Raman spectra sampled on the Ag nanoantennas as well as on the substrate. Both spectra show the G-and 2D-bands with a higher intensity 2D band, suggesting monolayer graphene²⁷. The wide peak around the G-band for the Raman signal on the Ag nanoantennas comes from the fluorescence from the nanoantennas themselves. The data also shows about an order of magnitude enhancement in the Raman signal of the graphene when sampled on top of the nanoantennas in comparison to graphene just on glass. A Raman map highlighting the intensity of the 2D-band (**Figure 2.8b**) clearly shows the collective enhancement of the graphene Raman signal from the nanoantennas within the boundaries of the array.

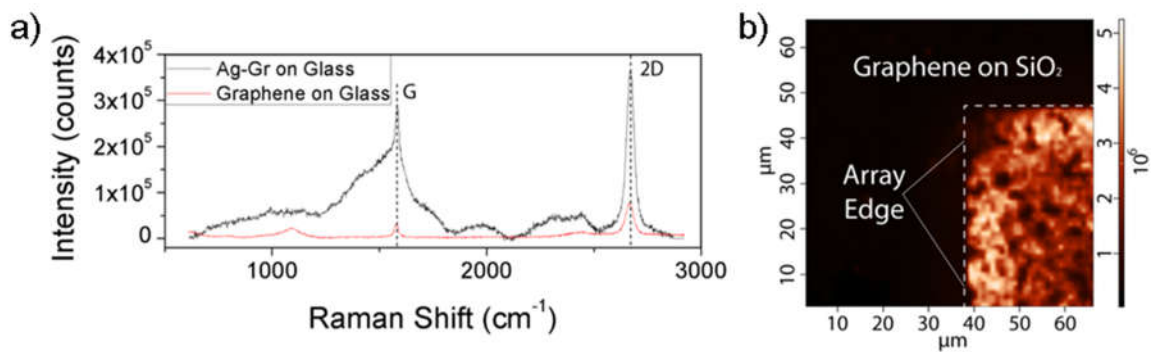


Figure 2.8 (a) Raman spectra of graphene both on and off of the Ag nanoantenna array, with the relative intensities of the G and 2D bands suggest monolayer graphene. (b) Raman intensity map of the 2D band on the corner of a Ag nanoantennas array, showing the relative enhancement.

One of the main concerns about protective layers on LSPR sensors is the detrimental effect it has on the sensitivity to local refractive index changes. Because graphene is only 0.355 nm thick²⁸, it should not hinder LSPR sensing ability of the nanoantennas that is highly sensitive but also highly localized. For bulk refractive index sensing, similarly fabricated array samples were made that were 110 nm in diameter and 250 nm in interparticle spacing. To compare the Ag-Gr nanoantennas with that of Au nanoantennas, the second sample in this study was deposited with 3/30 nm Ti/Au in place of the Ag-Gr film. These were then put into poly(dimethylsiloxane) (PDMS) fluid cells with refractive index matching liquids (Cargille, Series AA). The samples were washed with acetone/IPA between each refractive index liquid to ensure no residual chemical remained on the sample. **Figure 2.9a** shows the peak shift from air ($n=1.00$) of both Ag-Gr and Au nanoantennas for a very fine and controlled refractive index range ($n=1.40$ - 1.45), proving that graphene-passivated nanoantennas retain their ability to sense small local refractive index changes. The error bars signify one standard deviation in the peak

position over 20 individual, identical $100 \times 100 \text{ } \mu\text{m}^2$ arrays for each index. Measuring the resonance peak shift as a function of the index, the bulk sensitivity of the LSPR sensor from the slope of **Figure 2.9a**, $d\lambda/dn$, can be determined. For graphene-passivated Ag nanoantennas, $d\lambda/dn = 162$, while $d\lambda/dn = 102$ for Au nanoantennas. This yields ~60% increase in bulk sensitivity for Ag-Gr over that of bare Au nanoantennas. Using finite-difference time-domain (FDTD) calculations, the effect of bulk index changes on both Ag-Gr as well as bare gold nanoantennas was studied. FDTD simulations were done using a software package (Lumerical 7.5.4) on both Au and Ag-Gr plasmonic structures of similar dimensions as in the experimental case. Optical data for graphene was taken from work by Gray *et al.*²⁹, while the data for Au and Ag was taken from Palik³⁰. A plane wave source was introduced and the reflected power flux as a function of frequency was measured for both cases with varying bulk index of the background ranging from 1.38-1.47 RIU. Additionally, the field intensity profile was taken across the middle of the 30 nm Ag-Gr simulation, showing the field enhancement. **Figure 2.9b** shows the results of the simulations; the sensitivity toward bulk index change is 148 for Ag-Gr and 83 for Au nanoantennas. The simulations give rise to ~80% increase in bulk sensitivity of Ag-Gr over that of Au.

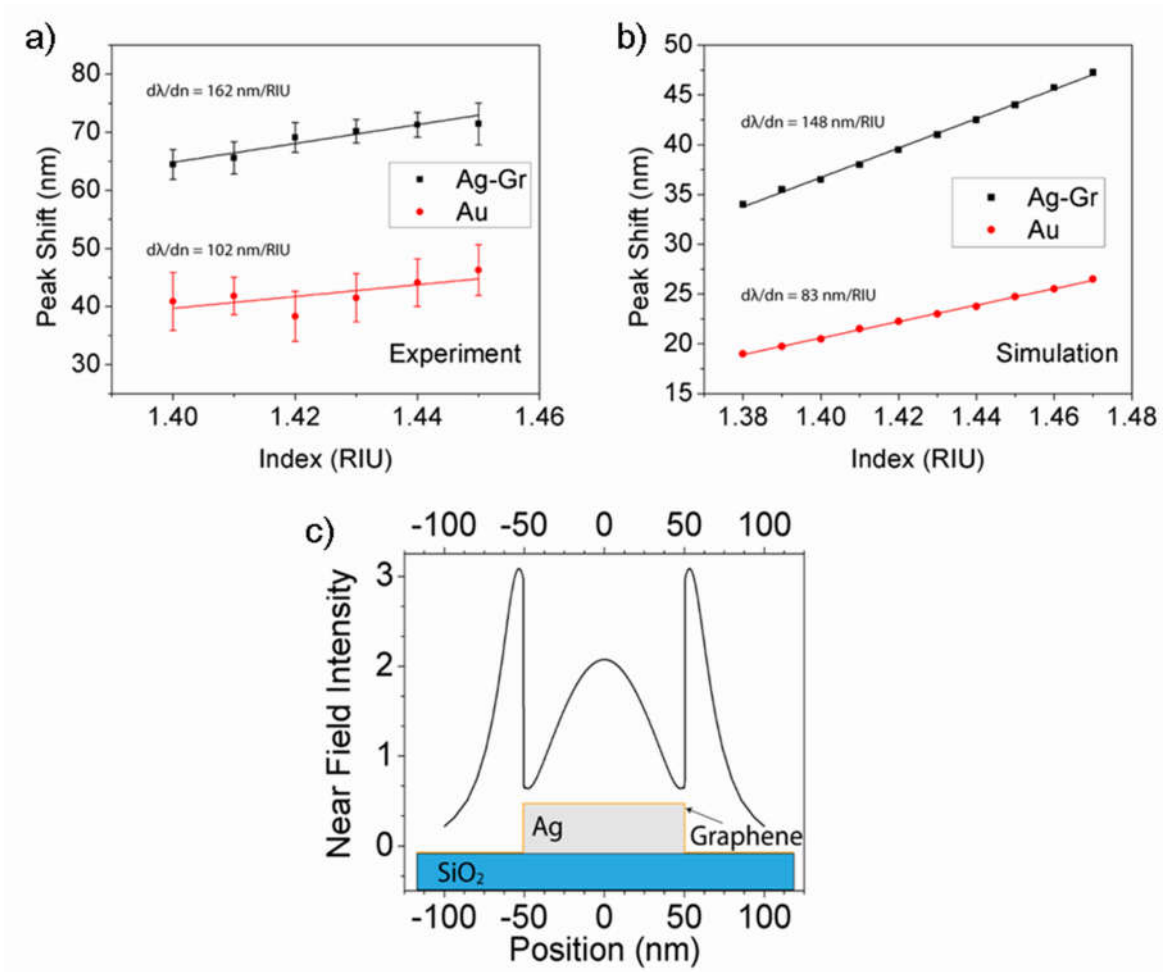


Figure 2.9 The sensitivity of both graphene-passivated silver as well as gold nanoantennas arrays of the same dimensions to bulk index changes over a small index range. (a) Experimental data for the change in peak wavelength with index, showing a bulk sensitivity ($d\lambda/dn$) of 241 for Ag-Gr and 186 for bare Au. (b) Theoretical data from FDTD simulations showing a $d\lambda/dn$ of 142 for Ag-Gr and 98 for bare Au. (c) Plot of nearfield intensity profile from FDTD simulations of graphene-passivated silver nanoantennas as a function of position. The local enhancement of the electric field decays exponentially with a constant of 16.5 nm from the surface of the particle.

For bulk sensitivity measurements, the results show that the graphene-passivated silver nanoantennas were better at sensing bulk index changes than bare gold nanoantennas. The experimental 60% increase matched well with the 80% increase of the FDTD simulations. Such a result was expected because of the better plasmonic properties

of silver. This also matches previous work that numerically shows the same order of magnitude increase in sensitivity of graphene-passivated silver versus that of gold for surface plasmon resonance (SPR) sensing³¹. The increased bulk sensitivity of Ag-Gr nanoantennas, means that Ag-Gr can be used for sensors with a much higher resolution.

The FDTD simulations also show the local electric field enhancement around the Ag-Gr nanoantennas (**Figure 2.9c**), with the inset showing the corresponding size of the particle in the lateral direction. The field enhancement is about three times at the edge of the particle and decays exponentially with a decay constant of 16.5 nm for this system. This shows two things. One is that the graphene layer does not limit the sensing abilities of silver particles as the field still extends tens of nanometers from the surface. The second is that only a very thin and impermeable passivation layer is applicable in this system, such as monolayer graphene. Polymeric or ceramic passivation layers need to be on the order of hundreds⁹ or tens¹⁵ of nanometers in thickness, respectively. Given the fast decay of the localized field, such thick layers would hamper the sensing ability of the nanoantennas. The hexagonal structure of graphene and delocalized π -bonds can attract and adsorb various biomolecules³², making graphene a potential adsorption layer for molecular sensing³³. Additionally, graphene can be converted to graphene oxide with a large number of surface functional groups that can be tailored to individual molecular sensing applications^{34,35}.

To find the theoretical effects of sulfidation, an extension of the quasistatic Mie theory known as the modified long wavelength approximation (MLWA) was used in order to incorporate the radiation damping and depolarization effects. For theoretical

scattering data, a mathematical package (Mathematica 8) was used with calculations based on the MLWA, as reported by Kelly *et al.*³⁶. The far field scattering spectra of the theoretical Ag oblate spheroids when coated with varying thicknesses of Ag₂S were obtained through this method. Following established literature, it was assumed that the conversion of Ag into Ag₂S occurs uniformly with a conversion ratio of 1:1.6⁹. The Ag₂S and Ag optical data were obtained from Bennett *et al.*³⁷ and Palik³⁰, respectively. The size and geometry of the spheroids were chosen such that they best approximated the behavior and resonance wavelengths of the actual Ag discs used experimentally; here the minor axis was chosen to be 12.5 nm to have a 600 nm resonance peak. **Figure 2.10a** shows the calculated scattering intensities with an increasing uniform shell of Ag₂S around a Ag core in the spheroid. Both peak width and peak position as a function of Ag₂S shell thickness is shown in **Figure 2.10b**. Peak position increases roughly linearly with a slight plateau, whereas the peak width plateaus at a much faster rate.

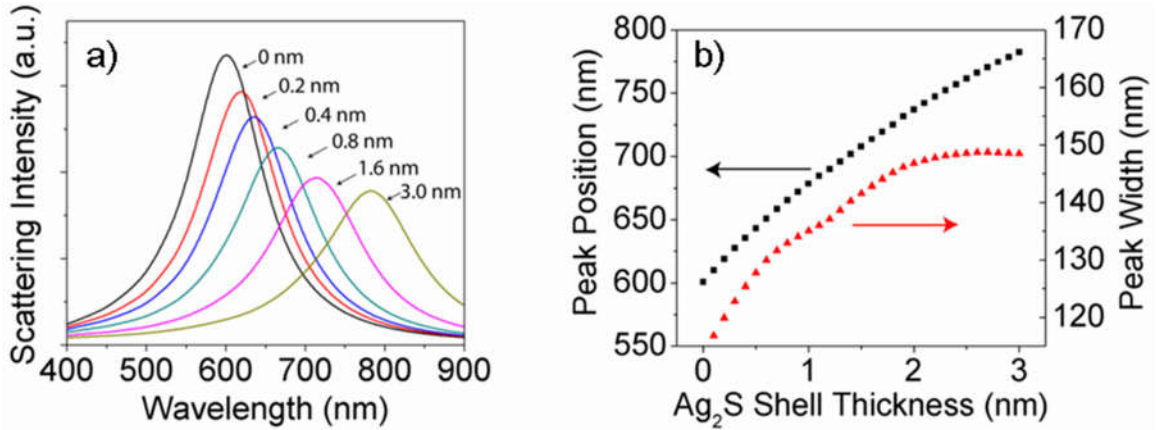


Figure 2.10 (a) Scattering intensity of Ag oblate spheroids with varying shell thickness of Ag₂S calculated with the MLWA. (b) Scattering peak position as well as peak width derived from the calculated scattering spectra.

From the theoretical scattering data, the general trend of increasing peak positions and line widths follows that of the aforementioned experimental data; however the rate at which it does so is different. This discrepancy can be explained by the morphological changes in the fabricated Ag nanoantennas. In **Figure 2.5c**, the resonance peak position for bare Ag nanoantennas increases at three different rates: a relatively steep rise, a plateau, and then another relatively steep rise. Based on the observations of Elechiquerra *et al.*¹², that the first steep rise in the LSPR peak position corresponds to a formation of silver sulfide crystallites around the Ag core. The larger index of Ag_2S causes the nanoantenna arrays to experience a red shift in the optical response, hence a steep rise in days 0-10. The plateau during days 10-14 corresponds to a period in which clusters of Ag_2S coalesce into a very rough shell of sulfide. The rough shell slowly grows and causes a relatively small red shift of the spectra, but continue to increase the scattering loss, as seen in the increased peak width in **Figure 2.5d**. After day 14, the particles begin to break apart and fragment, leading to another large increase in the peak position. More significantly, the breaking up of the nanoantennas causes a substantial increase in the peak widths. This splintering of the Ag nanoantenna is thought to be the result of changes in the crystal structure^{9,11} or through diffusive processes¹⁴. It is believed that this is also the cause of the large increase in resonance peak width, even larger than that of theoretical values. Breaking of the nanoantennas would not only serve to enhance the rate of sulfidation, but as well as dramatically increase scattering losses that lead to broadening of the optical spectrum. The morphological changes in the nanoantennas as a function of time can be seen in **Figure 2.11**.

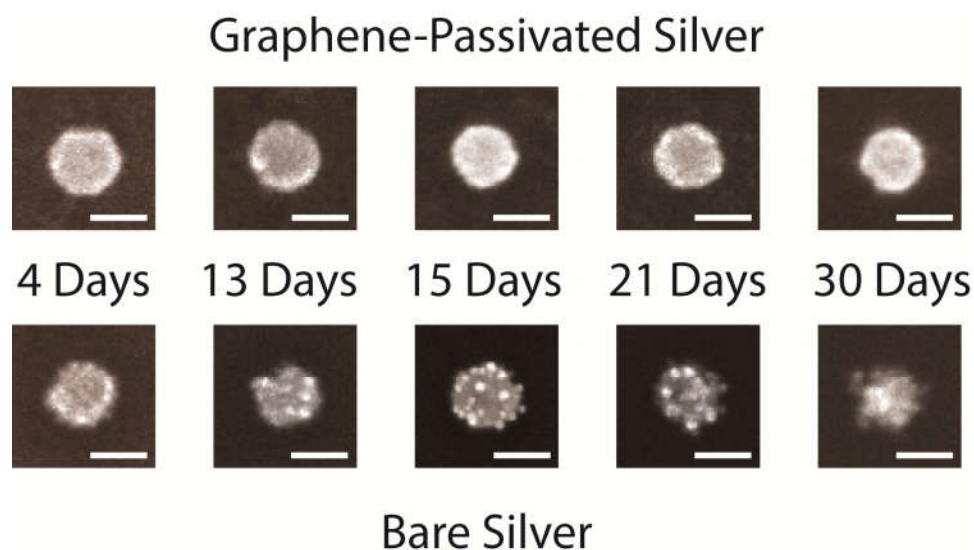


Figure 2.11 SEM images of individual silver nanoantennas passivated by graphene (top row) and unpassivated (bottom row) over the course of 30 days. Scale bars are 100 nm.

2.3 Conclusions

In summary, by passivating the surface of Ag nanoantennas with graphene, we demonstrate that the sulfidation of the silver surface that degrades its excellent optical properties can be prevented by effectively blocking diffusion of gas molecules through a transferred monolayer graphene film. It is strongly believed that silver-based LSPR and SPR sensors and applications can now be significantly more useful, especially over long time frames without hindering near-field sensing. This method has the potential to be widely applicable to other plasmonic material systems otherwise rendered useless through chemical reactivity, such as Al or Cu nanoantennas. Not only are Al and Cu several orders of magnitude less expensive than gold, they both have different functional regimes for plasmonic sensors that can be enabled through graphene. Al is active in deep-UV spectrum while Cu in near-IR. Thus, graphene passivation of metal nanoantennas has

the potential to open up a wide range of plasmonic applications for reactive materials beyond silver alone.

2.4 References

- 1 Jensen, T. R., Malinsky, M. D., Haynes, C. L. & Van Duyne, R. P. "Nanosphere Lithography: Tunable Localized Surface Plasmon Resonance Spectra of Silver Nanoparticles". *The Journal of Physical Chemistry B* **104**, 10549 (2000).
- 2 Xu, H., Aizpurua, J., Käll, M. & Apell, P. "Electromagnetic Contributions to Single-Molecule Sensitivity in Surface-Enhanced Raman Scattering". *Physical Review E* **62**, 4318 (2000).
- 3 Haes, A. J. & Van Duyne, R. P. "A Nanoscale Optical Biosensor: Sensitivity and Selectivity of an Approach Based on the Localized Surface Plasmon Resonance Spectroscopy of Triangular Silver Nanoparticles". *Journal of the American Chemical Society* **124**, 10596 (2002).
- 4 Hache, F., Ricard, D. & Flytzanis, C. "Optical Nonlinearities of Small Metal Particles: Surface-Mediated Resonance and Quantum Size Effects". *Journal of the Optical Society of America B: Optical Physics* **3**, 1647 (1986).
- 5 Nie, S. & Emory, S. R. "Probing Single Molecules and Single Nanoparticles by Surface-Enhanced Raman Scattering". *Science* **275**, 1102 (1997).
- 6 Pryce, I. M., Kelaita, Y. A., Aydin, K. & Atwater, H. A. "Compliant Metamaterials for Resonantly Enhanced Infrared Absorption Spectroscopy and Refractive Index Sensing". *ACS Nano* **5**, 8167 (2011).
- 7 Adato, R. *et al.* "Ultra-Sensitive Vibrational Spectroscopy of Protein Monolayers with Plasmonic Nanoantenna Arrays". *Proceedings of the National Academy of Sciences* **106**, 19227 (2009).
- 8 West, P. R. *et al.* "Searching for Better Plasmonic Materials". *Laser & Photonics Reviews* **4**, 795 (2010).
- 9 McMahon, M., Lopez, R., Meyer, H., Feldman, L. & Haglund, R. "Rapid Tarnishing of Silver Nanoparticles in Ambient Laboratory Air". *Applied Physics B: Lasers and Optics* **80**, 915 (2005).
- 10 Cao, W. & Elsayed-Ali, H. E. "Stability of Ag Nanoparticles Fabricated by Electron Beam Lithography". *Materials Letters* **63**, 2263 (2009).
- 11 Huang, T., Cao, W., Elsayed-Ali, H. E. & Xu, X.-H. N. "High-Throughput Ultrasensitive Characterization of Chemical, Structural and Plasmonic Properties of Ebl-Fabricated Single Silver Nanoparticles". *Nanoscale* **4**, 380 (2012).
- 12 Elechiguerra, J. L. *et al.* "Corrosion at the Nanoscale: The Case of Silver Nanowires and Nanoparticles". *Chemistry of Materials* **17**, 6042 (2005).
- 13 Nagpal, P., Lindquist, N. C., Oh, S.-H. & Norris, D. J. "Ultrasmooth Patterned Metals for Plasmonics and Metamaterials". *Science* **325**, 594 (2009).
- 14 Wang, L. *et al.* "Spectral Properties and Mechanism of Instability of Nanoengineered Silver Blocks". *Optics Express* **19**, 10640 (2011).

- 15 Park, Y.-i., Cha, S.-w., Saito, Y. & Prinz, F. B. "Gas-Tight Alumina Films on Nanoporous Substrates through Oxidation of Sputtered Metal Films". *Thin Solid Films* **476**, 168 (2005).
- 16 Barrios, C. A., Malkovskiy, A. V., Kisliuk, A. M., Sokolov, A. P. & Foster, M. D. "Highly Stable, Protected Plasmonic Nanostructures for Tip Enhanced Raman Spectroscopy". *The Journal of Physical Chemistry C* **113**, 8158 (2009).
- 17 Hall, W. P. *et al.* "A Conformation- and Ion-Sensitive Plasmonic Biosensor". *Nano Letters* **11**, 1098 (2011).
- 18 Geim, A. K. & Novoselov, K. S. "The Rise of Graphene". *Nature Materials* **6**, 183 (2007).
- 19 Wang, X. *et al.* "Room-Temperature All-Semiconducting Sub-10-Nm Graphene Nanoribbon Field-Effect Transistors". *Physical Review Letters* **100**, 206803 (2008).
- 20 Bunch, J. S. *et al.* "Electromechanical Resonators from Graphene Sheets". *Science* **315**, 490 (2007).
- 21 Stoller, M. D., Park, S., Zhu, Y., An, J. & Ruoff, R. S. "Graphene-Based Ultracapacitors". *Nano Letters* **8**, 3498 (2008).
- 22 Kim, K. S. *et al.* "Large-Scale Pattern Growth of Graphene Films for Stretchable Transparent Electrodes". *Nature* **457**, 706 (2009).
- 23 Leenaerts, O., Partoens, B. & Peeters, F. M. "Graphene: A Perfect Nanoballoon". *Applied Physics Letters* **93**, 193107 (2008).
- 24 Bunch, J. S. *et al.* "Impermeable Atomic Membranes from Graphene Sheets". *Nano Letters* **8**, 2458 (2008).
- 25 Chen, S. *et al.* "Thermal Conductivity of Isotopically Modified graphene". *Nature Materials* **11**, 203 (2012).
- 26 Li, X. *et al.* "Transfer of Large-Area Graphene Films for High-Performance Transparent Conductive Electrodes". *Nano Letters* **9**, 4359 (2009).
- 27 Ni, Z. H. *et al.* "Graphene Thickness Determination Using Reflection and Contrast Spectroscopy". *Nano Letters* **7**, 2758 (2007).
- 28 Gupta, A., Chen, G., Joshi, P., Tadigadapa, S. & Eklund, "Raman Scattering from High-Frequency Phonons in Supported N-Graphene Layer Films". *Nano Lett.* **6**, 2667 (2006).
- 29 Gray, A., Balooch, M., Allegret, S., De Gendt, S. & Wang, W.-E. "Optical Detection and Characterization of Graphene by Broadband Spectrophotometry". *Journal of Applied Physics* **104**, 053109 (2008).
- 30 Palik, E. D. *Handbook of Optical Constants of Solids*. (Academic Press, 1985).
- 31 Choi, S. H., Kim, Y. L. & Byun, K. M. "Graphene-on-Silver Substrates for Sensitive Surface Plasmon Resonance Imaging Biosensors". *Optics Express* **19**, 458 (2011).
- 32 Song, B. *et al.* "Graphene on Au(111): A Highly Conductive Material with Excellent Adsorption Properties for High-Resolution Bio/Nanodetection and Identification". *ChemPhysChem* **11**, 585 (2010).
- 33 Papasimakis, N. *et al.* "Graphene in a Photonic Metamaterial". *Optics Express* **18**, 8353 (2010).

- 34 Han, T. H., Huang, Y.-K., Tan, A. T. L., Dravid, V. P. & Huang, J. "Steam Etched Porous Graphene Oxide Network for Chemical Sensing". *Journal of the American Chemical Society* **133**, 15264 (2011).
- 35 Li, F., Feng, Y., Zhao, C., Li, P. & Tang, B. "A Sensitive Graphene Oxide-DNA Based Sensing Platform for Fluorescence "Turn-on" Detection of Bleomycin". *Chemical Communications* **48**, 127 (2012).
- 36 Kelly, K. L., Coronado, E., Zhao, L. L. & Schatz, G. C. "The Optical Properties of Metal Nanoparticles: The Influence of Size, Shape, and Dielectric Environment". *The Journal of Physical Chemistry B* **107**, 668 (2002).
- 37 Bennett, J. M., Stanford, J. L. & Ashley, E. J. "Optical Constants of Silver Sulfide Tarnish Films". *Journal of the Optical Society of America* **60**, 224 (1970).

CHAPTER 3: Wavelength Tunable Microdisk Cavity Light Source with a Chemically Enhanced MoS₂ Emitter

Adapted with permission from: J.C Reed, A. Y. Zhu, H. Zhu, F. Yi, and E. Cubukcu, “Wavelength Tunable Microdisk Cavity Light Source with a Chemically Enhanced MoS₂ Emitter”, *Nano Letters*, **15**, 1967, (2015). Copyright 2015 American Chemical Society.

In this work, we report an integrated narrowband light source based on thin MoS₂ emissive material coupled to the high quality factor whispering gallery modes of a microdisk cavity with a spatial notch enabling easy out-coupling of emission while yielding high spatial coherence and a Gaussian intensity distribution. The active light emitting material consists of chemically enhanced bilayer MoS₂ flakes with a thin atomic layer deposited SiO₂ protective coating yielding 20 times brighter chemically enhanced photoluminescence compared to as-exfoliated monolayers on the microdisk. Quality factors ~1000 are observed as well as a high degree of spatial coherence. We also experimentally achieve effective index tuning of cavity coupled emission over a full free spectral range. The thermal response of this system is also studied. This work provides new insights for nanophotonic light sources with atomically thin active media.

3.1 Introduction

Transition to a direct electronic bandgap in emerging transition metal dichalcogenide (TMDC) materials at the monolayer limit has enabled novel optoelectronic devices such as photodetectors, solar cells, and light-emitting diodes, which take advantage of neutral and charged excitons in these 2-D semiconductors.¹⁻⁴

Arguably, one of the most prominent applications of bulk direct bandgap semiconductors is integrated photonic light sources based on optical waveguides and resonators.⁵⁻⁷ However, such integrated photonic devices based on 2-D semiconductors that may potentially form the discrete components of future optoelectronic systems are yet to be explored. Here, we demonstrate a wavelength tunable integrated narrowband light source enabled by chemically enhancing MoS₂ emission. A sub-wavelength notch coupler integrated into a microdisk cavity with high quality-factor (Q) whispering gallery modes (WGMs), enables easy extraction of MoS₂ emission while yielding high spatial and temporal coherence. We envision that this work will pave the way for nanophotonic light sources with atomically thin active media for next generation optoelectronic sensors and systems.

Among other emerging 2D materials, naturally occurring molybdenum disulfide (MoS₂) as direct bandgap semiconductor has gained a great deal of attention for novel discrete optoelectronic devices.¹⁻⁴ While a suspended monolayer MoS₂ flake shows photoluminescence (PL) efficiencies 100 times higher compared to a suspended bilayer flake,⁸ its overall quantum yield (QY) is still below 1% and excitonic emission is spectrally broad at room temperature. In contrast, when transferred on to substrates for device integration, QY for MoS₂ monolayers is even lower and only 3.5 times higher than that of a bilayer. Therefore, enhancement of its emission efficiency is necessary to realize the potential of atomically thin MoS₂ as a nanoscale active material in a light source. Modification of MoS₂ PL emission has been reported through addition of plasmonic nanoparticles,^{9,10} chemical dopants,¹¹ and photonic crystal cavities.^{12,13}

Recent developments in nano-optics have made possible the manipulation of light at sub-wavelength scales.¹⁴⁻¹⁷ For light sources such as lasers in particular, micrometer scale dielectric optical microcavities that support high Q WGM resonances have been extensively studied as potential candidates for providing optical feedback.^{14,18} These resonances arise as the light is confined via total internal reflection to a circular cavity. However, for efficient out of plane extraction of light the strong confinement of the cavity modes necessitates sophisticated evanescent coupling schemes requiring extremely precise placement of optical fibers or fabrication of waveguides next to the cavity.¹⁹ This is a significant obstacle for the practical implementation of these devices as narrow band light-sources integrated with emerging nanomaterials with efficient yet simple output coupling schemes.

For efficient integrated photonic light sources with MoS₂ active region, one needs to address: 1) High QY on substrates; 2) Efficient and simple input/output coupling to the devices with an atomically thin optical active region. To this end, in this work, we demonstrate the coupling of excitonic PL from chemically enhanced MoS₂ flakes to the high Q WGMs of a SiO₂ microdisk optical resonator with an engineered broadband notch input-output coupler for efficient optical excitation and light extraction. This unique combination enables a tunable narrowband light source with a high degree of temporal coherence due to the high Q WGM resonances and spatial coherence by localizing the out of plane emission near the sub-wavelength notch coupler. The light emitting material in this case is chemically enhanced bilayer MoS₂ that is embedded in the SiO₂ by the micromechanical exfoliation technique.²⁰ The SiO₂ cavity was designed to have WGM

resonances coinciding with the peak PL near 664 nm. A sub-wavelength ($\sim\lambda/2$) notch was introduced at the rim of the disk to significantly increase both in- and out-coupling efficiencies and simultaneously localizes emission. This notch enables the structure to function effectively as an optically pumped, spectrally narrowband light source with an active material that is only a few atoms thick.

3.2 Theoretical Analysis of Microdisk Design

Analytical approximations to the whispering gallery mode resonances in cylindrical geometries are well known¹⁻³. Here we re-summarize the essential aspects: in a microdisk geometry, due to the large vertical confinement in the z direction, the functional dependence of the wave equation on r , θ and z variables can be separated so that the electric field can be written:

$$E = E_r(r)e^{\pm im\theta}e^{\pm i\beta z}$$

where $E_r(r)$ is the solution to the radial part of the classical Helmholtz equation, $e^{\pm im\theta}$ gives the azimuthal angle dependence where m is the azimuthal number (broadly analogous to the number of total internal reflections undergone in the cavity before returning to its original position), and β is the propagation constant in the out of plane direction. Here we have suppressed the time dependent behavior of the fields. In the case of no propagation along the cylindrical axis $\beta=0$.

The radial part of the Helmholtz equation is

$$r^2 \frac{d^2 E_r}{dr^2} + r \frac{dE_r}{dr} + \left[r^2 \frac{\omega^2}{c^2} n_i^2 - m^2 \right] E_r = 0$$

where ω is the frequency and n_i is the (effective) index of the region in which the equation is solved for. This is a standard Bessel-form differential equation: with the usual constraints that solutions must tend to zero going to infinity but be finite at the origin, we have that

$$E_r = \begin{cases} J_m\left(r n_{disk} \frac{\omega}{c}\right), r \leq R \\ H_m^{(1)}\left(r \frac{\omega}{c}\right), r > R \end{cases}$$

i.e. solutions of the field inside the disk are Bessel functions, whereas external solutions are Hankel functions of the first kind⁴. The latter can also be approximated by a Bessel function multiplied by a decaying exponential¹ of the form $\exp(-\alpha(r - R))$, where $\alpha = \omega/c \sqrt{(n_{disk}^2 - 1^2)}$. Here we have assumed that the cladding or external environment has a uniform index of unity. Approximate resonance positions can be found by matching boundary conditions at $r = R$ and solving the resultant transcendental equations for ω , either numerically or for example via the Green's function method^{2,3}. Note that in this case the roots for ω will necessarily be complex; consequently the resonant frequencies can be written $\omega_{res} = \sqrt{\text{Re}(\omega)^2 + \text{Im}(\omega)^2}$ and the quality (Q) factor due to the radiative loss is $Q_{rad} = \text{Re}(\omega)/2\text{Im}(\omega)$.

In addition, from the expressions for E_r previously, several observations can be made: firstly, since solutions inside the disk are Bessel functions (standing wave along radial axis) whereas immediately outside the solutions are Hankel functions (travelling waves along radial axis), one immediately sees that these modes are leaky, i.e. the circulating

light cannot be entirely confined within the cavity. Secondly, the expression for the electric field, being a Bessel function implies that the localization of the mode increases sharply with m since $J_m\left(rn_{disk}\frac{\omega}{c}\right) \propto \left(rn_{disk}\frac{\omega}{c}\right)^m$ for $\left(rn_{disk}\frac{\omega}{c}\right) \ll 1$. So the general design principles for a microdisk cavity are that it should be sufficiently large to admit a high azimuthal mode number at the target frequency, with only one radial mode close to the edge, with an increasingly smaller mode volume as azimuthal mode number increases.

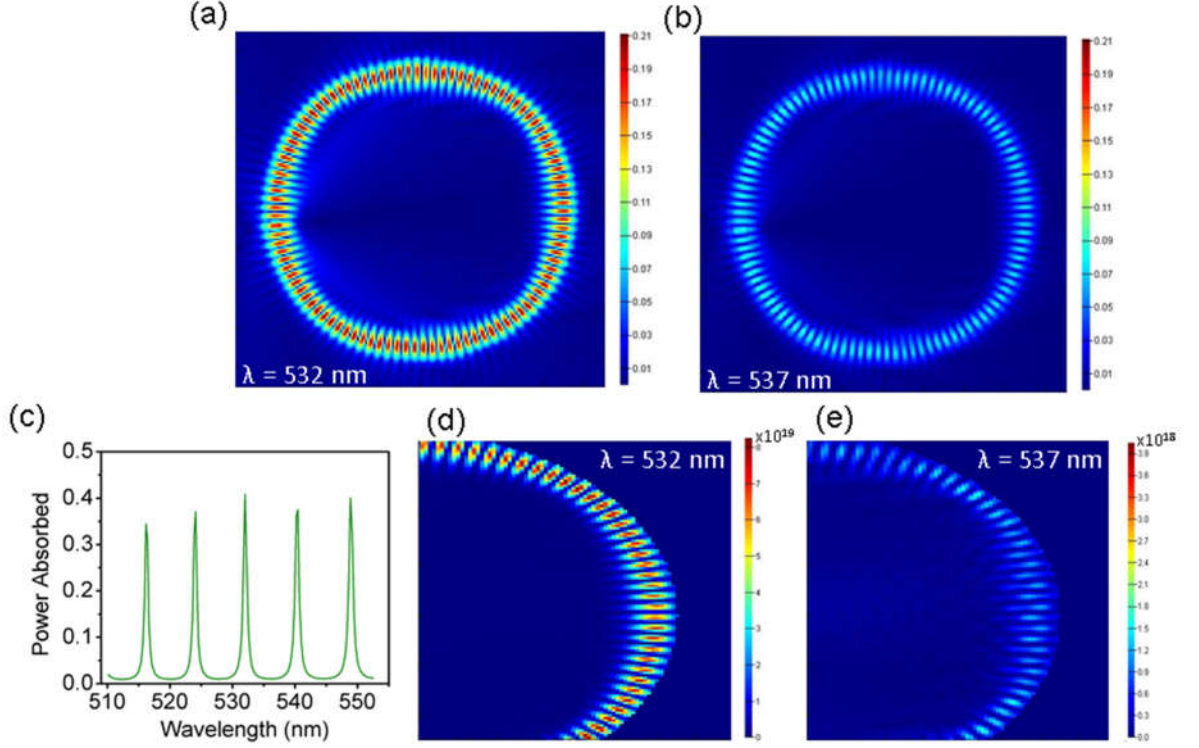


Figure 3.1 The $|E|$ for the microdisk (a) on-resonance at $\lambda = 532$ nm and (b) off-resonance at $\lambda = 537$ nm. The two colormaps are of the same scale. (c) A plot showing the spectral dependence of the excitation wavelength on the power absorbed by the MoS₂ flake coupled to the microdisk cavity. Plots of the power absorbed per unit volume of the MoS₂ flake for both the (d) on-resonant $\lambda = 532$ case as well as the (e) off-resonant $\lambda = 537$ case. The colormap scales for these two plots differ by a factor of ~ 20 .

3.3 Results and Discussion

Figure 3.2a-b show SEM images of a microfabricated notched microdisk light source with integrated MoS₂ layer. The orange shaded area in **Figure 3.2a** and the white dotted outline in **Figure 3.2b** show the device active region covered with the MoS₂ flake that was transferred from a bulk natural molybdenite crystal. These microdisks are fabricated from thermally grown SiO₂ released from the underlying Si substrate, with a central Si pedestal remaining for structural support. As mentioned previously, these microdisks are able to support high Q-factor WGMs. These resonances can be

characterized by the azimuthal mode number m , which determines the number of field maxima or minima around the microdisk circumference, and the radial mode number n corresponding to the number of radial nodes in the field.²¹⁻²³ For operation at a fixed wavelength, the Q-factor for a WGM resonance increases with increasing radius.²¹⁻²³ However, in the case of exfoliated 2-D materials due to the small areas available with transferred flakes, the microdisk cannot be excessively large to allow for considerable spatial overlap with the WGMs. Due to the proximity of the support pedestal to the edge of the microdisk cavity only the modes with $n = 1$ achieve high Q. A disk of radius 3.8 μm was chosen, as it provides reasonably high Q within the size limitation of the exfoliated MoS_2 flake. The microdisk height is constrained by the use of the 285 nm thermal oxide required for locating, through thin film interference, low optical contrast MoS_2 flakes on Si substrates.²⁴

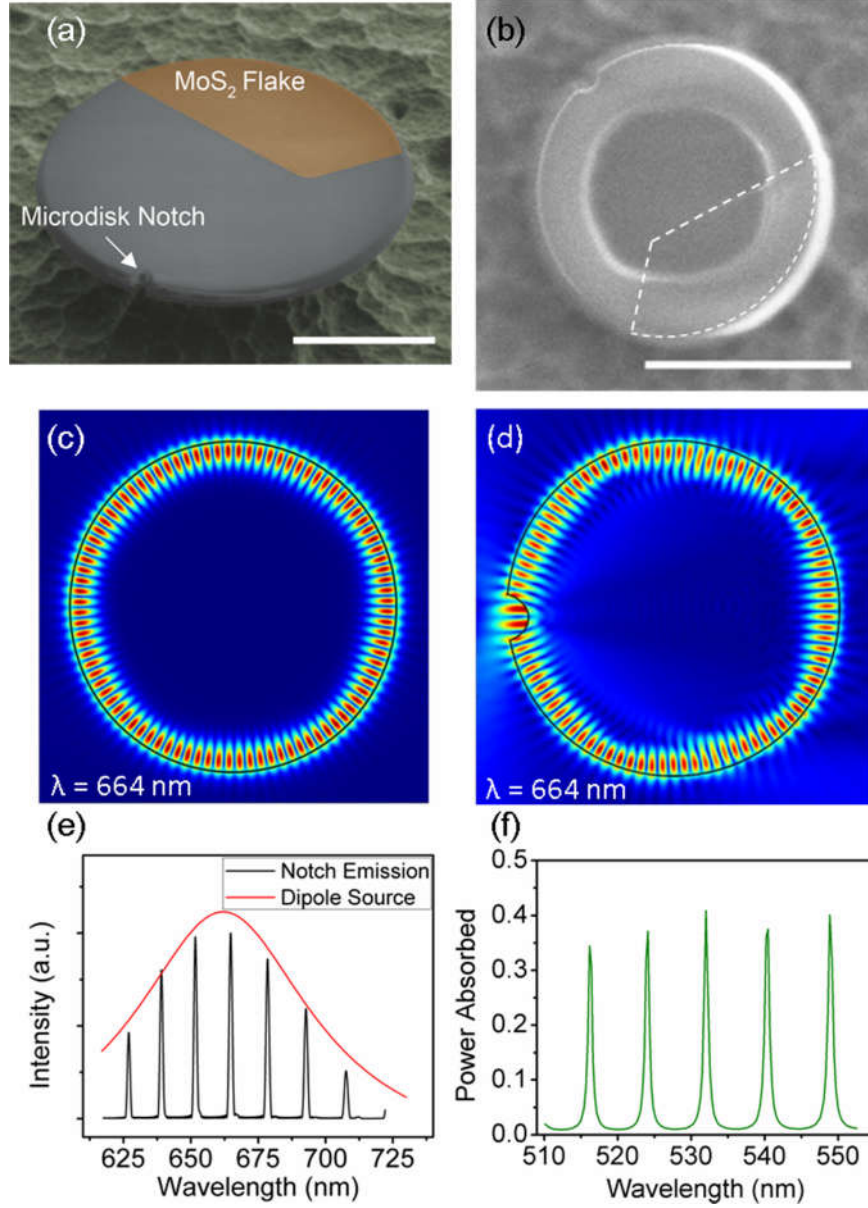


Figure 3.2 (a) SEM image of a MoS₂-coupled microdisk cavity showing a false-colored, tilted view and with low accelerating voltage. The shaded lighter, orange area denotes the area with the MoS₂ flake coverage on the microdisk. Scale bar is 2 μ m. (b) SEM image of the same microdisk with top-down view and with higher accelerating voltage, showing the free-standing portion of the microdisk supported by a silicon pillar. The white dotted area shows the location of the MoS₂. Scale bar is 5 μ m. Field intensity profiles at 664 nm (on resonance) for a (c) perfect 3.8 μ m radius disk as well as a (d) notched disk. (e) FDTD simulations showing dipole excitation at 664 nm and the resulting notch emission from the cavity. (f) A plot from FDTD simulations showing the spectral dependence of the excitation wavelength on the power absorbed by the MoS₂ flake coupled to the microdisk cavity.

Figure 3.2c shows the spatial distribution of the electric field intensity for the transverse-electric (TE), $n = 1$, $m = 46$ WGM of a perfectly circular microdisk. The mode shown is the PL from MoS₂ flake near the edges of the disk, which is expected to couple well to the WGMs due to the good spatial overlap with the mode. However, the WGM coupled light will not scatter efficiently out of the cavity in the out of plane direction. By incorporating a 200×300 nm semicircular notch, the light can be efficiently coupled in and out of the microdisk. Due to the sub-wavelength size of the notch, the Q is only minimally perturbed indicating that in-plane losses are dominated by leakage due to the small size of the cavity.²⁵ The modification to the WGMs from the notch can be seen in **Figure 3.2d**. Since the PL emission of MoS₂ originates entirely from excitonic transitions polarized in the plane of the material, we only consider the TE modes of the microdisk resonator.²⁶

We calculated the emitted optical power from the notch by modelling the MoS₂ PL with a Lorentzian (**Figure 3.2e**, red curve) dipole source. This is shown in **Figure 3.2e** along with the spectral response of the notched microdisk cavity. We observe that the system supports multiple TE _{$n=1,m$} modes (**Figure 3.2e**, black curve). As a result, the far field emission spectrum from the notch becomes almost entirely dominated by these WGMs whose relative intensities are modulated by the assumed Lorentzian spectrum.

To determine the cavity coupled absorption efficiency with the notch coupler, we assumed a Gaussian beam focused on the notch with a spectrum matching the experimental excitation wavelength of 532 nm. The coupler first scatters light efficiently into the plane of the silica microdisk to excite cavity modes. The optical power in these

resonant modes circulating in the microdisk is then absorbed by the MoS₂ layer. The interaction of the cavity modes with the active layer is strong due to high cavity Q and good spatial overlap of the MoS₂ flake with the $TE_{n=l,m}$ modes (**Figure 3.2a-b**). The absorption can reach up to 40% on-resonance, and have average power absorption of 6.22% between 528-537 nm.

The emission efficiency of MoS₂ flakes needs to be improved for the optically pumped microdisk coupled light source. For the microdisk light source, we have adopted an approach that offers improved PL through the use of successive cycling of ozone, water, and 3-aminopropyltriethoxysilane during the atomic layer deposition (ALD) of SiO₂. Using this ALD process, we can chemically enhance the light emission from a bilayer (2L) flake of MoS₂ (**Figure 3.3b**). This can be seen by systematically performing PL and Raman microscopies on a 2L flake. We define ‘E-2L’ as an exfoliated bilayer MoS₂ flake that has undergone the process of ALD etching, chemical enhancement and encapsulation by SiO₂. Similarly, we denote as-exfoliated monolayer MoS₂ as ‘1L’. **Figure 3.3a** shows the separation of the E_{2g}¹ and the A_{1g} Raman active vibrational modes for 1L, 2L, and E-2L MoS₂ samples. For 2L and 1L MoS₂, the Raman peak separation values are around 22.3 and 19.5 cm⁻¹, respectively, which match closely to other reported values for the separation at these layer thicknesses.²⁷ After exposure to the ALD process, the peak separation of an E-2L flake gradually decreases from 22.3 cm⁻¹ to 20.3 cm⁻¹ (**Figure 3.3a**). This implies that as more SiO₂ is deposited through the ALD process, more and more of the top monolayer of material is etched. The disappearance of initially 1L flakes further indicates the etching process.

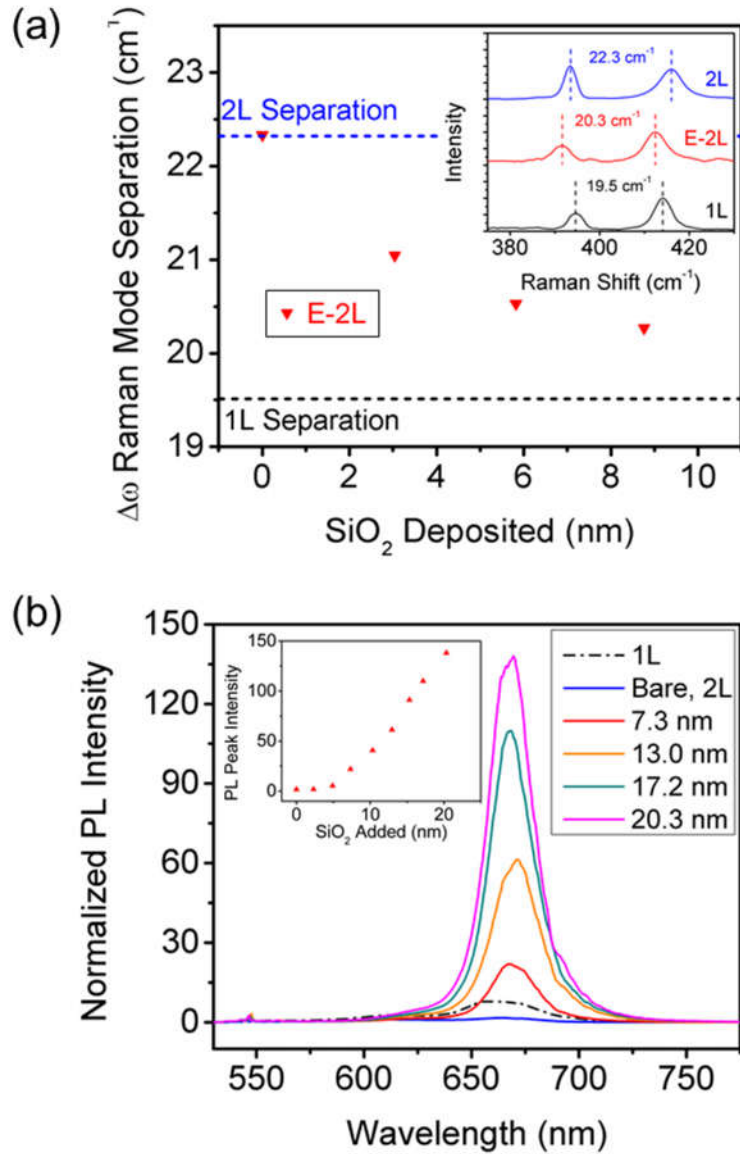


Figure 3.3 (a) Raman spectroscopy of the MoS₂ E_{2g}^1 and A_{1g} vibrational modes and their separation for monolayer (1L), bilayer (2L). The data plotted in red shows the change in Raman mode separation for enhanced bilayer (E-2L) as a function of added ALD SiO₂. The initially bilayer flake shows a narrowing of the mode separation which approaches the monolayer limit. The inset shows the Raman spectra and mode separation for 2L, 1L as well as E-2L MoS₂. (b) MoS₂ Raman-normalized PL for the E-2L MoS₂ with increasing amounts of ALD SiO₂ added. Here, bare represents data for as-exfoliated bilayer, 2L MoS₂. The data given by the dotted line is the PL for as-exfoliated monolayer 1L MoS₂ as a comparison. The inset shows the Raman-normalized peak intensities as a function of added SiO₂, reaching levels ~2 orders of magnitude larger than the initial values

Additionally, with increasing ALD cycles, the weak 2L MoS₂ PL transitions to a more luminescent monolayer-type emission after addition of SiO₂ (**Figure 3.3b**). As an internal calibration, the spectra are normalized to the MoS₂ Raman peak intensities. For a deposited SiO₂ thickness of ~20 nm, PL intensity dramatically increases 70-fold corresponding to 20 times the brightness of the as-exfoliated monolayer MoS₂. We attribute this chemically enhanced PL to partial etching of the original bilayer MoS₂ yielding a mostly monolayer flake of higher quality than the as-transferred monolayer. In addition to the etching involved in the ALD process, the ozone based chemistry used in the oxide deposition also might change the effective doping in the resulting monolayer, which further increases the luminescence.²⁸ The thin SiO₂ layer also serves as an encapsulation for the resulting MoS₂ layer from further reactive etching processes needed for patterning of the microdisks that would detrimentally affect optical properties.

These E-2L MoS₂ flakes were then incorporated into SiO₂ microdisk optical resonators with the notch coupler. In **Figure 3.4a**, by probing the notch with a 532 nm laser, we see discrete emission peaks corresponding to the WGMs, which are modulated by the original MoS₂ PL intensity. Only certain wavelengths within the MoS₂ emission spectrum are coupled back into the microdisk cavity selected by the allowed cavity modes. It is these modes that are then scattered at the notch. These modes have Q factors as high as 900 (**Figure 3.4b**), which is in agreement with values in the literature for small optical microcavities in the visible.²⁹ The free spectral range (FSR) of ~9.5 THz is also consistent across different samples (**Figure 3.5**), showing the sample uniformity.

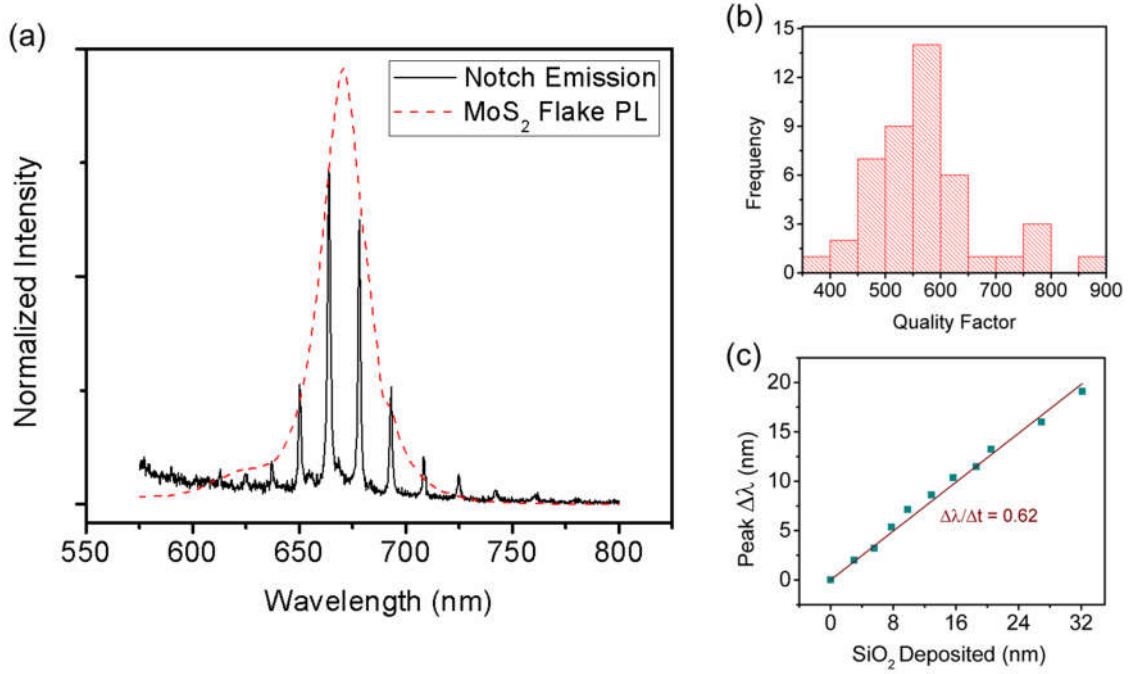


Figure 3.4 (a) Confocal microscope spectroscopy of different areas of the coupled microdisk resonator; flake PL when illuminating and probing the MoS₂ flake (red curve), and notch emission when probing and illuminating the notch in the microdisk (black curve). (b) Histogram showing the quality factor of the modes and their frequency of occurrence across the samples used in this study. (c) Plot of the shift in notch emission peaks with the addition of SiO₂ to fully fabricated MoS₂ coupled microdisks, with a redshift in the spectra of 0.62 nm for each nanometer of SiO₂ added.

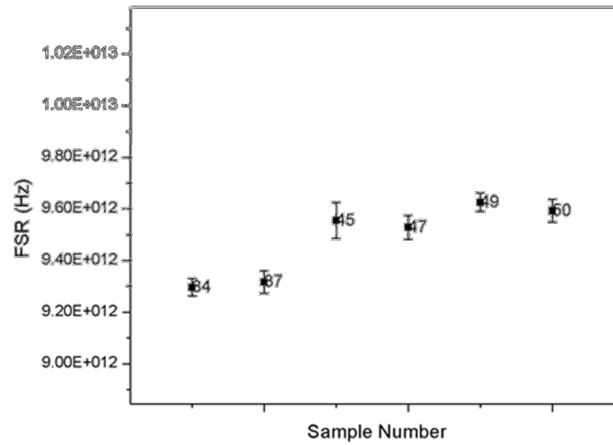


Figure 3.5 Plot of the free spectral range (FSR) for the different samples used in this study. The error bars represent one standard deviation for modes of the corresponding sample. The small variation across the samples shows relative consistency of the fabrication process.

It is also possible to tune the resonances by post processing. By slightly altering the dimensions of the microdisk, we can tune the cavity modes by more than the full FSR of the microcavity. To do this, we increased the disk height by sequentially adding SiO₂. **Figure 3.4c** shows the tuning of the peaks as thin layers of SiO₂ are added to an existing MoS₂ coupled microdisk through ALD. The peak wavelengths shift linearly with a 0.62 nm shift in the emission peak position per nanometer of added SiO₂ consistent with the theoretical trend (**Figure 3.6**).

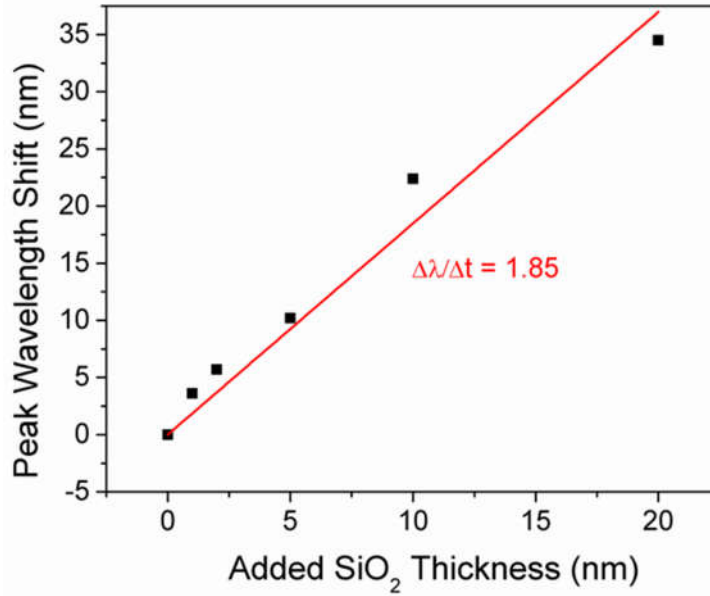


Figure 3.6 This plot shows the FDTD simulation results for the change in the cavity-coupled MoS₂ PL peak as a function of added SiO₂ to the top of the microdisk structure.

As shown in **Figure 3.7a**, high Q peaks with a linewidth of 2.44 meV can be achieved, which in turn means that the emitted light has a high degree of temporal coherence (coherence length of approximately 440 μm, in contrast to typical LED coherence lengths on the order of tens of μm³⁰). In addition, the notched microdisk

geometry allows for a high degree of spatial coherence as well. **Figure 3.7c-d** show FDTD simulations of the electric field intensity profile at the surface of the microdisk as well as 1 μm above the surface of the disk, where the only significant radiation into the far field comes from the locality of the notched area. The spatial coherence of the emitted light can be seen in the cross sectional intensity plot of the electric field 1 μm above the surface of the disk in **Figure 3.7b**. The intensity of the beam spot fits nicely to the Gaussian form with a width of 884 nm (corresponding approximately to a divergence angle of 23.8°) and a coherence area of approximately $1.55 \mu\text{m}^2$. This is larger than the observed beam spot size, which is approximately $0.805 \mu\text{m}^2$ by treating it as an ellipse with major and minor axes of 1160 nm and 884 nm respectively. Although we observe high spatial and temporal coherence, we do not observe lasing in this system and any non-linear pump intensity dependence is attributed to thermal effects.

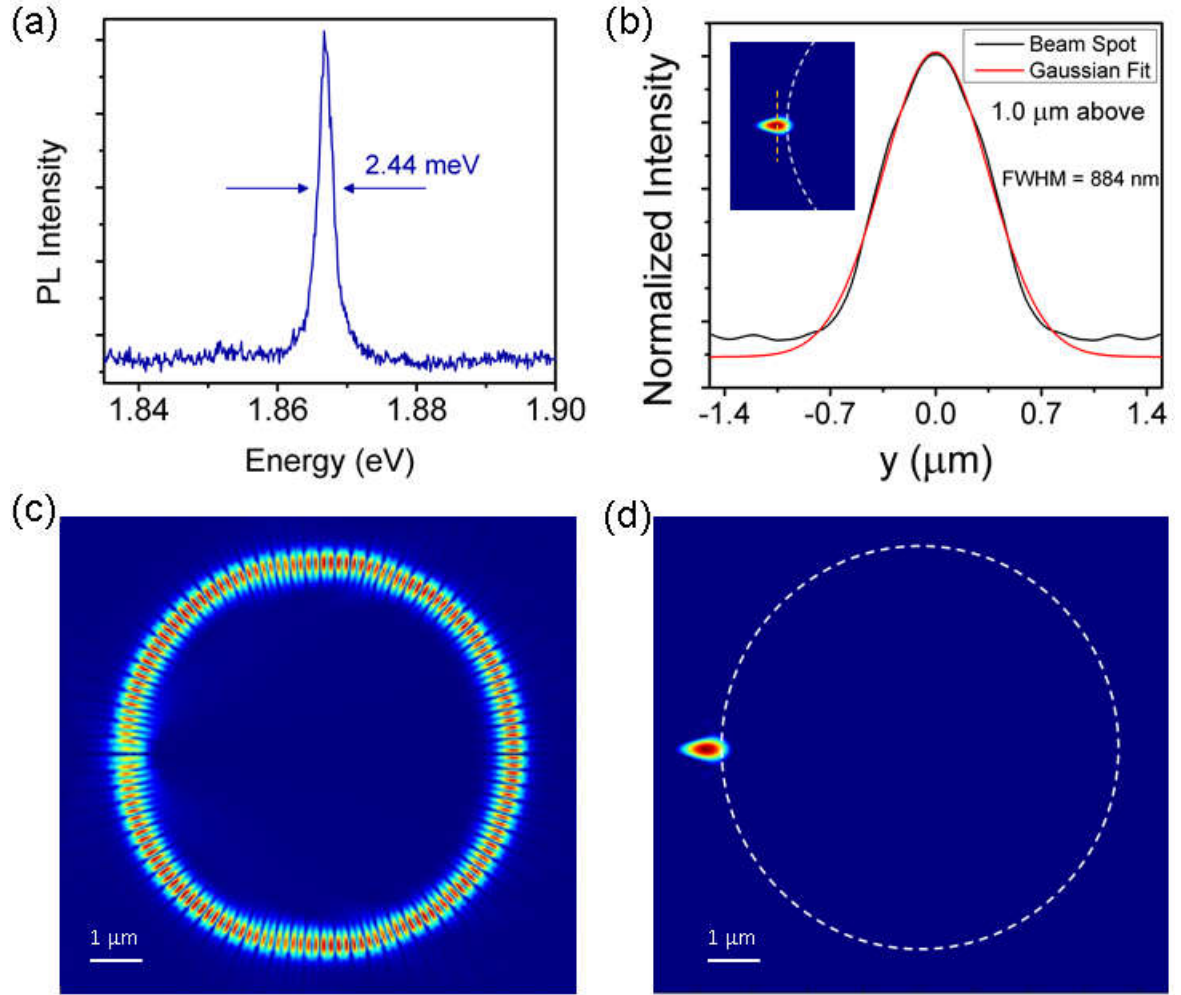


Figure 3.7 (a) Plot of the PL coupled to a cavity mode showing a FWHM of 2.44 meV corresponding to a coherence length of 440 μm (b) Calculated electric field intensity profile near the notch 1.0 μm above the surface of the disk which matches well with a Gaussian fit. The inset shows a dotted orange line which shows the line scan direction relative to the disk from (d). Calculated electric field intensity at (c) the surface of the disk and (d) 1.0 μm above the disk showing that the far-field radiated optical power originates from the notch. Spatial coherence is determined by the dimension of the notch.

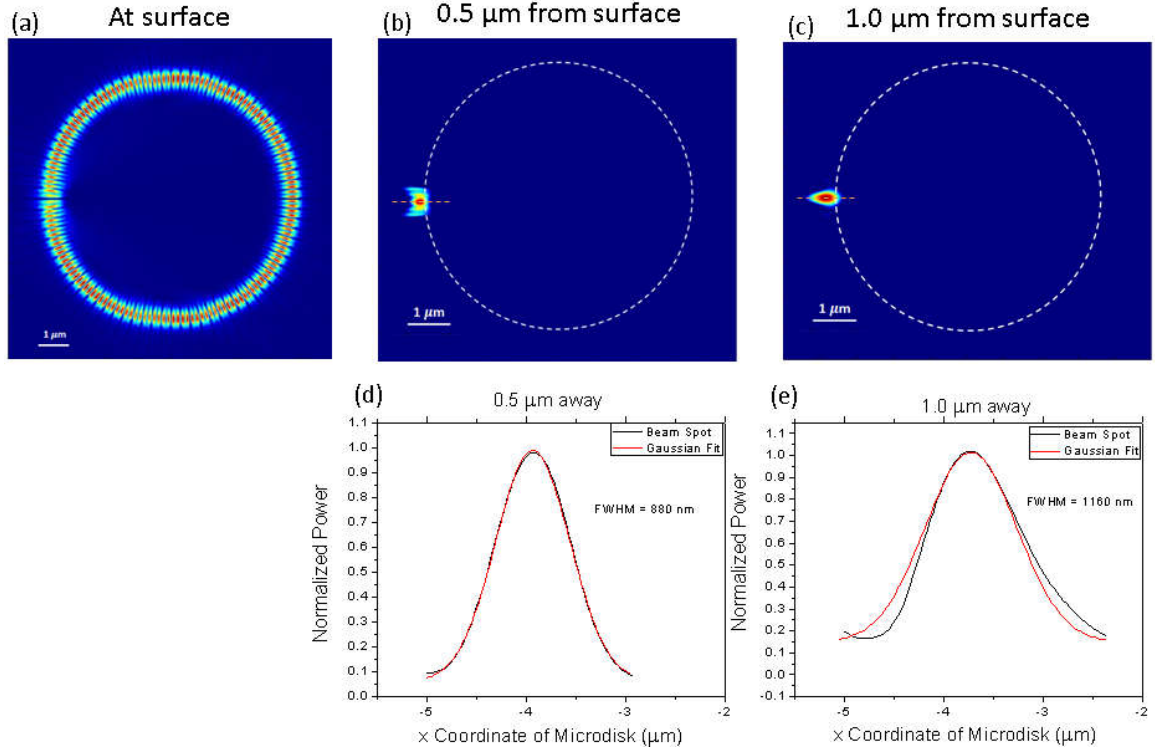


Figure 3.8 FDTD simulations of the electric field intensity and PL spot width from a Gaussian source. 2-D FDTD plots of the electric field distribution at (a) the surface of the microdisk, (b) 0.5 μm above and (c) 1.0 μm above the surface. Plots of the horizontal cross section of the spot width at (d) 0.5 μm and (e) 1.0 μm from the surface (orange dotted line on (b) and (c), respectively).

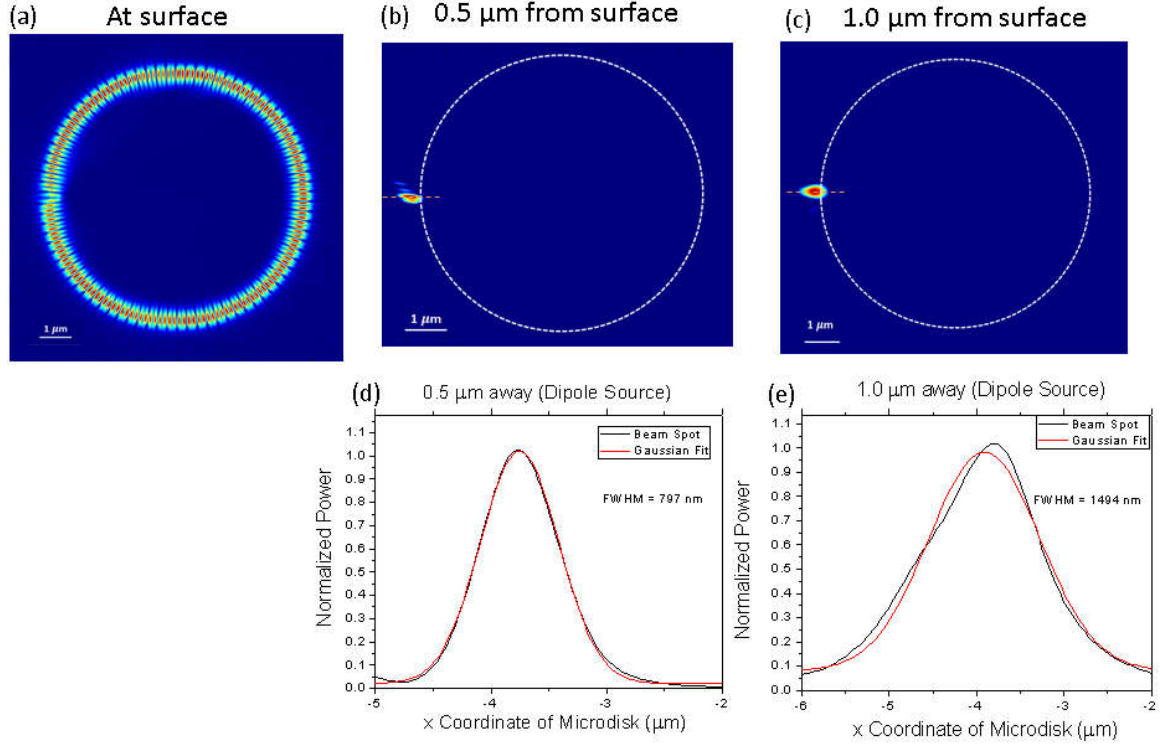


Figure 3.9 FDTD simulations of the electric field intensity and PL spot width from a Dipole source. 2-D FDTD plots of the electric field distribution at (a) the surface of the microdisk, (b) 0.5 μm above and (c) 1.0 μm above the surface. Plots of the horizontal cross section of the spot width at (d) 0.5 μm and (e) 1.0 μm from the surface (orange dotted line on (b) and (c), respectively). These plots are analogous to those of Supp. Fig. 3, with the difference in the excitation source.

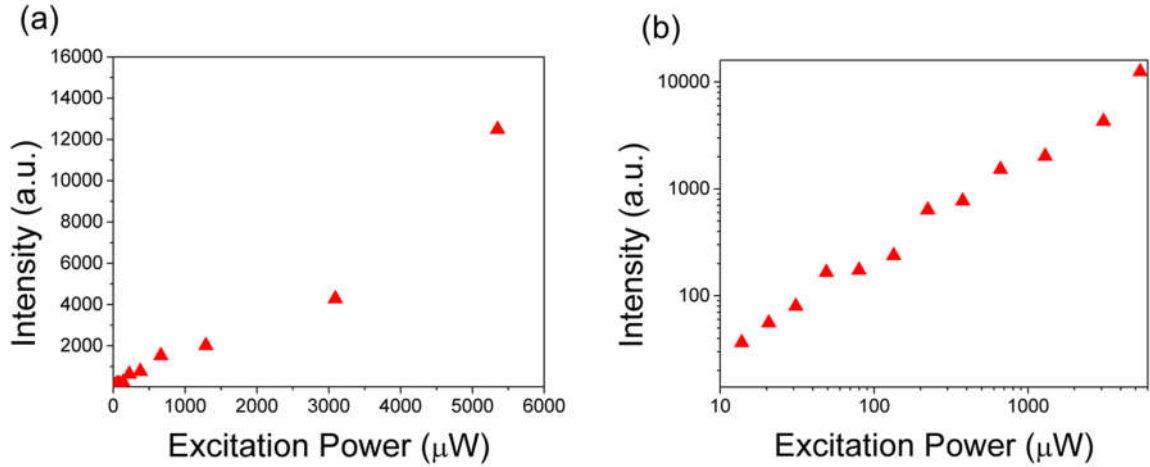


Figure 3.10 Graphs of the intensity of the WGM peaks at different excitation powers shown in (a) linear and (b) logarithmic scales. At these power levels, there is no indication of lasing action in this system.

3.4 Conclusions

In summary, we both experimentally and theoretically show that a two-dimensional material, MoS₂, can be chemically enhanced and used to make a tunable light source with high spatial and temporal coherence when integrated with a notched microdisk optical cavity. Very high contrast emission in comparison to the MoS₂ PL can be seen at very low pump power densities. The success of recent efforts at synthesizing high quality, large scale MoS₂ by chemical vapor deposition (CVD) is extremely promising^{31,32} and will allow for device fabrication at a larger scale. Additionally, this platform can be utilized for other types of 2-D TMDC materials, giving us the ability to utilize and probe the optical properties of this emerging class of materials. This work will ultimately pave the way toward lasers with atomically thin gain media and has a great promise for the basis for lab-on-a-chip type sensing applications.³³

3.5 References

- 1 Pospischil, A., Furchi, M. M. & Mueller, T. "Solar-Energy Conversion and Light Emission in an Atomic Monolayer P-N Diode". *Nat Nano* **9**, 257 (2014).
- 2 Baugher, B. W. H., Churchill, H. O. H., Yang, Y. & Jarillo-Herrero, P. "Optoelectronic Devices Based on Electrically Tunable P-N Diodes in a Monolayer Dichalcogenide". *Nat Nano* **9**, 262 (2014).
- 3 Jones, A. M. *et al.* "Optical Generation of Excitonic Valley Coherence in Monolayer Wse₂". *Nat Nano* **8**, 634 (2013).
- 4 Yin, Z. *et al.* "Single-Layer Mos₂ Phototransistors". *ACS Nano* **6**, 74 (2011).
- 5 Huffaker, D. L., Park, G., Zou, Z., Shchekin, O. B. & Deppe, D. G. "1.3 Mm Room-Temperature Gaas-Based Quantum-Dot Laser". *Applied Physics Letters* **73**, 2564 (1998).
- 6 Wood, T. H. *et al.* "High-Speed Optical Modulation with Gaas/Gaalas Quantum Wells in a P-I-N Diode Structure". *Applied Physics Letters* **44**, 16 (1984).
- 7 Pan, D., Towe, E. & Kennerly, S. "Normal-Incidence Intersubband (in, Ga)as/Gaas Quantum Dot Infrared Photodetectors". *Applied Physics Letters* **73**, 1937 (1998).
- 8 Mak, K. F., Lee, C., Hone, J., Shan, J. & Heinz, T. F. "Atomically Thin Mos₂: A New Direct-Gap Semiconductor". *Physical Review Letters* **105**, 136805 (2010).
- 9 Sobhani, A. *et al.* "Enhancing the Photocurrent and Photoluminescence of Single Crystal Monolayer Mos₂ with Resonant Plasmonic Nanoshells". *Applied Physics Letters* **104**, 031112 (2014).
- 10 Kang, Y. *et al.* "Plasmonic Hot Electron Induced Structural Phase Transition in a Mos₂ Monolayer". *Advanced Materials* **26**, 6467 (2014).
- 11 Mouri, S., Miyauchi, Y. & Matsuda, K. "Tunable Photoluminescence of Monolayer Mos₂ Via Chemical Doping". *Nano Letters* **13**, 5944 (2013).
- 12 Gan, X. *et al.* "Controlling the Spontaneous Emission Rate of Monolayer Mos₂ in a Photonic Crystal Nanocavity". *Applied Physics Letters* **103**, 181119 (2013).
- 13 Sanfeng, W. *et al.* "Control of Two-Dimensional Excitonic Light Emission Via Photonic Crystal". *2D Materials* **1**, 011001 (2014).
- 14 Srinivasan, K., Borselli, M., Painter, O., Stintz, A. & Krishna, S. "Cavity Q, Mode Volume, and Lasing Threshold in Small Diameter Algaas Microdisks with Embedded Quantum Dots". *Optics Express* **14**, 1094 (2006).
- 15 Cao, H. *et al.* "Optically Pumped Inas Quantum Dot Microdisk Lasers". *Applied Physics Letters* **76**, 3519 (2000).
- 16 Liu, Z., Lee, H., Xiong, Y., Sun, C. & Zhang, X. "Far-Field Optical Hyperlens Magnifying Sub-Diffraction-Limited Objects". *Science* **315**, 1686 (2007).
- 17 Taubner, T., Korobkin, D., Urzhumov, Y., Shvets, G. & Hillenbrand, R. "Near-Field Microscopy through a Sic Superlens". *Science* **313**, 1595 (2006).
- 18 Wang, Q. J. *et al.* "Whispering-Gallery Mode Resonators for Highly Unidirectional Laser Action". *Proceedings of the National Academy of Sciences* **107**, 22407 (2010).
- 19 Hossein-Zadeh, M. & Vahala, K. J. "Free Ultra-High-Q Microtoroid: A Tool for Designing Photonic Devices". *Optics Express* **15**, 166 (2007).

- 20 Novoselov, K. S. *et al.* "Electric Field Effect in Atomically Thin Carbon Films". *Science* **306**, 666 (2004).
- 21 Borselli, M., Johnson, T. & Painter, O. "Beyond the Rayleigh Scattering Limit in High-Q Silicon Microdisks: Theory and Experiment". *Optics Express* **13**, 1515 (2005).
- 22 Quan, H. & Guo, Z. "Analyses of Whispering-Gallery Modes in Small Resonators". *MOEMS* **8**, 033060 (2009).
- 23 Dettmann, C. P., Morozov, G. V., Sieber, M. & Waalkens, H. "Internal and External Resonances of Dielectric Disks". *EPL (Europhysics Letters)* **87**, 34003 (2009).
- 24 Castellanos-Gomez, A., Agraït, N. & Rubio-Bollinger, G. "Optical Identification of Atomically Thin Dichalcogenide Crystals". *Applied Physics Letters* **96**, 213116 (2010).
- 25 Boriskina, S. V., Benson, T. M., Sewell, P. & Nosich, A. I. "Q Factor and Emission Pattern Control of the Wg Modes in Notched Microdisk Resonators". *Selected Topics in Quantum Electronics, IEEE Journal of* **12**, 52 (2006).
- 26 Schuller, J. A. *et al.* "Orientation of Luminescent Excitons in Layered Nanomaterials". *Nat Nano* **8**, 271 (2013).
- 27 Lee, C. *et al.* "Anomalous Lattice Vibrations of Single- and Few-Layer Mos2". *ACS Nano* **4**, 2695 (2010).
- 28 Chang, J., Larentis, S., Tutuc, E., Register, L. F. & Banerjee, S. K. "Atomistic Simulation of the Electronic States of Adatoms in Monolayer Mos2". *Applied Physics Letters* **104**, 141603 (2014).
- 29 Min, B. *et al.* "High-Q Surface-Plasmon-Polariton Whispering-Gallery Microcavity". *Nature* **457**, 455 (2009).
- 30 Coutinho, R. C. *et al.* "Variable Numerical-Aperture Temporal-Coherence Measurement of Resonant-Cavity Leds". *J. Lightwave Technol.* **21**, 149 (2003).
- 31 Zhan, Y., Liu, Z., Najmaei, S., Ajayan, P. M. & Lou, J. "Large-Area Vapor-Phase Growth and Characterization of Mos2 Atomic Layers on a Sio2 Substrate". *Small* **8**, 966 (2012).
- 32 Lee, Y.-H. *et al.* "Synthesis of Large-Area Mos2 Atomic Layers with Chemical Vapor Deposition". *Advanced Materials* **24**, 2320 (2012).
- 33 Luchansky, M. S. & Bailey, R. C. "High-Q Optical Sensors for Chemical and Biological Analysis". *Analytical Chemistry* **84**, 793 (2011).

CHAPTER 4: Cavity-Coupled 2-Dimensional Semiconductors: A Photothermal Analysis

4.1 Introduction

Transition metal dichalcogenides (TMDCs) have garnered intense research interest in the past few years. The TMDCs are semiconductor materials with a bulk indirect bandgap electronic structure. Much like graphene, the interest for this class of material comes from the ability to fabricate or synthesize single molecular layers. At the monolayer limit, the TMDCs transition to a direct bandgap material with broken inversion symmetry, leading to a range of interesting optical phenomena such as photoluminescence (PL),¹⁻⁴ optical nonlinearity,^{5,6} and valley polarization.^{7,8} However, these optical phenomena, while substantial for a monolayer of material, are still relatively weak and need to be improved upon to compete with incumbent technologies. Recently, there has been research into using optical structures to enhance or otherwise manipulate the optical effects of these TMDCs through use of plasmonic nanoparticles.⁹⁻¹¹

Optical cavities, in particular, are of considerable interest for incorporation of TMDCs. Any two-level emitter coupled to optical cavities can experience high Purcell enhancement factors stemming from high quality (Q) factor cavity modes.¹² This stems from the fact that the spontaneous rate of emission is proportional to the density of modes at the emission wavelength per volume of the cavity. Incorporation of TMDCs and their excitonic transitions into high-Q optical cavities is interesting for photoluminescence enhancement and modification because of this effect. Recently, materials such as MoS₂, WSe₂, and WS₂ have been incorporated into Fabry-Perot, whispering gallery microdisk, and photonic crystal optical microcavities.¹³⁻¹⁹

In this work, we study the thermal effects of coupled TMDC optical cavity systems. Specifically, we observe these effects in MoS₂ and WSe₂ within the context of a microdisk optical cavity geometry. Because high-Q optical cavities require large refractive index changes at their interfaces, many are physically isolated to be completely surrounded by the low index environment of air. This presents an issue of heating of the optical cavity caused by absorption of the emitting material and subsequent high rate of non-radiative recombination of the absorbed photons. We show that not only can this photothermal effect change the background PL of the emitting material leading to non-linearity in intensity vs pump power curves, that at high enough power and thermal isolation of the optical structure can lead to damage of the emitting material.

4.2 Results and Discussion

To make the MoS₂-coupled optical microdisk cavity, we first mechanically exfoliated molybdenite onto silicon dioxide on silicon substrates. After optical identification of the few layer MoS₂ flakes, we protect the flakes by addition of a thin layer of SiO₂ through atomic layer deposition. Using electron beam lithography, the shape of the microdisk was patterned and then etched into the SiO₂ substrate. A subsequent undercutting Si etch step was performed to release the edges of the microdisk to form the microdisk structures. **Figure 4.1a-b** show SEM images of the fabricated microdisks. The dimensions of the cylindrical microdisk are 3.8 μm in radius and 285 nm in height. These dimensions were chosen to support high-quality whispering gallery cavity modes in the microdisk while taking into account physical restraints in terms of the substrate oxide thickness and MoS₂ flake size. Additionally, a semicircular notch defect was incorporated into the microdisk

design which helps with input coupling of excitation light and output coupling of the cavity emission. The notch was also positioned on the opposite side of the microdisk as the MoS₂ flake area (colored purple) to separate the cavity-coupled emission from the direct flake emission. We have previously reported on the details on the microcavity design and optical characterization.¹⁴

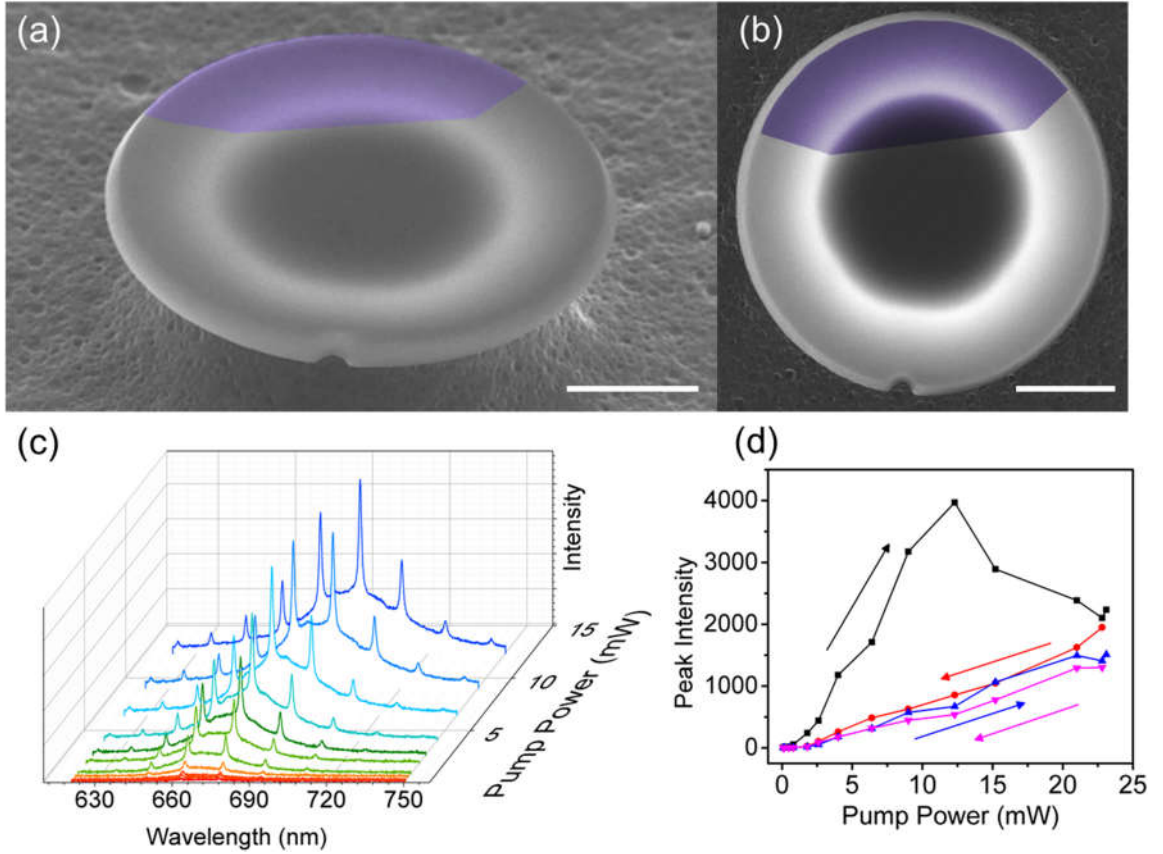


Figure 4.1 (a-b) SEM images of a silicon dioxide microdisk at a tilted and top-down view, respectively. The false-colored purple areas denote the location of the MoS₂. Scale bars are 2 μm . (c) Cavity-coupled emission spectra collected at the microcavity notch as a function of excitation laser power. (d) Peak intensity of the 685 nm cavity mode as the excitation power is cycled to and from 22.8 mW in two consecutive cycles (in order: black squares, red circles, blue upward triangles and purple downward triangles).

Using a continuous-wave (CW) $\lambda = 532$ nm laser illumination we observed spectrally sharp cavity modes collected at the microcavity notch on top of the background MoS₂ PL. **Figure 4.1c** shows the observed emission spectrum at various levels of illumination intensity. Figure 1d (black curve) tracks the intensity of the 685 nm cavity mode peak as the MoS₂ flake is illuminated with increasing pump power. We observe a non-linear increase in the peak intensity up to 12.3 mW of illumination. Above this threshold, the intensity of the cavity-coupled emission peaks start to decrease. Subsequent cycling of the illumination power on the microdisk (**Figure 4.1d**; red, blue and purple curves, respectively) yields a permanently lowered response. This decrease in the intensity is a clear signal of damage to the emitting material.

Figure 4.2a shows the spectra at three different power levels: low power: 0.03 mW, damage threshold: 12.3 mW, and well beyond the damage threshold: 22.8 mW. By distilling and normalizing the background MoS₂ PL at these power levels, as seen in **Figure 4.2b**, we make two observations. First, there is a noticeable red-shift of the PL spectra from 670 nm to 690 nm between the low power and damage threshold illumination levels. Second, after the damage threshold illumination, the red-shift of the PL spectra desists. The first observation suggests that there is a photothermal effect; as more light is input into the microcavity and absorbed by the MoS₂, non-radiative recombination processes in the TMDC produce heat.^{20,21} **Figure 4.2c** shows the PL peak wavelength for a MoS₂ flake on an un-patterned substrate as the entire substrate is heated to elevated temperatures. From these data, as well as the spectra shown in **Figure 4.2d**, we can see that there is a clear and reversible redshift in the PL spectra in MoS₂ with

increasing temperature. This data matches well with other reports on temperature-based MoS₂ PL spectra and may be a result of energetic changes in the band structure as a result of thermal expansion of the in-plane lattice.^{22,23} Thus, we can confidently describe the shift in the background PL of the MoS₂ in this first observation as a result of the photothermal effect.

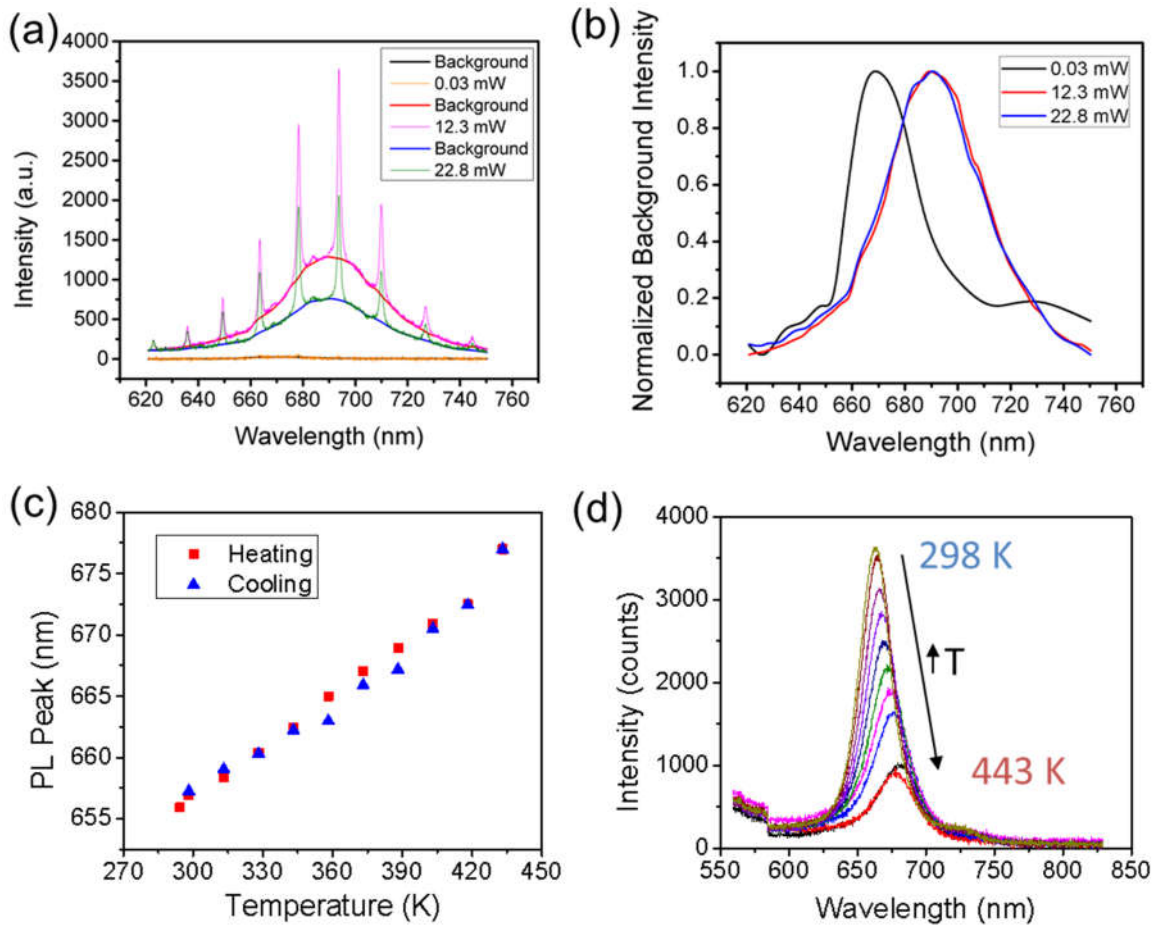


Figure 4.2 (a) Emission spectra at low power (0.03 mW), at the damage threshold (12.3 mW) and high power beyond the damage threshold (22.8 mW) and the corresponding background PL overlaid. (b) Normalized background PL from panel (a) at the three different power levels. (c) The position of the PL peak wavelength of MoS₂ during heating to and cooling down from elevated temperatures. (d) The evolution of the PL spectra of MoS₂ at different temperatures. Intensity decreases and peak position red shifts with increasing temperature.

The second observation, that above the damage threshold the photothermal effect stops, suggests that above the threshold thermal oxidation of the MoS₂ begins to occur. Oxidation of bulk MoS₂ has been reported to begin to occur above 500 K.²⁴ Extrapolating from the data gathered on the PL position with respect to temperature (**Figure 4.2c**), we can determine the temperature of the MoS₂ flake that relates to the shift in the PL background. Temperature can be tracked from the low power to the damage threshold level and above. A 20 nm redshift from 670 to 690 nm in the background PL peak corresponds to a temperature of around 550 K at and above the damage threshold. This is clearly in the range of material oxidation, and any further increase in the absorbed laser intensity will only serve to oxidize more of the emitting material. The reason no further red-shifting (and thus material heating) is observed beyond the damage threshold level is that as the MoS₂ is oxidized, light absorption also wanes. However, since light distribution in this whispering gallery mode cavity is not uniform,¹⁴ anti-nodal points with the highest electric field intensity will absorb and subsequently oxidize first.

This photothermal effect is not limited to MoS₂ and should be present in all of the 2-D TMDC materials. We further investigate the thermal effects on the PL properties of WSe₂. **Figure 4.3a** shows an optical image of a mechanically exfoliated WSe₂ flake with **Figure 4.3b-c** showing the Raman and PL spectra, respectively, which matches closely to previously reported spectra for monolayer WSe₂.³ We then looked at the evolution of the PL of WSe₂ as a function of temperature. **Figure 4.3d** tracks the peak of the photoluminescence spectra as the material is heated from room temperature to 172 °C. Upon heating the material, there is a redshift of ~40 nm. This is a similar and even larger

shift seen over a similar temperature range as in the case of MoS₂. Furthermore, upon cooling of the material, we observe a consistent and permanent change to the PL of the WSe₂. We attribute this to partial thermal oxidation of the WSe₂ at these elevated temperatures. The formation of the tungsten oxide decreases the overall intensity of the PL produced (as seen in **Figure 4.4**) by reducing the amount of luminescent material. Additionally, the oxide formation alters the electronic structure of the remaining luminescent WSe₂, leading to the permanent redshift in the PL spectra upon cooling of the material. This suggests that since oxidation and permanent change to the PL spectra of WSe₂ occurs at a lower temperature than that of MoS₂, the photothermal effect will have a larger influence and that the damage threshold will be lower. In general, similar thermal trends of the PL spectra have been observed in other materials such as MoSe₂,²² and WS₂.²⁵

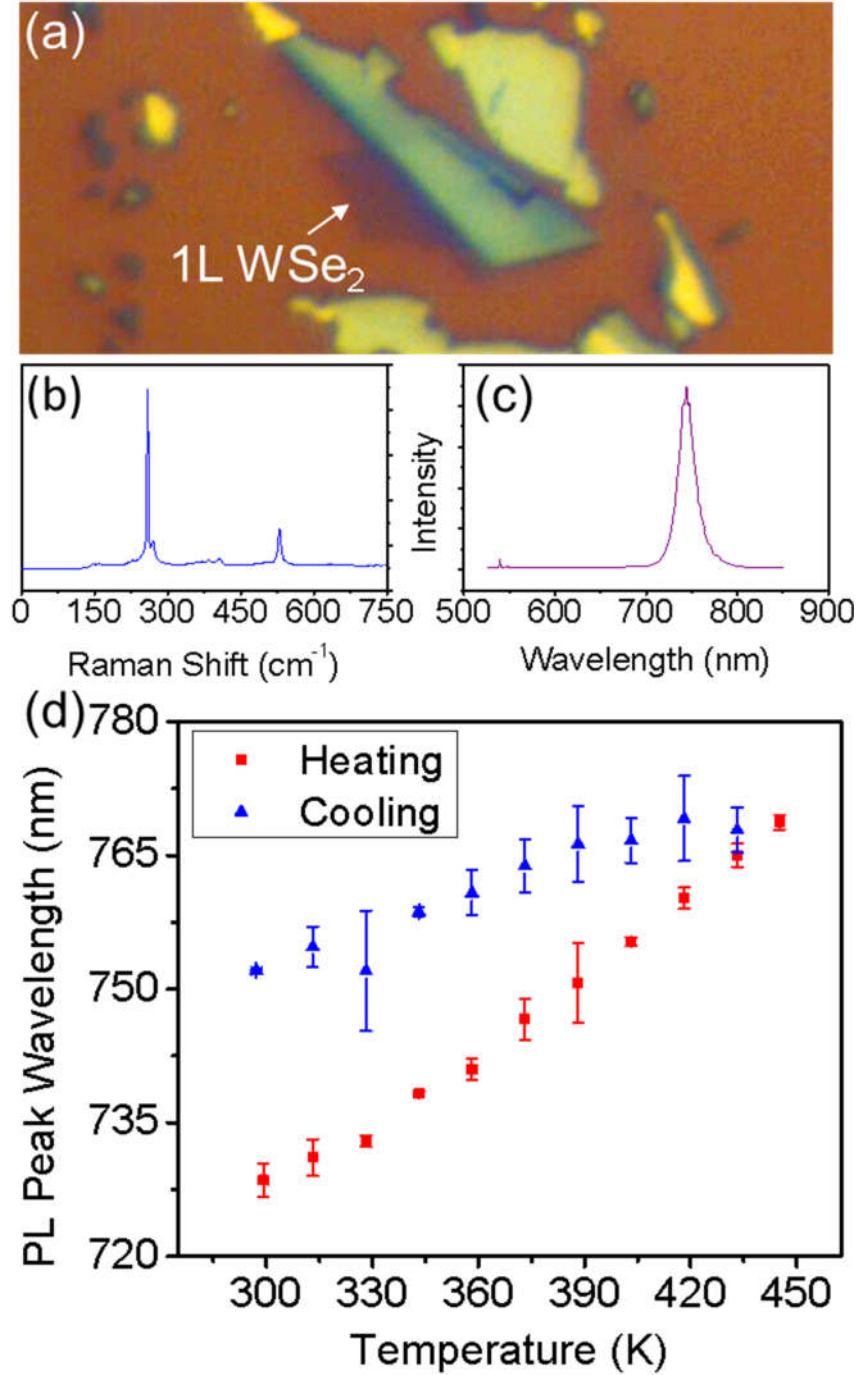


Figure 4.3 (a) Optical image of a monolayer (1L) WSe₂ flake. (b) Raman and (c) photoluminescence spectra that are characteristic of monolayer WSe₂. (d) The position of the PL peak wavelength of WSe₂ during heating to and cooling down from elevated temperatures. The data is averaged over multiple samples and error bars show standard deviation from the mean, showing reproducibility of the irreversible red shift.

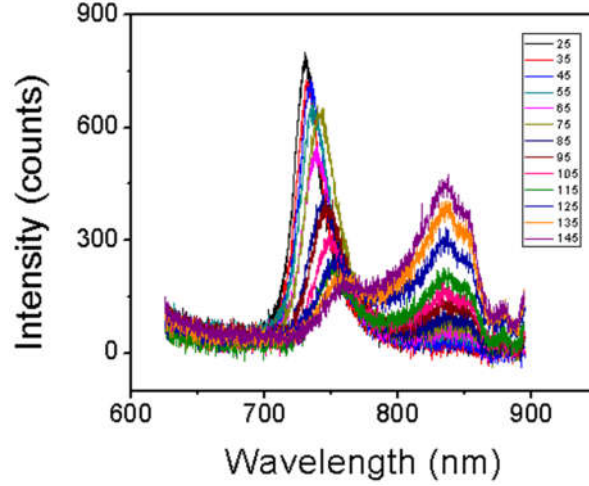


Figure 4.4 Graph of the PL spectrum for WSe₂ at increasing temperatures up to 145° C showing a decrease in the overall intensity and red-shift of the main PL peak.

The design considerations of the optical cavity are also an important factor in the photothermal effect for the coupled 2-D TMDC material. We modeled our MoS₂-coupled microdisk cavity using the finite element analysis software package, COMSOL. The model includes a 3.8 μm radius silicon dioxide cylinder with a height of 285 nm, which is connected to a Si thermal heatsink by a Si stem of varying radius and can be seen in **Figure 4.5**. For simplicity, we modeled the MoS₂ flake area as one third of the microdisk area and the absorption of the MoS₂ as a heat source confined to 500 nm wide radial segment within that third of the microdisk. **Figure 4.5a** shows the results for 0.55 mW of heat as a consequence of absorbed laser power and the resulting heating of the disk. The heatmap shows the thermal distribution around the top surface of the microdisk with a maximum temperature of 550 K at the edge. This heating level was chosen to match the approximate temperature at the previously discussed damage threshold level for MoS₂. The upper portion of **Figure 4.5a** shows a temperature line scan along the diameter of the microdisk perpendicular to the flake orientation. We then looked at the peak temperature

observed for not only different absorbed power levels (**Figure 4.5b**) but various stem radii as well as (**Figure 4.5c**). From this, it is clear that the higher thermal conductivity of the Si pillar (as seen in the inset of **Figure 4.5a**) has a large effect on the thermal distribution and maximum observed temperature. The stem radius is determined by the amount of Si undercut from the SiO_2 microdisk during the fabrication process, and a smaller stem leads to more thermal isolation and a higher overall peak temperature. Similar but less pronounced effects from thermal heating of optical cavities can be seen for GaP-based photonic crystal cavities as well as seen in **Figure 4.6**.

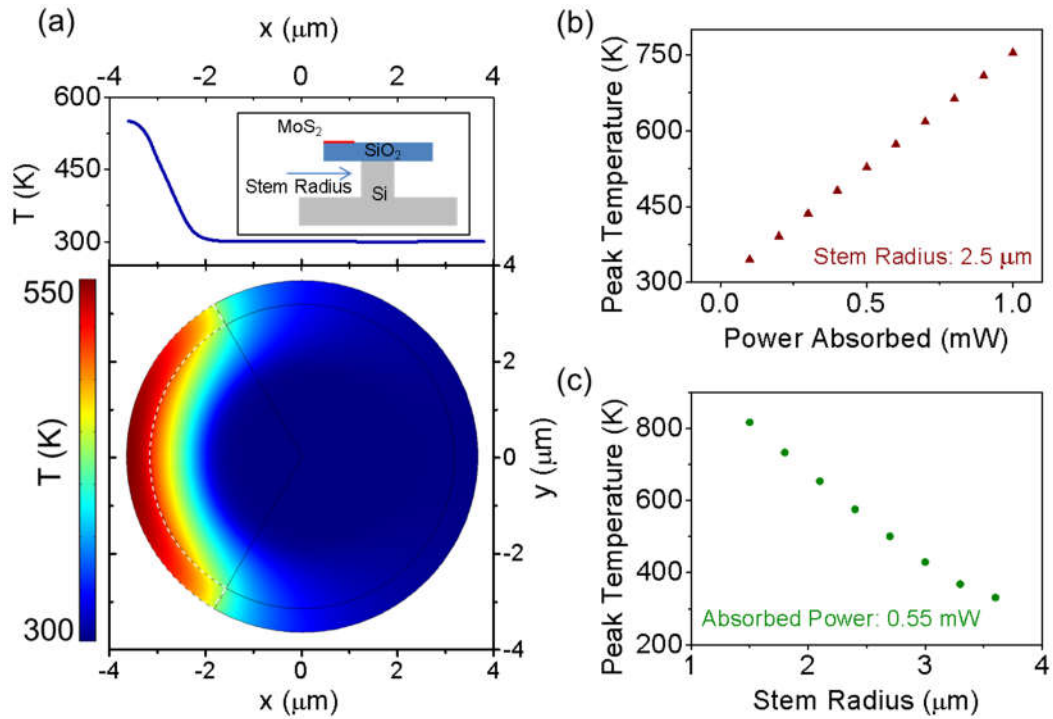


Figure 4.5 (a) COMSOL simulation result for 0.55 mW of heating of a silicon dioxide disk of radius 3.8 μm . (lower panel) Heat map of the temperature distribution throughout the microdisk with the heat source confined to the area outlined by the white dotted line. (upper panel) Line scan of the temperature along the horizontal axis of the microdisk. (inset) Cartoon of the microdisk geometry showing the stem radius. (b) Maximum temperature observed in the microdisk of a 2.5 μm stem radius at different absorbed power levels. (c) Maximum temperature observed for a microdisk of varying stem radius and 0.55 mW of absorbed power.

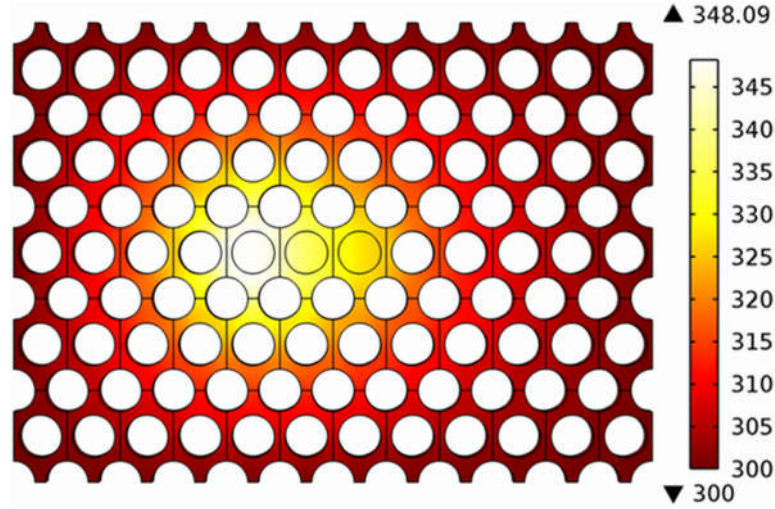


Figure 4.6 COMSOL simulation of a GaP photonic crystal membrane 125 nm in thickness with a pitch of 200 nm and hole radius 0.4 times the pitch. 0.55 mW of heat power was applied to the defect and shows a 48.09 K increase in temperature.

In order to further study and minimize the photothermal effect, we studied the heating of the microcavity in the time domain. **Figure 4.7a** shows the temperature of our modeled microdisk shortly after the onset of heating. The rate of heating decays exponentially and reaches steady state with a time constant, τ , of 395 ns. This suggests that instead of applying a CW illumination to the MoS₂ in the microdisk, short, pulsed laser illumination shorter than the time constant will mitigate the effects of heating and damage. Since we do not have the means to probe the temperature of the microdisk at the sub-microsecond level, to experimentally study the heating of the cavity at this time scale, we must do so through indirect methods. The data in **Figure 4.2c** shows the correlation between the PL peak position and the temperature of the MoS₂ flake. By measuring the PL spectra and its peak position at different illumination pulse lengths, we can infer the temperature of the MoS₂ for an illumination pulse of that time interval. **Figure 4.7b** shows the data for the increase in temperature from the shortest pulse of 50

ns for increasingly longer pulses. From this, we can effectively measure the temperature of the microdisk as a function of time in the sub-microsecond regime. This method can also be utilized to probe the thermos-temporal response for other optical systems at short time scales. For this system, steady state is reached within 1 μ s and the heating has a time constant of 184 ns. This value is a factor of ~ 2 less than that predicted by the model. We attribute this difference to experimental deviations from ideality and changes in thermal conductivity at the nanoscale, especially after chemical processing. Thus, we have determined that the photothermal effect can be minimized using pulsed excitation of a shorter time than the time constant of the optical cavity system.

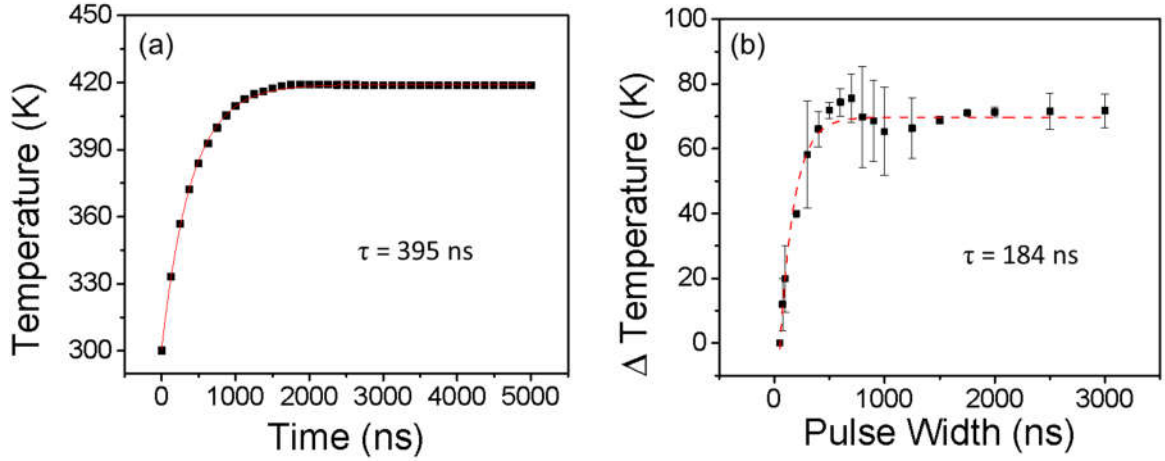


Figure 4.7 (a) COMSOL simulation result of a microdisk heating at short time scales. The temperature reaches a steady state with a decay time constant of 395 ns. The absorbed power was set to be 0.55 mW with a stem radius of 3.0 μm . (b) Experimental results for the change in temperature in the microdisk after illumination with a pulsed laser excitation of different pulse widths. The change in temperature was measured from the shift in the PL peak position of the MoS_2 on the microdisk. The change in temperature stabilizes with a decay time constant of 184 ns.

4.3 Conclusions

In conclusion, we have identified a significant photothermal effect that is inherent to optical cavity-coupled 2-D TMDC material systems. This effect has been explored for MoS_2 and WSe_2 in this work and has been similarly reported upon for other materials as well. We have shown that cavity design and fabrication should consider thermal arguments alongside optimizing optical performance. Pulsed excitation of the optical cavity system can not only help mitigate this effect but also be used as a tool for investigating the thermo-temporal response. We believe that this work will provide insight into the fields of optical cavities and 2-D TMDCs as the intersection of these two fields grows in prominence and importance in the future.

4.4 Methods

4.4.1 *MoS₂ & WSe₂ Exfoliation.*

The MoS₂ flakes were created from bulk single-crystalline MoS₂ (SPI) through mechanical exfoliation onto 285 nm thermally grown silicon dioxide on silicon. Roughly 8 nm of SiO₂ was deposited by atomic layer deposition (Cambridge Nanotech, Savannah 200) and quantified using a reflectance monitor (Filmetrics F40). WSe₂ single crystals were grown by the Tongay Group.

4.4.2 *Microdisk Fabrication*

ZEP 520A (Zeon Chemicals) was spin-casted onto the sample and patterned into a notched 7.6 μ m diameter disk on top of the located MoS₂ flake using e-beam lithography (Elionix, ELS-7500). Following development of the resist in o-xylene, the uncovered silicon dioxide was etched using reactive ion etching (Oxford Instruments, Plasmalab 80 Plus) with 38 sccm Ar and 12 sccm CHF₃. Following etching, the remaining resist was stripped using acetone and subsequently Remover 1165 (Microposit) at 75 °C for 15 minutes each. To form the microdisk structure, the underlying Si was undercut using a XeF₂ etch (Xactix, e-1).

4.4.3 *Temperature dependent PL Measurement*

Temperature dependent photoluminescence was measured in an inverted microscope (Nikon TE-2000U) setup from excitation by a 405 nm laser diode (Nichia Corp.). The sample was attached with silver epoxy to a joule heating stage whose temperature was measured by a thermocouple. Background corrected PL was measured with a 6 x 45 second integration time. Each sample was heated from room temperature to 172 °C (the

maximum temperature achievable with the heating stage) and then cooled to room temperature. PL measurements were made at 15 °C intervals and the temperature was kept constant within roughly ± 0.5 °C during each PL measurement. Between each measurement the focus and positioning of the monolayer flake was adjusted and verified to be consistent with the previous measurements.

4.5 References

- 1 Splendiani, A. *et al.* "Emerging Photoluminescence in Monolayer MoS_2 ". *Nano Letters* **10**, 1271 (2010).
- 2 Mak, K. F., Lee, C., Hone, J., Shan, J. & Heinz, T. F. "Atomically Thin MoS_2 : A New Direct-Gap Semiconductor". *Physical Review Letters* **105**, 136805 (2010).
- 3 Tonndorf, P. *et al.* "Photoluminescence Emission and Raman Response of Monolayer MoS_2 , MoSe_2 , and WSe_2 ". *Optics Express* **21**, 4908 (2013).
- 4 Tongay, S. *et al.* "Defects Activated Photoluminescence in Two-Dimensional Semiconductors: Interplay between Bound, Charged, and Free Excitons". *Sci. Rep.* **3** (2013).
- 5 Malard, L. M., Alencar, T. V., Barboza, A. P. M., Mak, K. F. & de Paula, A. M. "Observation of Intense Second Harmonic Generation from MoS_2 Atomic Crystals". *Physical Review B* **87**, 201401 (2013).
- 6 Zeng, H. *et al.* "Optical Signature of Symmetry Variations and Spin-Valley Coupling in Atomically Thin Tungsten Dichalcogenides". *Sci. Rep.* **3** (2013).
- 7 Sallen, G. *et al.* "Robust Optical Emission Polarization in MoS_2 Monolayers through Selective Valley Excitation". *Physical Review B* **86**, 081301 (2012).
- 8 Mak, K. F., He, K., Shan, J. & Heinz, T. F. "Control of Valley Polarization in Monolayer MoS_2 by Optical Helicity". *Nat Nano* **7**, 494 (2012).
- 9 Sobhani, A. *et al.* "Enhancing the Photocurrent and Photoluminescence of Single Crystal Monolayer MoS_2 with Resonant Plasmonic Nanoshells". *Applied Physics Letters* **104**, 031112 (2014).
- 10 Butun, S., Tongay, S. & Aydin, K. "Enhanced Light Emission from Large-Area Monolayer MoS_2 Using Plasmonic Nanodisc Arrays". *Nano Letters* **15**, 2700 (2015).
- 11 Lee, B. *et al.* Fano Resonance and Spectrally Modified Photoluminescence Enhancement in Monolayer MoS_2 Integrated with Plasmonic Nanoantenna Array. *ArXiv e-prints* **1503**, 3440 (2015).
- 12 Vahala, K. J. "Optical Microcavities". *Nature* **424**, 839 (2003).
- 13 Schwarz, S. *et al.* "Two-Dimensional Metal-Chalcogenide Films in Tunable Optical Microcavities". *Nano Letters* **14**, 7003 (2014).

- 14 Reed, J. C., Zhu, A. Y., Zhu, H., Yi, F. & Cubukcu, E. "Wavelength Tunable Microdisk Cavity Light Source with a Chemically Enhanced Mos₂ Emitter". *Nano Letters* **15**, 1967 (2015).
- 15 Ye, Y. *et al.* Monolayer Excitonic Laser. *ArXiv e-prints* **1503**, 6141 (2015).
- 16 Gan, X. *et al.* "Controlling the Spontaneous Emission Rate of Monolayer Mos₂ in a Photonic Crystal Nanocavity". *Applied Physics Letters* **103**, 181119 (2013).
- 17 Wu, S. *et al.* "Control of Two-Dimensional Excitonic Light Emission Via Photonic Crystal". *2D Materials* **1**, 011001 (2014).
- 18 Wu, S. *et al.* "Monolayer Semiconductor Nanocavity Lasers with Ultralow Thresholds". *Nature* **520**, 69 (2015).
- 19 Liu, X. *et al.* "Strong Light–Matter Coupling in Two-Dimensional Atomic Crystals". *Nat Photon* **9**, 30 (2015).
- 20 Wang, H., Zhang, C. & Rana, F. "Ultrafast Dynamics of Defect-Assisted Electron–Hole Recombination in Monolayer Mos₂". *Nano Letters* **15**, 339 (2015).
- 21 Shi, H. *et al.* "Exciton Dynamics in Suspended Monolayer and Few-Layer Mos₂ 2d Crystals". *ACS Nano* **7**, 1072 (2013).
- 22 Tongay, S. *et al.* "Thermally Driven Crossover from Indirect toward Direct Bandgap in 2d Semiconductors: Mose₂ Versus Mos₂". *Nano Letters* **12**, 5576 (2012).
- 23 Soklaski, R., Liang, Y. & Yang, L. "Temperature Effect on Optical Spectra of Monolayer Molybdenum Disulfide". *Applied Physics Letters* **104**, 193110 (2014).
- 24 Lavik, M. T., Medved, T. M. & Moore, G. D. "Oxidation Characteristics of Mos₂ and Other Solid Lubricants". *A S L E Transactions* **11**, 44 (1968).
- 25 He, Z. *et al.* "Layer-Dependent Modulation of Tungsten Disulfide Photoluminescence by Lateral Electric Fields". *ACS Nano* **9**, 2740 (2015).

CHAPTER 5: Future Directions and Summary

5.1 Aluminum and Copper Nanoantennas

In **CHAPTER 2**, it was shown that graphene passivation of silver nanoantennas preserved their excellent optical properties. Along with gold and silver nanoantennas, the Van Duyne group has seen that Al nanoparticles can support localized surface plasmons, most efficiently in the near-UV¹. They have reported about a 2 nm oxide layer forms on the surface of the particles that red-shifts the resonance of the particles. Similarly, Langhammer *et al.* has reported that: “formation of a thin 2-3 nm native oxide layer on the Al surface is almost instantaneous after its exposure to (humid) air. The thickness of this layer continuously keeps increasing over several days or weeks, however, at orders of magnitude slower rate than the initial one.”² The oxidation of aluminum has been traditionally seen as self-passivating, as in it limits further oxidation of the metallic aluminum. However, at the limit of decreasing particle sizes, the kinetics and amount of oxide formation becomes dependent on the size and shape of the particles, as seen in **Figure 5.1a**.³

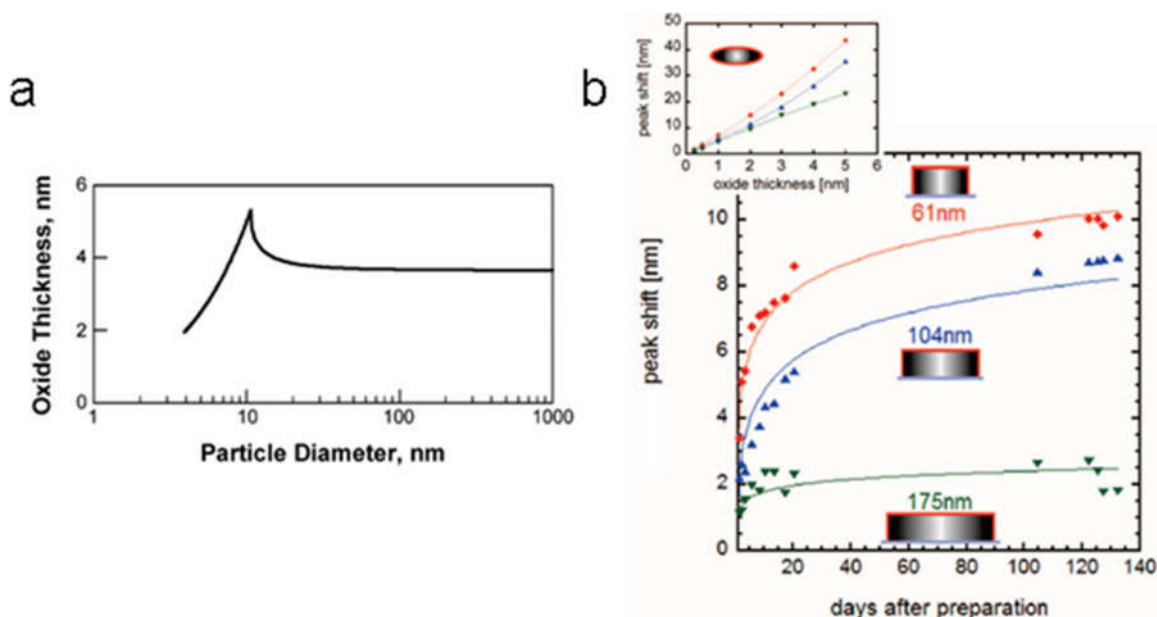


Figure 5.1 (a) Graph showing how Al particles smaller than 10 nm show fully oxidized particles, whereas particles larger than 10 nm show extended aging with a slow increase in the oxide thickness up to ~20 nm particles. Reproduced from Ref. ³ (b) Graph showing the LSPR peak shift with increasing particle oxidation over several months, with the inset showing the calculated peak shift with oxide layer thickness. Reproduced from Ref. ².

The work by Langhammer² shows that there is an additional shift in the LSPR peak of Al nanodisks of 20 nm height and various diameters in **Figure 5.1b**. This shift can be as much as 10 nm over the course of several months; however, much of this occurs within the first 20 days of the exposure. Thus, while graphene coverage may not be able to prevent the instantaneous formation of the alumina passivation layer, it is very plausible that it can prevent further oxidation and degradation of the nanoparticles after the initial instantaneous oxide formation.

Previously reported literature shows that Al nanoantennas can support localized surface plasmons, and that oxidation of Al at the nanoscale will negatively affect the optical properties of said nanoantennas. This effect is very similar to that of the

sulfidation of silver nanoparticles. Thus, the natural extension is to also study the effect of graphene passivation of Al nanoantennas. Fabrication of the Al nanoantennas could proceed in an analogous method to that of the Ag nanoantennas replacing the Ge adhesion layer with one of Ti. The diameter, height, spacing and resulting resonance should be engineered through FDTD simulations. Measurement of the resonance in the UV would be done using a mercury arc light source and spectrometer attached to an inverted microscope. The resonance should be targeted at the high 300 nm range to complement the wavelength range of the light source. The graphene passivated Al nanoantennas could also be compared to bare Al nanoantennas either over a long time scale or with an accelerated oxidation environment.

Much like those of Al or Ag, copper nanoparticles also can support localized surface plasmons. Also much like Al and Ag, Cu suffers from environmental degradation through reaction with the air. Unlike Al, copper does not form a self-passivating oxide layer, leading to further oxidation of the metallic surface than that of metallic Al.⁴ The copper oxides (CuO and CuO₂) continue to degrade the electronic and optical properties of copper as it continues to oxidize. The Van Duyne group has been able to show that removal of the copper oxide layer through acetic acid etching reveals metallic Cu particles that can support optical resonances in an inert atmosphere.⁵ **Figure 5.2** shows the evolution of the optical response to oxidized Cu nanoparticles as they undergo increasing amounts of acetic acid exposure. Oxidized particles before acetic acid etching (t_1 in **Figure 5.2**) shows a completely damped optical resonance, while 20s of acetic acid etching (t_5 in **Figure 5.2**) shows a strong optical response.

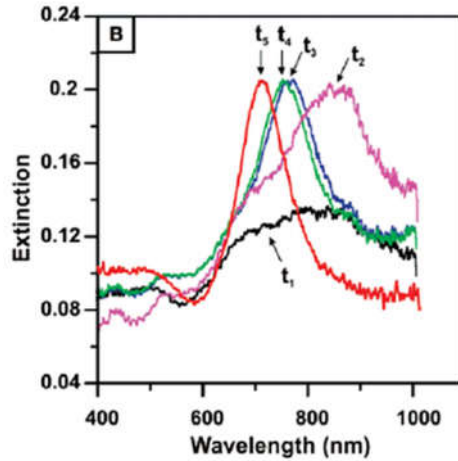


Figure 5.2 Optical spectra of Cu nanoparticles with 0 to 20s (t_1 to t_5) of acetic acid etching. Reproduced from Ref. ⁵.

Preliminary data in **Figure 5.3a** and **Figure 5.3b** shows that as-deposited Cu nanoparticles also supports optical resonances with steadily increasing plasmon peak resonance and width. This data is taken across 13 days without a graphene passivation layer showing that oxidation of the copper nanoparticles does not occur instantaneously and to a degree at which no optical resonances can be supported. The copper oxidation happens slowly over the course of weeks for nanoparticles in ambient laboratory air. Thus, proper passivation of Cu nanoparticles with graphene will have a large effect in preventing their continued oxidation and degradation of optical properties. To test the graphene passivation of Cu nanoantennas, nanoantennas were fabricated using methods similar to those of Ag nanoantennas. **Figure 5.3c** & **Figure 5.3d** are SEM images of Cu nanoantennas with a monolayer graphene passivation layer. The images selectively show cracks in the graphene film with the lighter areas having graphene coverage. The nanoantennas were annealed in air for 2 hours at 200 °C to mimic an accelerated oxidation environment. The areas not covered by graphene show the morphological

changes due to surface oxidation while those covered by graphene remain relatively smooth.

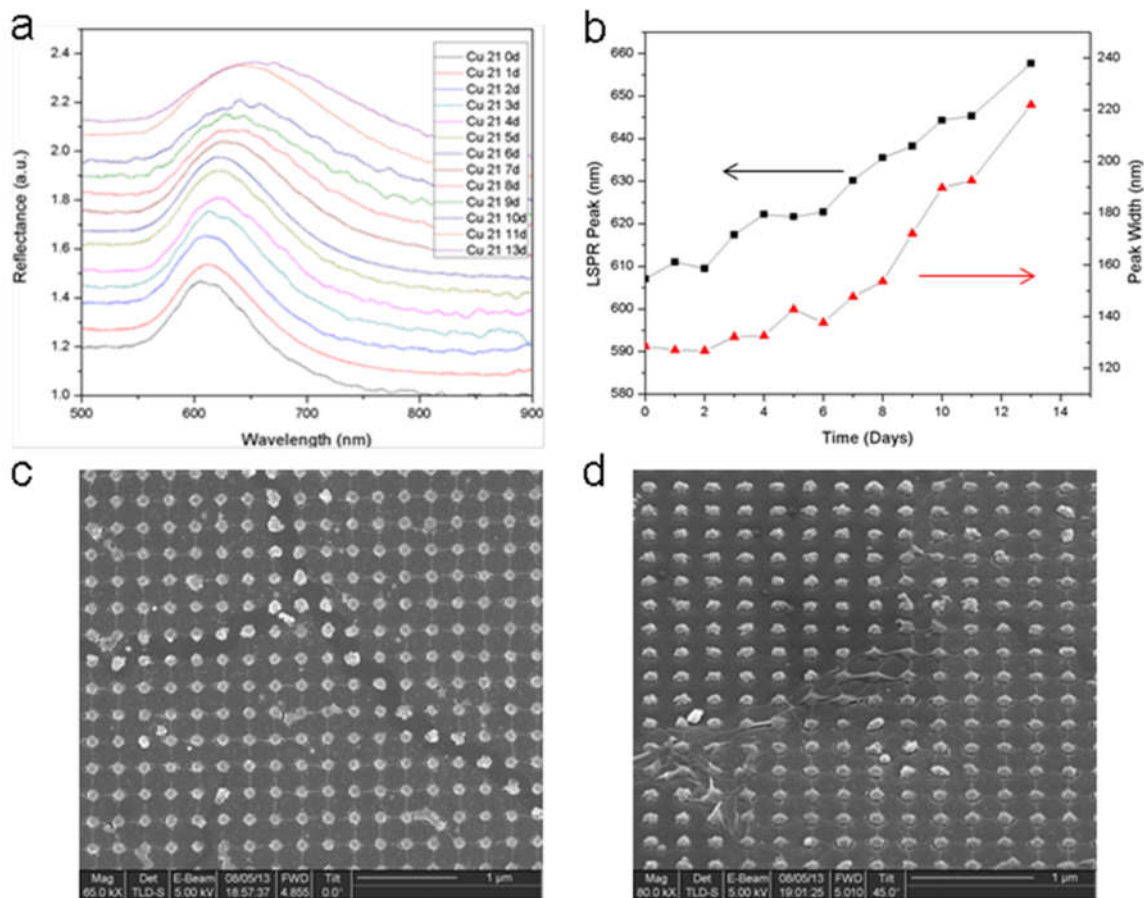


Figure 5.3 (a) Reflection spectra as a function of time and (b) extracted LSPR peak position and width for bare Cu nanoparticles over a 13 day period. SEM images in (c) top down and (d) tilted view of Cu nanoantennas partially covered with monolayer graphene after 2 hours at 200 °C.

Through literature and some preliminary work, it has been shown that not only can copper nanoparticles support surface plasmon resonances, but like those of Ag and Al, they are affected by reaction with ambient air. These effects are detrimental to the longevity of any devices based on copper nanoantennas with ~70% increase in the peak

width of the resonance. A monolayer graphene passivation layer over fabricated Cu nanoantennas has proven to prevent morphological changes through oxidation of the Cu particles. In order to show that the optical properties of the Cu nanoantennas can be preserved by the graphene, more samples need to be made. Previous Cu nanoantenna samples with graphene passivation either show no plasmon peak or have inadequate graphene coverage for passivation.

5.2 Graphene-Enabled Ag Nanoantennas for Protein Sensing

Graphene passivation of metallic nanoparticles does not only offer protection from reactive species in the air, but is also a simple method for creating a highly integrated biochemical sensor using the graphene as a functional layer. Because of its delocalized pi-bonding, graphene is a great substrate for adsorption of the hydrocarbon chains in various biomolecules, vastly improving the limit of surface adsorption. Sensing through localized surface plasmon resonances also decays exponentially within tens of nanometers from the surface of the particles, making graphene near-transparent because of its thin, single atomic layer nature.

Previous studies in the Cubukcu Lab have shown the use of graphene-functionalized biomolecular sensors using gold nanoantennas as well as silicon nanowires.^{6,7} After the transfer of graphene onto these materials, mouse IgG and its conjugate binding protein A/G were applied to the graphene through drop casting. A/G was applied first which floods the surface of the graphene, adsorbing to the active sites and, in turn, only offer a

binding site to the IgG protein. Subsequently, increasing concentrations of the IgG protein are added to the samples.

Figure 5.4a,b shows the optical spectrum of the Au nanoantennas and Si NW samples with increasing concentrations of IgG, showing measurable shifts of up to 8 and 6 nm, respectively, at protein concentration saturation. Silver nanoantennas passivated and functionalized by graphene have also been fabricated to study its ability to sense increasing levels of biomolecules.

Figure 5.4c shows the optical spectra of a fabricated Ag nanoantenna array with subsequent additions of protein. The data shows a shift in the resonance peak by more than 100 nm, over an order of magnitude larger for the same protein concentration added to gold nanoantennas and silicon nanowires. This shift is not likely caused by oxidation because of the consistency of the peak widths over the different spectra.

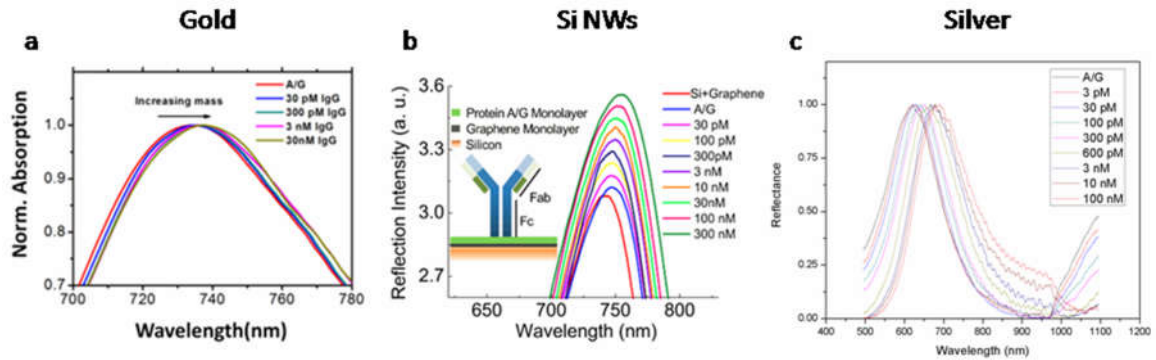


Figure 5.4 Spectra of graphene-functionalized (a) gold nanoantenna (b) Si nanowire and (c) silver nanoantenna arrays with an A/G binding protein and increasing concentrations of IgG. Reproduced from Ref.⁶ and Ref.⁷

The work in **CHAPTER 2** as well as the preliminary work here has shown that silver nanoparticles passivated and functionalized by graphene can sense the addition of increasing concentrations of IgG protein through shifts in the optical spectra. This has

great potential use as the active element in biosensors. The shifts for silver nanoantennas are much larger than that of gold nanoantennas and Si nanowires with graphene and protein additions in a near-identical method. The silver nanoantennas are also protected from any surface reactions as a result of the buffered saline environment of the protein.

More samples need to be fabricated and tested to verify the shifts seen with respect to the protein loading. If the spectral shifts are consistent and equally large as in the preliminary data, then this would add significant weight to the claim of the benefits of Ag as a functional plasmonic material when encapsulated with graphene. The protein conjugate A/G and IgG is nonreversible in its binding; however it would be interesting to study the use of Ag nanoparticles *in situ*. By choosing a protein conjugate pair that can be reversibly bound, we can create a PDMS flow cell to monitor the change in the optical spectra in real time as the protein binds and unbinds from the surface. Highly sensitive, reversible sensors that can detect specific biomolecules *in situ* are of great importance in the biomedical field⁸.

5.3 Cavity-Coupled MoS₂ Microdisks for Protein Sensing

The work in **CHAPTER 3** set the stage for a microcavity with an integrated 2D light source that could be used as a sensing platform. Attachment of adsorbates to the surface of the microcavity will lead to changes in the local dielectric environment. These changes can influence the spectral position of the resonant cavity modes. The shift in these modes can be calibrated and quantified to deduce the amount of adsorbate. This technique of using optical microcavities for spectroscopy and sensing is well established.⁹ The novelty of this idea is in the incorporation of the 2D light source. This allows for facile fabrication with the inclusion of CVD-grown MoS₂. Additionally, the MoS₂ acts as the functionalization basis layer, allowing for a greater level of ease in the functionalization of the cavity to the target species.

Figure 5.5 shows SEM images of the fabricated silica microdisk with incorporated MoS₂ flake. The darker contrast part in **Figure 5.5a** shows the location of the MoS₂ as well as the defect notch patterned into the bottom of the disk. In contrast to the fabrication of the microdisks in **CHAPTER 3**, these MoS₂ flakes were grown through CVD methods in the Johnson Lab. This allows for a greater density of monolayer material and less involved fabrication methods. In short, SiO₂/Si substrates with 285 nm of thermally grown oxide are patterned by e-beam lithography with ZEP-520A resist. The resist disks act as the mask for the subsequent reactive-ion etch that etches through the surrounding, exposed portion of the SiO₂ on the substrate. Then, the underlying Si is etched away through XeF₂ isotropic etching to release the edges of the disk structure. Afterwards, CVD-grown MoS₂ flakes are transferred onto a sample substrate containing

an array of these microdisk structures. Suitable candidate samples are identified by optical microscopy based on the quality and location of the MoS₂ flake in relation to the microdisk. Similar to the work in **CHAPTER 3**, suitable samples have the MoS₂ flake located toward the edge of the microdisk opposite to the notch defect.

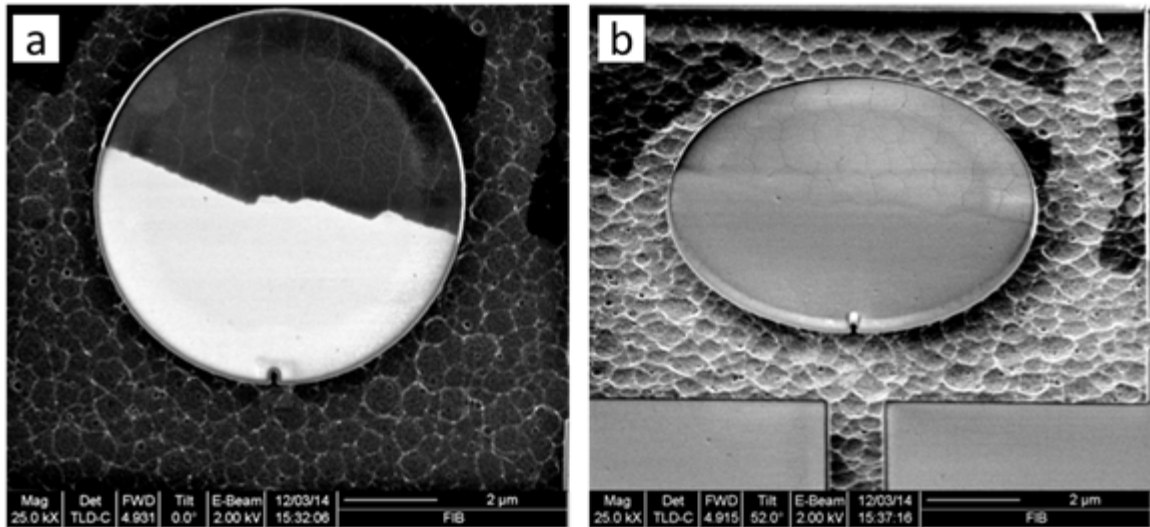


Figure 5.5 (a) Top-down and (b) 52° tilted SEM images of fabricated SiO₂ microdisk cavities with incorporated MoS₂ flakes. The darker, wrinkled portion in panel (a) is the location of the MoS₂ flake.

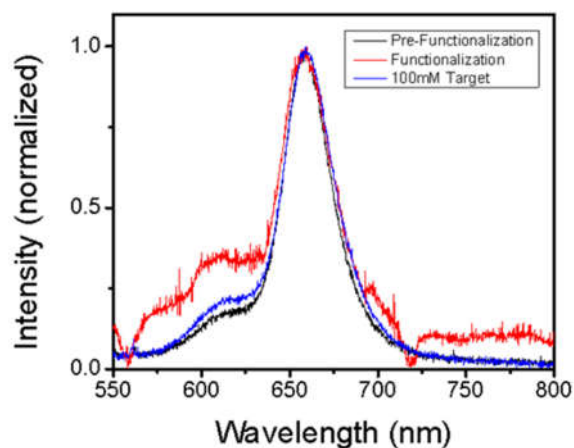


Figure 5.6 Optical spectra of an MoS₂ flake on a flat 285 nm SiO₂/Si substrate before protein functionalization, after binding protein functionalization, and after addition of 100 mM of target protein.

The identified samples were then functionalized with a binding protein that chemically attaches to the surface of the MoS₂. This binding protein then has a specific protein binding site that will allow attachment of the final target protein to attach to the surface of the MoS₂. **Figure 5.6** shows the optical PL spectra of a MoS₂ flake on a flat substrate before and after these functionalization steps. We can see that the PL spectrum is neither affected by the attachment of the functionalization protein nor the addition of large amounts of the target protein.

From **Figure 5.7**, we see the emission from the coupled microdisk modes collected from the notch. Prior to any protein functionalization, a microdisk with a freshly transferred CVD-grown MoS₂ flake shows pronounced cavity mode peaks with Q~300 in this sample (as shown by the black curves in **Figure 5.7**). After the functionalization protein has been attached to the surface of the MoS₂, We see a dramatic change to the optical spectrum. This comes in the form of a much higher background PL

from the MoS₂ flake in comparison to the cavity modes (as shown by the red curves in **Figure 5.7**). The cavity modes are still visible in this spectrum, although muted. We can see in **Figure 5.7b** that the peaks shifts ~ 10 nm or greater than 10 nm, depending on if the shift in the cavity mode exceeded the FSR for this cavity. The spectrum after addition of 100 mM of the target protein consists entirely of the background PL from the MoS₂ flake, lacking observable peaks from the cavity modes (as shown by the blue curves in **Figure 5.7**).

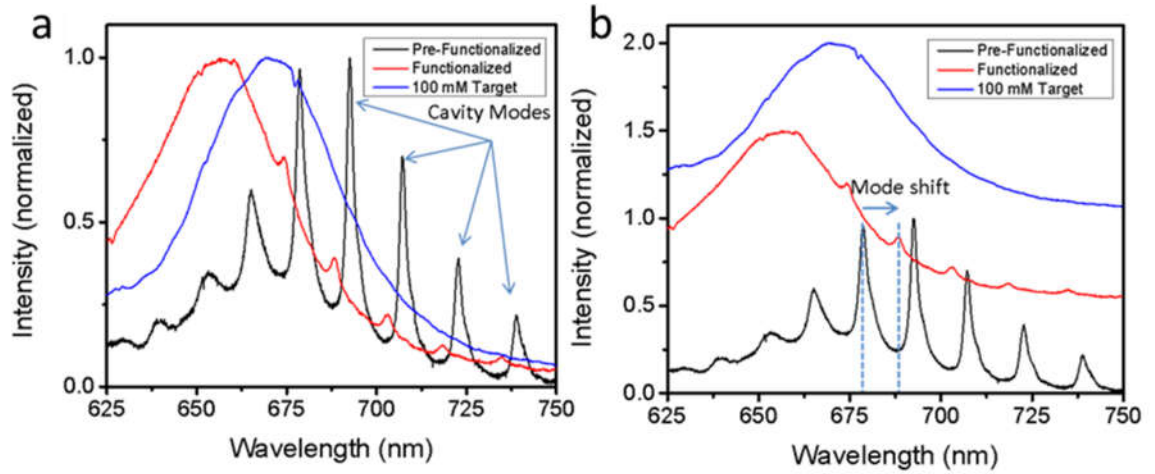


Figure 5.7 Cavity-mode emission from the microdisk notch before and after functionalization of the binding protein, as well as after addition of 100 mM of the target protein. Panels (a) and (b) show the same data with an offset in the latter added for clarity.

From this, we can determine that we can detect the attachment of the functionalization protein through changes in the optical spectrum. The inclusion of the functionalization protein to the surface of the MoS₂ flake as well as the surface of the microdisk causes a shift in the resonant frequency of the cavity coupled modes. This is easily detectable as the shift in the mode is relatively large, at least 5-times the FWHM of

the cavity modes and possibly larger if the shifts are larger than the FSR. The spectra after the addition of the proteins does start to become overwhelmed with the background PL of the MoS₂ flakes. This could be that the attachment of the protein to the surface of the microcavity decreases the Q of the cavity by increasing the surface scattering/absorption by decreasing Q_{scatt} as seen in equation 49.

Increased protein aggregation may be aggravating the increased observed background PL in the spectrum as the target protein may have reached the end of its shelf life. Improvements in the method of optical characterization of the microdisks with improved spatial exclusion of areas around the microdisk notch could also help improve the observation of the cavity modes. These experiments have proved that we can observe, optically, the addition of small amounts of biologically-relevant molecules using a 2D semiconducting material. More samples with smaller amounts of target protein need to be produced and characterized to determine the concentration limit to which we can detect shifts in the optical spectrum.

5.4 Large Radius, High- Q Microdisk Cavities with CVD-Grown MoS₂ for High-Fluence Optical Pumping

In **Section 1.5**, it was shown that the higher the azimuthal mode number, m , for a WGM cavity, the higher the radial field localization. In **CHAPTER 3**, it was also shown that larger microdisk cavities would yield larger mode number m as well as higher Q resonances. We were limited in **CHAPTER 3** by the size of the mechanically exfoliated MoS₂ flake to microdisks of radius 3.8 μm . Replacing the source material for our 2D TMDC to CVD-grown MoS₂ from the Johnson Lab, we are no longer constrained by this

parameter. CVD-grown MoS₂ flakes are triangular or hexagonal flakes with edge lengths on the order of 10-20 μm per edge. In contrast, typical mechanically exfoliated MoS₂ flakes are rectangular in nature and on the order of 5 μm for the long dimension. Additionally, mechanically exfoliated monolayer MoS₂ typically is located in very close proximity to much thicker flakes and pieces. Because of the release of this spatial constraint, we can utilize microdisk of larger sizes to enhance the quality factor of the cavity mode resonances.

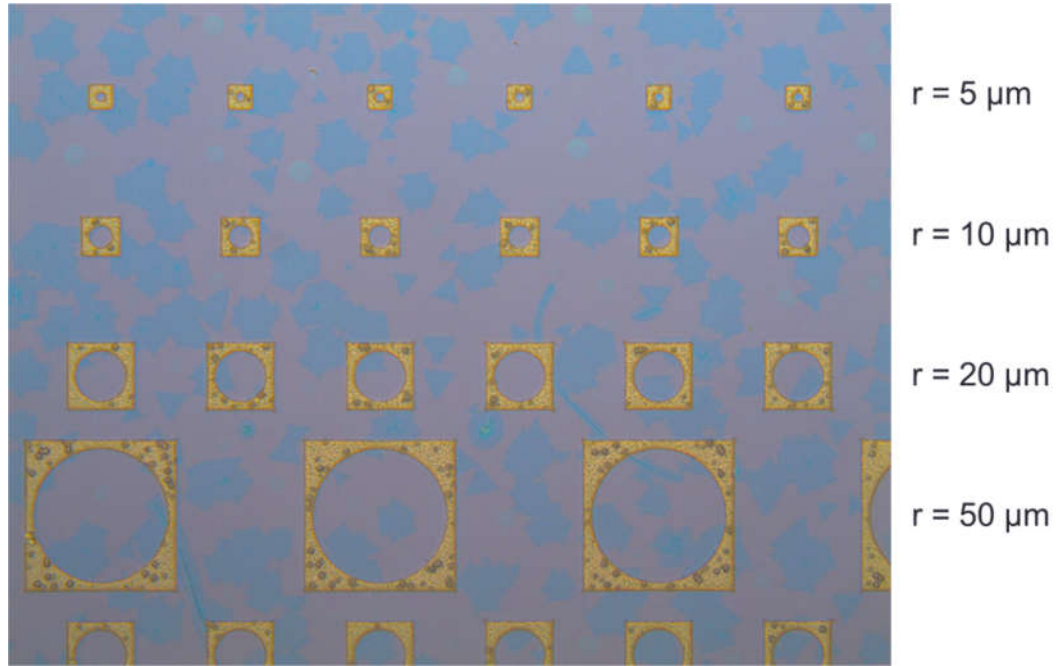


Figure 5.8 Optical image of fabricated large-radius microdisks with transferred CVD-grown MoS₂ flakes. The sizes of the disks range from 5 to 50 μm in radius.

The method for fabrication of the larger radii MoS₂-coupled microdisk structures is the same as that outlined in the **Section 5.3**. The only difference to the fabrication method is the size of the disks patterned during e-beam lithography. **Figure 5.8** is an optical image of the fabricated microdisks with the transferred MoS₂ flakes; the radii

range from 5 to 50 μm . As with the smaller sized microdisks, the microdisk flake should be located near the edge of the microdisk and far enough away from the notch to prevent collection of the background PL at the notch. Because of the size and density of the MoS_2 flakes grown through CVD methods, the microdisks of 50 μm radius tend to be too large to fit this criterion.

Figure 5.9 shows the optical spectrum collected at the notch for a microdisk of $r = 10 \mu\text{m}$. The MoS_2 flakes on the microdisks were illuminated using a continuous wave $\lambda = 405 \text{ nm}$ diode laser. The laser was driven using a pulse generator with 750 ns pulses at a frequency of 100 kHz. The laser illumination was incident upon the MoS_2 flake directly while the illumination from the locality of the microdisk notch was collected by a spectrometer. In comparison to the smaller radii microdisks in **CHAPTERS 3, 4**, and **Section 5.3**, the free spectral range is much smaller and the quality factors for the resonant modes are in the 2000-3000 range. This quality factor is similar to those of other cavity-enhanced 2D TMDC work that claim lasing of their active material.¹⁰ An exhaustive list of the spectra of different sized microdisk radius samples is listed in **APPENDIX B**.

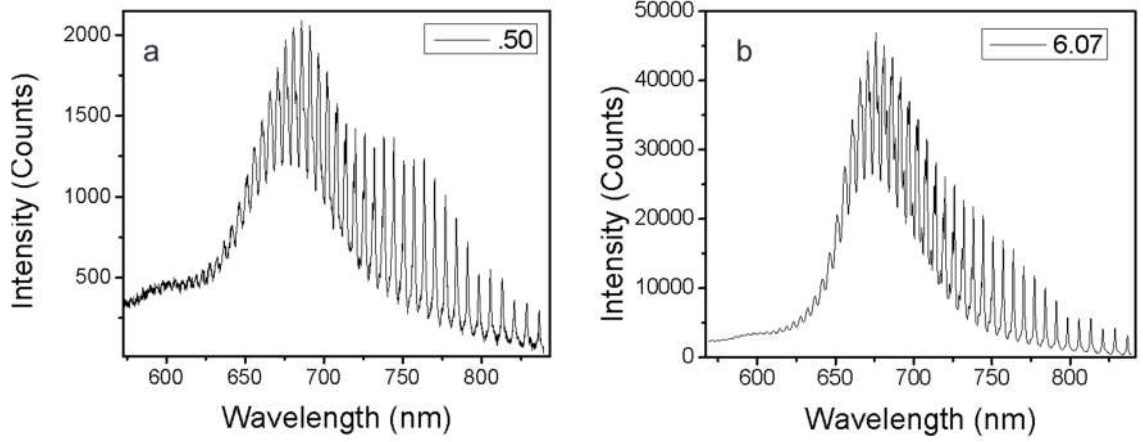


Figure 5.9 Cavity mode emission from CVD-grown MoS₂ coupled to 10 μm radius microdisk cavities. The MoS₂ is excited by a 405 nm pulse driven laser diode at 100kHz with a 750 ns pulse width. The power incident at the flake is (a) 0.50 mW and (b) 6.07 mW.

A consequence of the larger quality factor can be seen in **Figure 5.10**. Sampling at a finer spectral resolution of the resonant modes around 685 nm, we can see that the individual resonant peaks are split into two peaks. This peak splitting is result of a degeneracy formed by breaking the symmetry in a axially symmetric WGM cavity.¹¹ This occurs because of small imperfections in the fabrication process. The light circulating around the microdisk cavity counter-propagates in a left- or right-handed fashion. For truly axially symmetric cavities, this leads to identical conditions for each wave. However, the inclusion of the imperfections causes a small shift in the resonance condition for one propagation direction relative to the other. This leads to a splitting of the WGM peak into two discrete peaks. For low quality-factor cavities, this effect is not usually seen as the peaks cannot be resolved into two separate peaks. Because of the $Q = 2000\text{-}3000$ cavities, this splitting can be resolved.

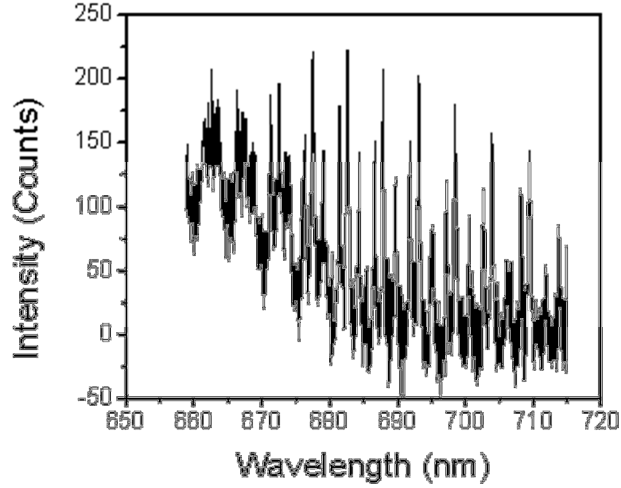


Figure 5.10 Magnified view of the optical spectra of presented in **Figure 5.9b** taken with a higher resolution diffraction grating showing the peak splitting that occurs with the high- Q cavity modes.

Figure 5.11a shows the cavity mode emission spectra at different excitation power, up to a maximum value of 6.07 mW of power. By tracking the intensity of a specific resonant mode, we can observe the changes to the emission intensity as a function of pump power. In **Figure 5.11b-e**, the resonant mode intensities at $\lambda = 675.9$ nm and $\lambda = 763.6$ nm can be seen tracked in both linear and logarithmic scales. As the excitation power increases, the output intensity does not respond in a linear fashion. The linear-scale tracking of the resonant modes show a kink-like behavior with multiple regimes of different linearity. These characteristics could be indicative of amplified stimulated emission or gain in the optical medium of this system. However, more optical pumping power needs to be applied to this system in order to fully investigate this. Our collaborator, Dr. Oulton at the Centre for Plasmonics and Metamaterials at Imperial College in London was able to investigate the effects of short pulse width, high-fluence pumping of the MoS₂ in these microdisks.

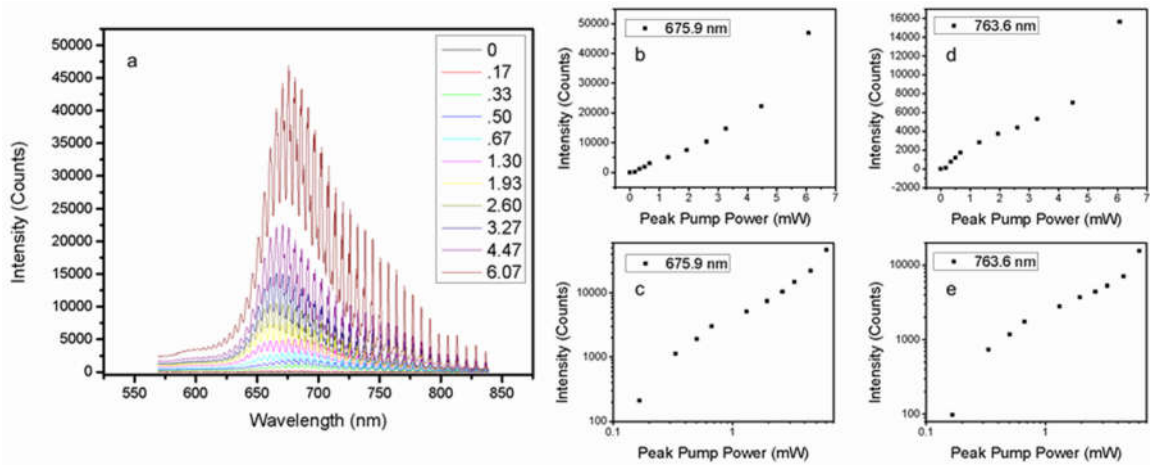


Figure 5.11 (a) Cavity-mode emission spectra of a 10 μm radius disk at different excitation power levels (in mW). Linear (a,d) and log-scale (c,e) measurement of the intensity vs pump power of the 675.9 nm and 763.6 nm resonant modes, respectively.

Microdisks of $r = 10 \mu\text{m}$ were pumped with pulses of approximately 150 fs in duration at repetition rates of either 80 kHz, 800 kHz or 8 Mhz and at a wavelength of 480 nm. Specifically, this set of data is focused around investigation of sample 11 as denoted in **APPENDIX B**, however other samples were tested with similar results. The spot was defocused in order to illuminate the entire disk. **Figure 5.12** shows the effect of increasing pump power on the spectra. Spectra were also normalized to the lowest power spectrum to see changes in the shape. While heating is associated with a red-shift in spectrum, this is not seen with pulsed illumination. Instead, an overall blue-shift is arguably observed, possibly corresponding to state filling.

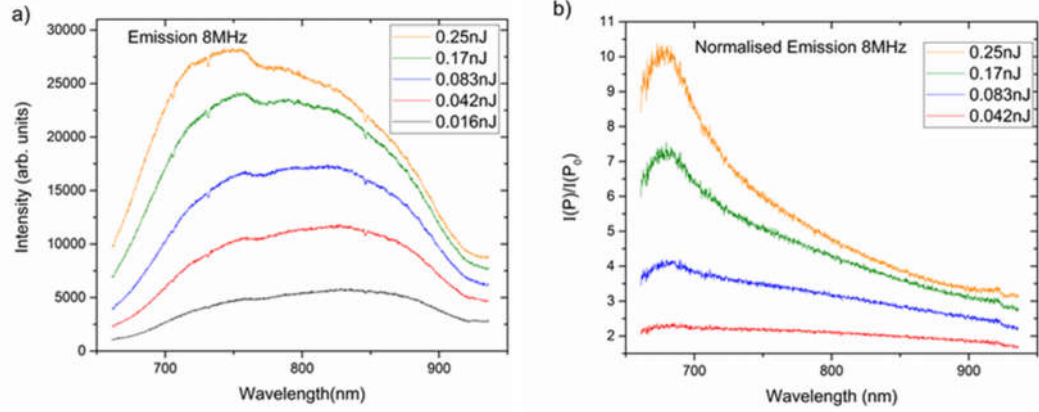


Figure 5.12 (a) Total emission and (b) emission normalized to the spectrum at 0.016 nJ pulse energy at an 8 MHz pulse repetition rate.

Figure 5.12, **Figure 5.13**, and **Figure 5.14** show the emission spectra produced by the microdisk at the various repetition rates. It also shows the emission spectra normalized to the spectrum at the lowest considered peak pulse power for each repetition rate. From these plots it is clear that the spectrum changes shape as the pulse power is increased, and emission is seen increasingly from the blue end of the spectrum, possibly from the A-exciton. Most importantly, the general spectral response does not change with decreasing repetition rate, indicating either that heating is minimal here, or that it is necessary to decrease the repetition rate to below 80 kHz.

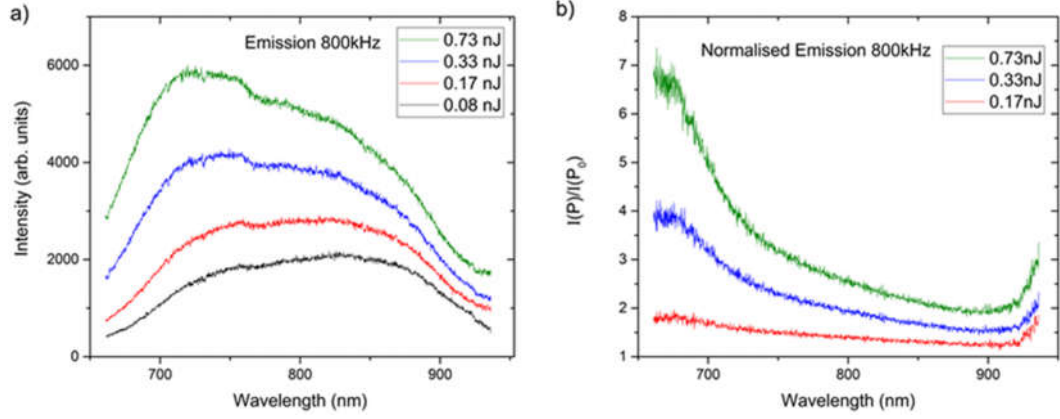


Figure 5.13 (a) Total emission and (b) emission normalized to the spectrum at 0.017 nJ pulse energy at an 800 kHz pulse repetition rate.

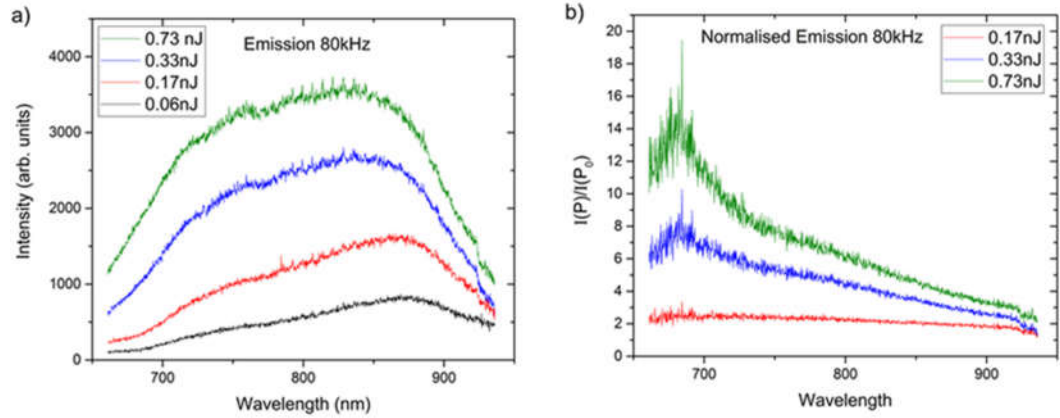


Figure 5.14 (a) Total emission and (b) emission normalized to the spectrum at 0.06 nJ pulse energy at an 80 kHz pulse repetition rate.

Following these results, the aperture was closed around the notch to try and isolate emission from the microdisk notch. Here, repetition rates of 800 kHz and 8 Mhz were used and the power was varied all the way up to the maximum available. **Figure 5.15** shows the integrated counts per pulse as the power varies; here it seems that the emission saturates at both repetition rates. The chosen repetition rate does seem to affect the saturation intensity suggesting that perhaps heating is limiting the emission. This

behavior was observed for multiple microdisks. The saturation power at the two different repetition rates were determined by fitting a curve given by:

$$I = I_0 P / (1 + P/P_{sat})$$

Here, I represents the intensity in counts per pulse, P is the pulse power and P_{sat} is the saturation power. At 80 kHz, $P_0 = 0.13$ nJ and at 8 MHz, $P_0 = 0.053$ nJ. Incidentally, saturation of the response is also a possible indication that state filling is occurring, explaining the observed blue-shift.

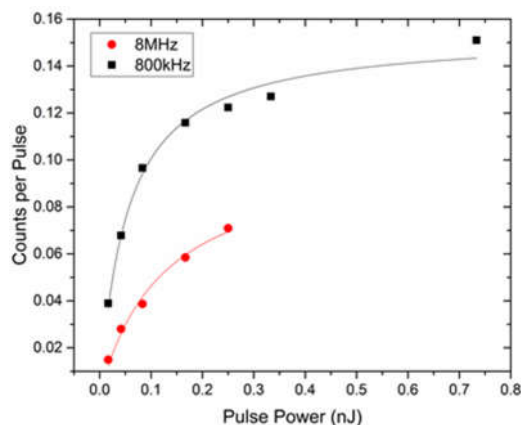


Figure 5.15 Integrated intensity of emission from notch plotted against pulse power for repetition rates of 80 kHz and 8 MHz

The spectra measured via the aperture at the notch are plotted in **Figure 5.16a,b**. Following this the intensity of two of the peaks in the spectra were monitored as pulse power was varied, as plotted in **Figure 5.16c,d**. Again the emission seems to saturate as power is increased. The background spectral shape seems to be dependent on the notch position relative to MoS₂ flakes. **Figure 5.17** shows an alternative spectrum, this time from a different $r = 10$ μm microdisk (Sample 3, **APPENDIX B**).

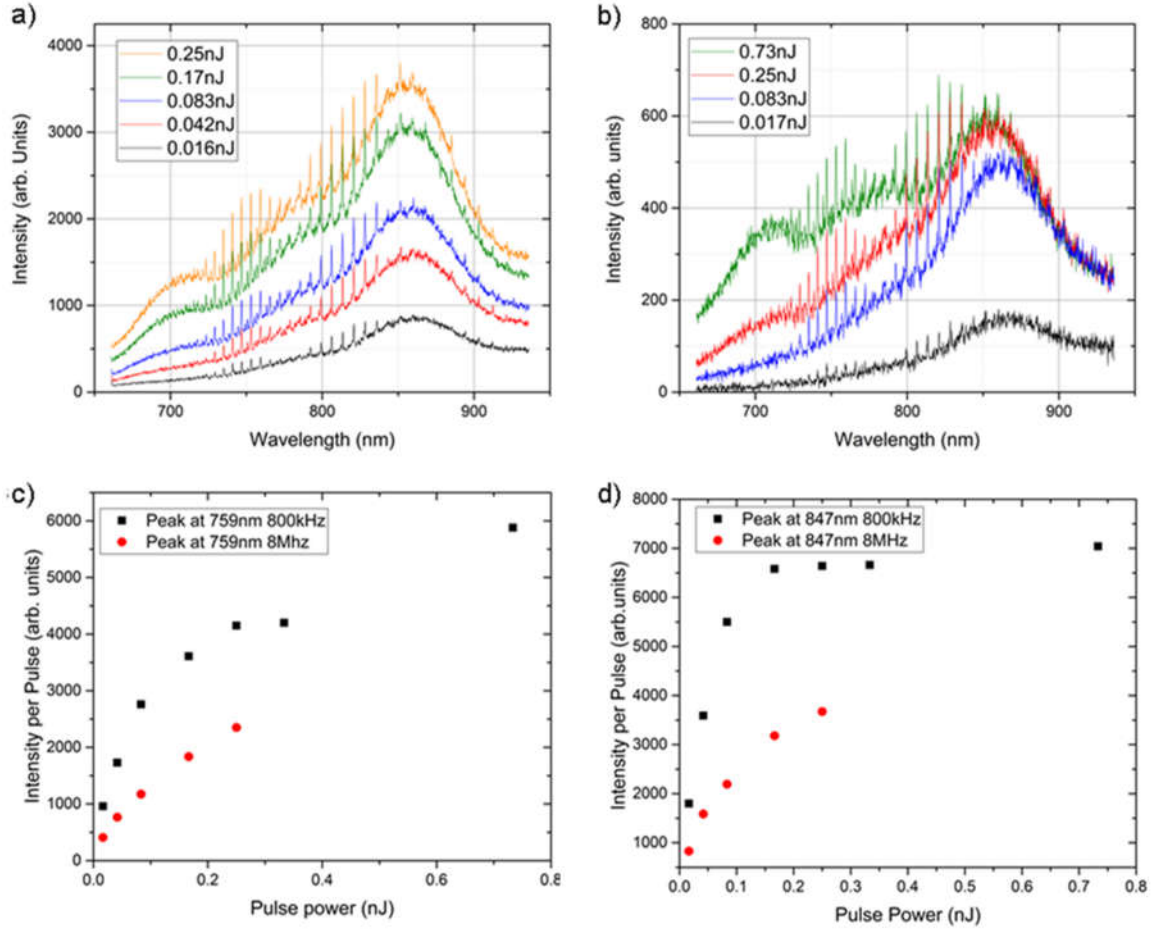


Figure 5.16 Emission spectra from notch for varying pulse power at repetition rates of (a) 8 MHz and (b) 800 kHz. Intensity of peak at (c) $\lambda = 759$ nm and (d) $\lambda = 847$ nm as incident pulse power is varied for both repetition rates of 8 MHz and 800 kHz.

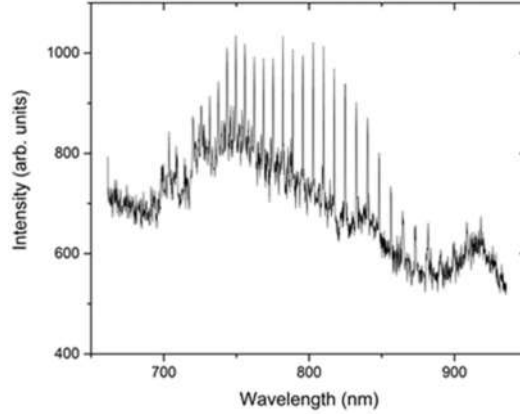


Figure 5.17 Spectrum taken from the notch of a different $r = 10 \mu\text{m}$ microdisk using a pulse power of 0.25 nJ at a repetition rate of 800 kHz.

A more systematic study of these microdisks will need to be undertaken. Characterization of the effects of repetition rates and pulse power for different microdisks of different sizes should be completed to identify trends in the data. The next step would be repeating these experiments at cryogenic temperatures. Ye *et al.*¹² has shown that going from 300 to 10 K, monolayer TMDC quantum yield increases by over an order of magnitude. Additionally, switching to another 2D TMDC, such as WS_2 which has a quantum yield almost two orders of magnitude larger than MoS_2 , could help improve the emission characteristics of these high- Q microdisks.

5.5 Summary

The work reported in the preceding chapters has covered a large range of photonic applications involving 2D materials. Graphene, with its impermeability to sulfur-containing gaseous molecules, was shown to protect silver nanoantennas from environmental degradation. The use of silver as a plasmonic sensor material, which was once hindered by degradation, was enabled through the use of graphene. This method of passivation can be applied to both aluminum and copper nanoparticles as well, preventing buildup of surface oxides that would hinder the use of those materials for plasmonic applications. Additionally, graphene enabled the functionalization of the surface of the particles to van der Waals-based protein conjugation and allows for specific molecules to bind to the surface of the graphene. With its superior optical properties, silver is also a more promising material for sensing these biological molecules.

Molybdenum disulfide was utilized in both mechanically exfoliated as well as CVD-grown forms to produce optical microcavity structures. The luminescent properties of mechanically exfoliated material were able to be enhanced through the use of atomic layer deposition and subsequent chemical doping. The incorporation of MoS₂ into the microdisk structures allowed for the observation of spectrally sharp, tunable cavity-enhanced emission and a platform for biological sensing. Thermal stability of these optical cavities is of a concern with 2D TMDC materials and was thoroughly studied. Degradation of the 2D material through oxidation at elevated temperatures is the likely cause and was shown to be mitigated through the use of pulsed excitation. High-fluence pulsed excitation and the addition of larger, higher Q microdisk cavities proved to show

interesting non-linear pump vs. emission behavior with possible signs state filling and population inversion.

5.6 References

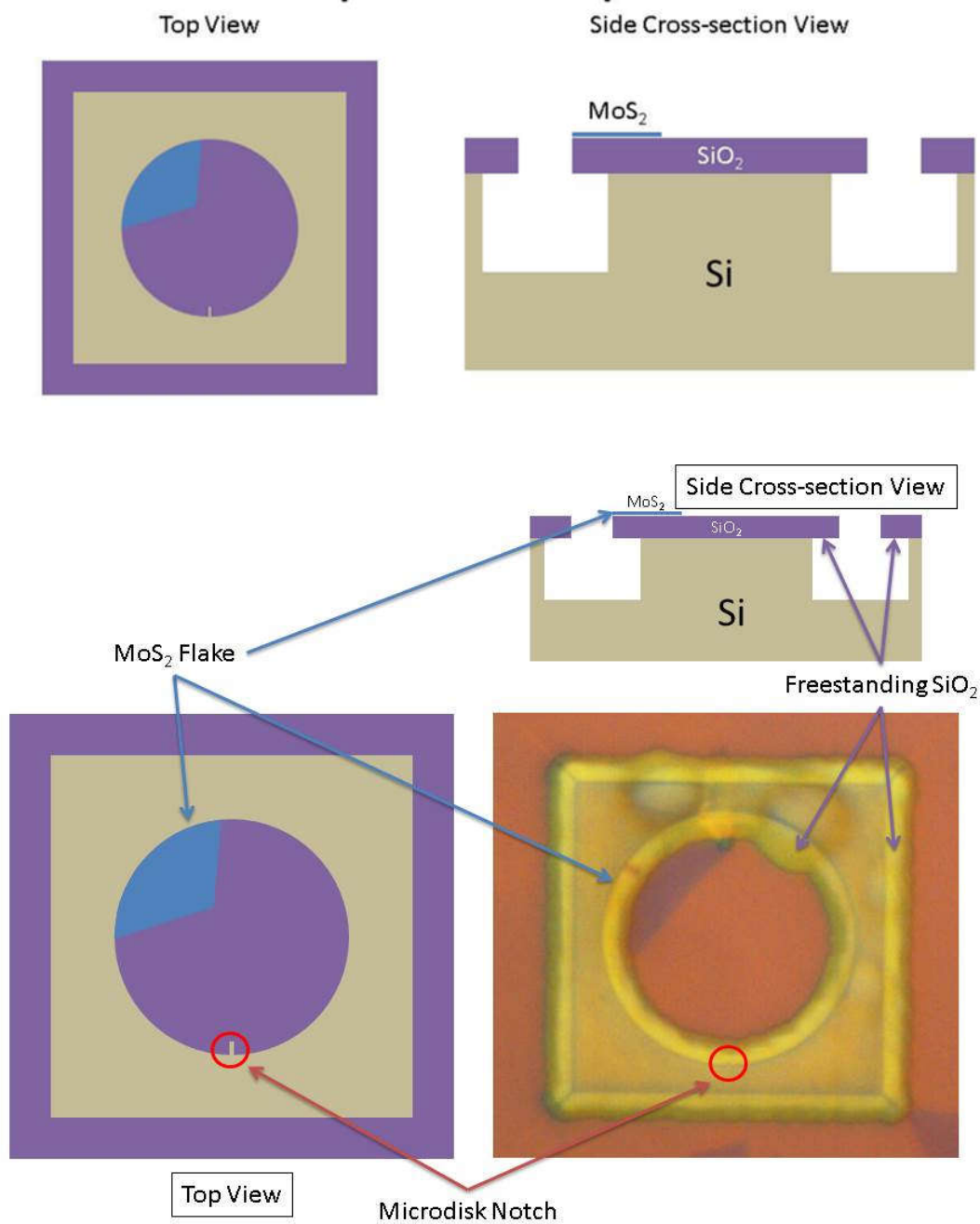
- 1 Chan, G. H., Zhao, J., Schatz, G. C. & Duyne, R. P. V. "Localized Surface Plasmon Resonance Spectroscopy of Triangular Aluminum Nanoparticles". *J. Phys. Chem. C* **112**, 13958 (2008).
- 2 Langhammer, C., Schwind, M., Kasemo, B. & Zorić, I. "Localized Surface Plasmon Resonances in Aluminum Nanodisks". *Nano Lett.* **8**, 1461 (2008).
- 3 Trunov, M. A., Umbrajkar, S. M., Schoenitz, M., Mang, J. T. & Dreizin, E. L. "Oxidation and Melting of Aluminum Nanopowders". *J. Phys. Chem. B* **110**, 13094 (2006).
- 4 Li, J., Mayer, J. W. & Colgan, E. G. "Oxidation and Protection in Copper and Copper Alloy Thin Films". *J. Appl. Phys.* **70**, 2820 (1991).
- 5 Chan, G. H., Zhao, J., Hicks, E. M., Schatz, G. C. & Van Duyne, R. P. "Plasmonic Properties of Copper Nanoparticles Fabricated by Nanosphere Lithography". *Nano Lett.* **7**, 1947 (2007).
- 6 Zhu, A. Y., Yi, F., Reed, J. C., Zhu, H. & Cubukcu, E. "Optoelectromechanical Multimodal Biosensor with Graphene Active Region". *Nano letters* **14**, 5641 (2014).
- 7 Guo, Q. *et al.* "Silicon-on-Glass Graphene-Functionalized Leaky Cavity Mode Nanophotonic Biosensor". *ACS Photonics* **1**, 221 (2014).
- 8 Homola, J. "Surface Plasmon Resonance Sensors for Detection of Chemical and Biological Species". *Chemical reviews* **108**, 462 (2008).
- 9 Gagliardi, G. L., Hans-Peter. in *Springer Series in Optical Sciences* Vol. 179 (ed William T. Rhodes) 527 (Springer, Berlin, 2014).
- 10 Wu, S. *et al.* "Monolayer Semiconductor Nanocavity Lasers with Ultralow Thresholds". *Nature* **520**, 69 (2015).
- 11 Teraoka, I. & Arnold, S. "Resonance Shifts of Counterpropagating Whispering-Gallery Modes: Degenerate Perturbation Theory and Application to Resonator Sensors with Axial Symmetry". *JOSA B* **26**, 1321 (2009).
- 12 Ye, Y. *et al.* Monolayer Excitonic Laser. *ArXiv e-prints* **1503**, 6141 (2015).

APPENDIX A: List of Publications

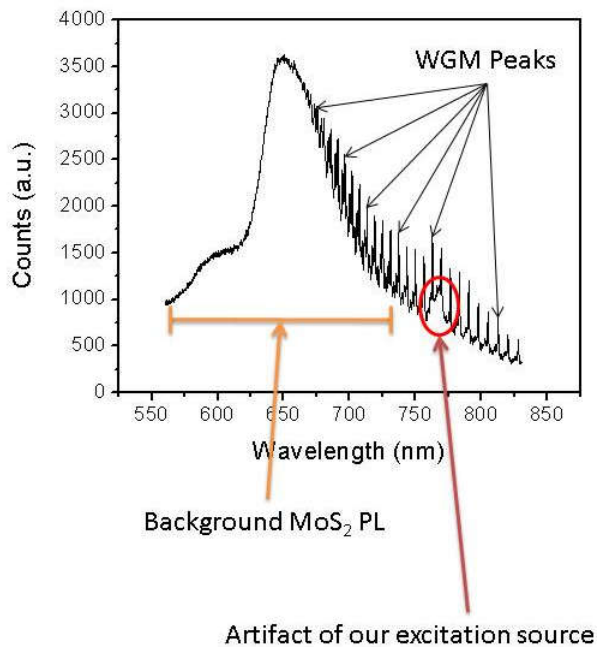
- 1 **J.C Reed**, S.C. Malek, F. Yi, C.H. Naylor, H. Zhu, S. Tongay, A.T.C. Johnson, and E. Cubukcu, “*Cavity-Coupled 2-Dimensional Semiconductors: A Photothermal Analysis*”, (In Preparation).
- 2 F.Yi, M. Ren, **J.C Reed**, H. Zhu, J. Hou, C.H. Naylor, A.T.C. Johnson, R. Agarwal, and E. Cubukcu, “*Optomechanical Enhancement of Doubly Resonant 2D Optical Nonlinearity*”, Nature Photonics, (Under Review).
- 3 **J.C Reed**, A. Y. Zhu, H. Zhu, F. Yi, and E. Cubukcu, “*Wavelength Tunable Microdisk Cavity Light Source with a Chemically Enhanced MoS₂ Emitter*”, Nano Letters, **15**, 1967, (2015).
- 4 D. Kuzum, H. Takano, E. Shim, **J.C Reed**, H. Juul, A. G. Richardson, J. de Vries, H. Bink, M. A. Dichter, T. H. Lucas, D. A. Coulter, E. Cubukcu, and B. Litt, “*Transparent and Flexible Low Noise Graphene Electrodes for Simultaneous Electrophysiology and Neuroimaging*”, Nature Communications, **5**, 5259 (2014).
- 5 Y. Zhu, F. Yi, **J.C Reed**, H. Zhu and E. Cubukcu. “*Optoelectromechanical Multimodal Biosensor with Graphene Active Region*”, Nano Letters, **14**, 5641 (2014).
- 6 Q. Guo, H. Zhu, F. Liu, A. Y. Zhu, **J.C Reed**, H. Zhu, F. Yi and E. Cubukcu. “*Silicon-on-Glass Graphene-Functionalized Leaky Cavity Mode Nanophotonic Biosensor*”, ACS Photonics, **1**, 221 (2014).
- 7 Y. Zhu, F. Yi, **J.C Reed** and E. Cubukcu. “*Cavity-Enhanced Mid-Infrared Absorption in Perforated Graphene*”, Journal of Nanophotonics, **8**, 083888 (2014).
- 8 F. Yi, H. Zhu, **J.C Reed**, A. Y. Zhu and E. Cubukcu. “*Thermoplasmonic Membrane-Based Infrared Detector*”, IEEE Photonics Technology Letters, **26**, 1041 (2014).
- 9 F. Yi, E. Shim, A. Y. Zhu, H. Zhu, **J.C Reed** and E. Cubukcu. “*Voltage Tuning of Plasmonic Absorbers by Indium Tin Oxide*”, Applied Physics Letters, **102**, 221102 (2013).
- 10 F. Yi, H. Zhu, **J.C Reed** and E. Cubukcu, “*Plasmonically Enhanced Thermomechanical Detection of Infrared Radiation*”, Nano Letters, **13**, 1638 (2013).
- 11 **J.C Reed**, H. Zhu, A.Y. Zhu, C. Li, and E. Cubukcu, “*Graphene-Enabled Silver Nanoantenna Sensors*”, Nano Letters, **12**, 4090, (2012).

APPENDIX B: Catalog of Large-Radius MoS₂-Coupled Microdisk Samples

Sample Description



Sample Spectra



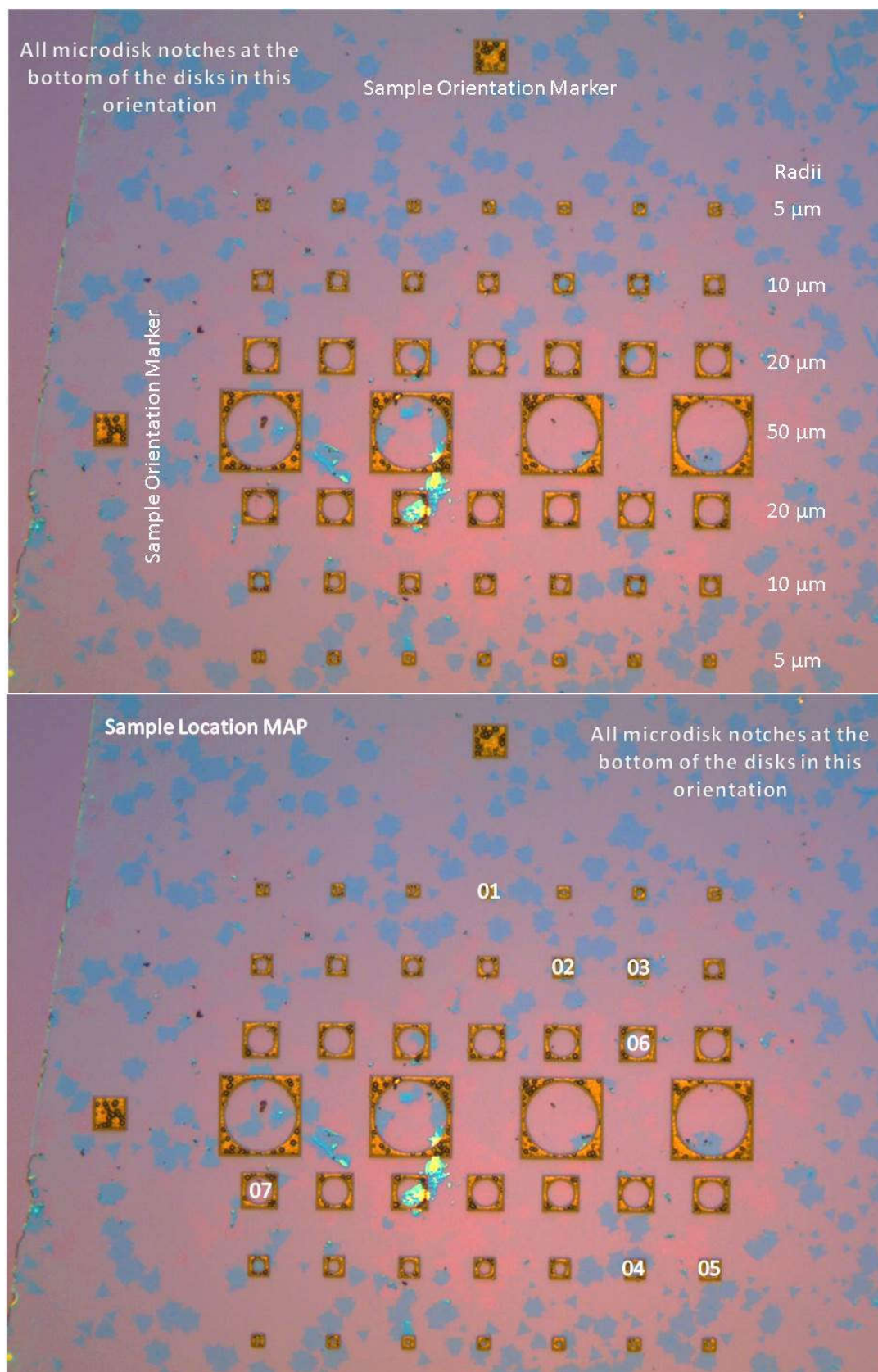
- This spectra was taken from spatially isolating the notch area and spectrally filtering the excitation source
- MoS_2 is illuminated on the opposite end of the microdisk
 - Some samples may have MoS_2 flakes that are not perfectly opposite to the notch

Notes

- The best performance is when all of the MoS_2 on the disk is excited
- Excitation of only a portion of the MoS_2 leads to absorption by the unexcited material and damped WGMs around the main MoS_2 PL peak
- Performance can also vary between samples depending on the PL efficiency of the specific MoS_2 flake
 - Performance i.e. contrast between PL and WGM peaks

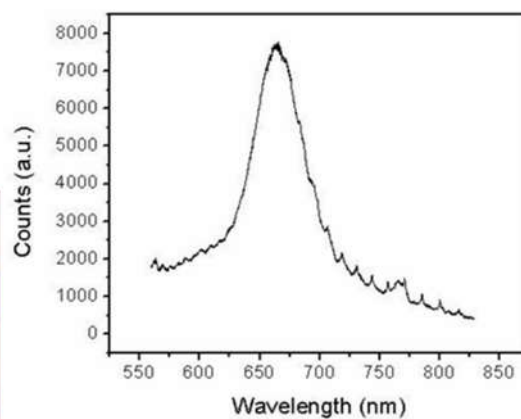
Chip 1





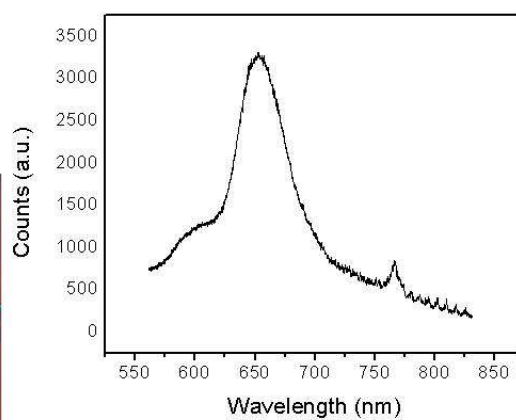
ID - jcr4-4-r5-01

Sample 01
5 μm Radius



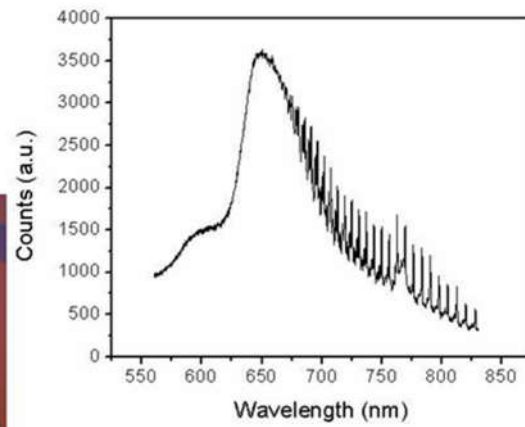
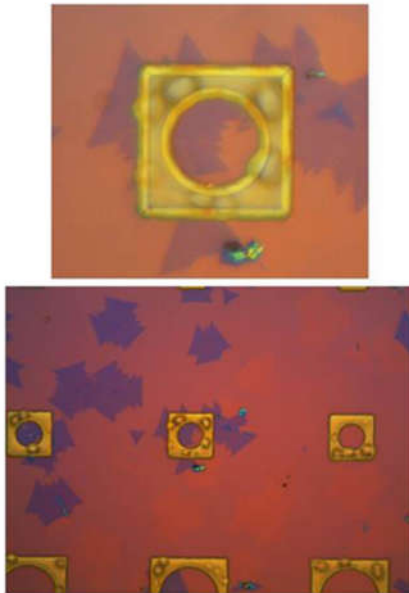
ID - jcr4-4-r10-01

Sample 02
10 μm Radius



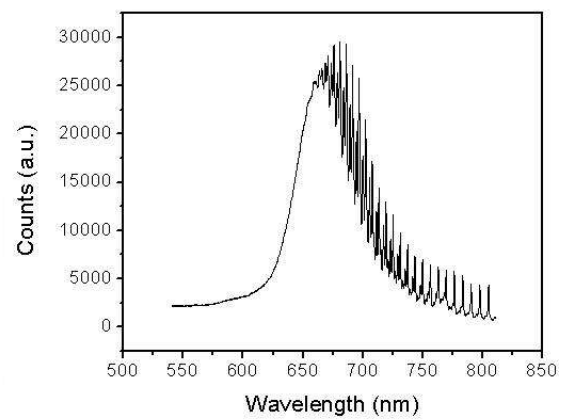
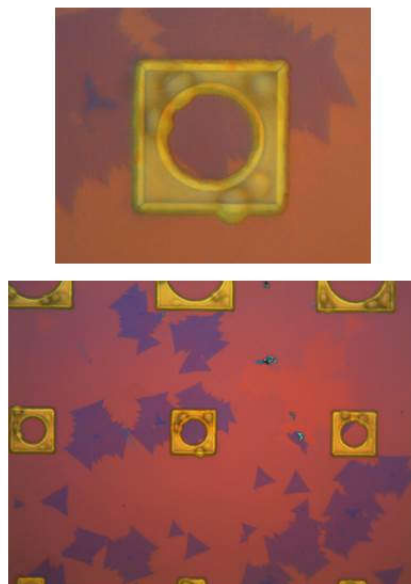
ID - jcr4-4-r10-02

Sample 03
10 μm Radius



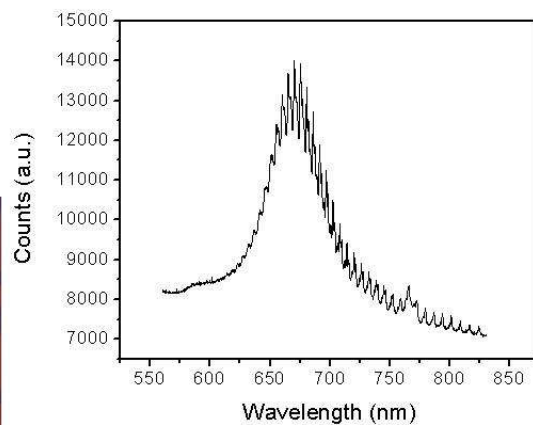
ID - jcr4-4-r10-03

Sample 04
10 μm Radius



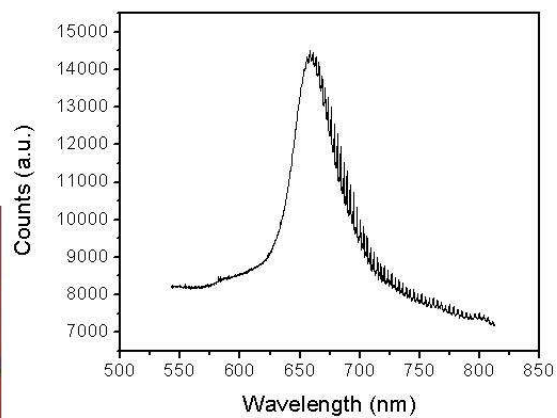
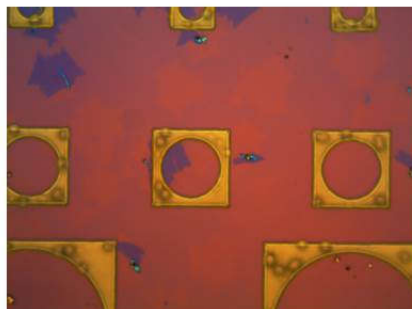
ID - jcr4-4-r10-04

Sample 05
10 μm Radius



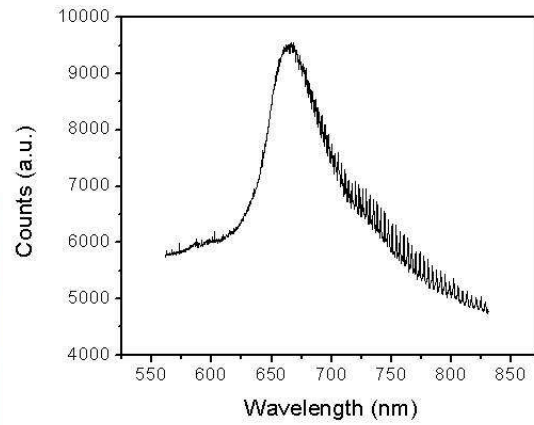
ID - jcr4-4-r20-01

Sample 06
20 μm Radius

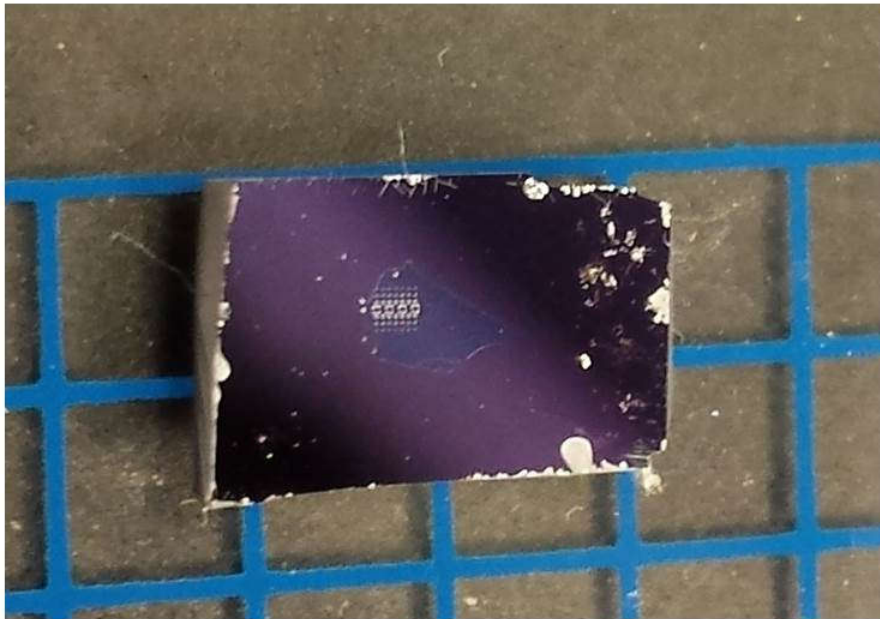


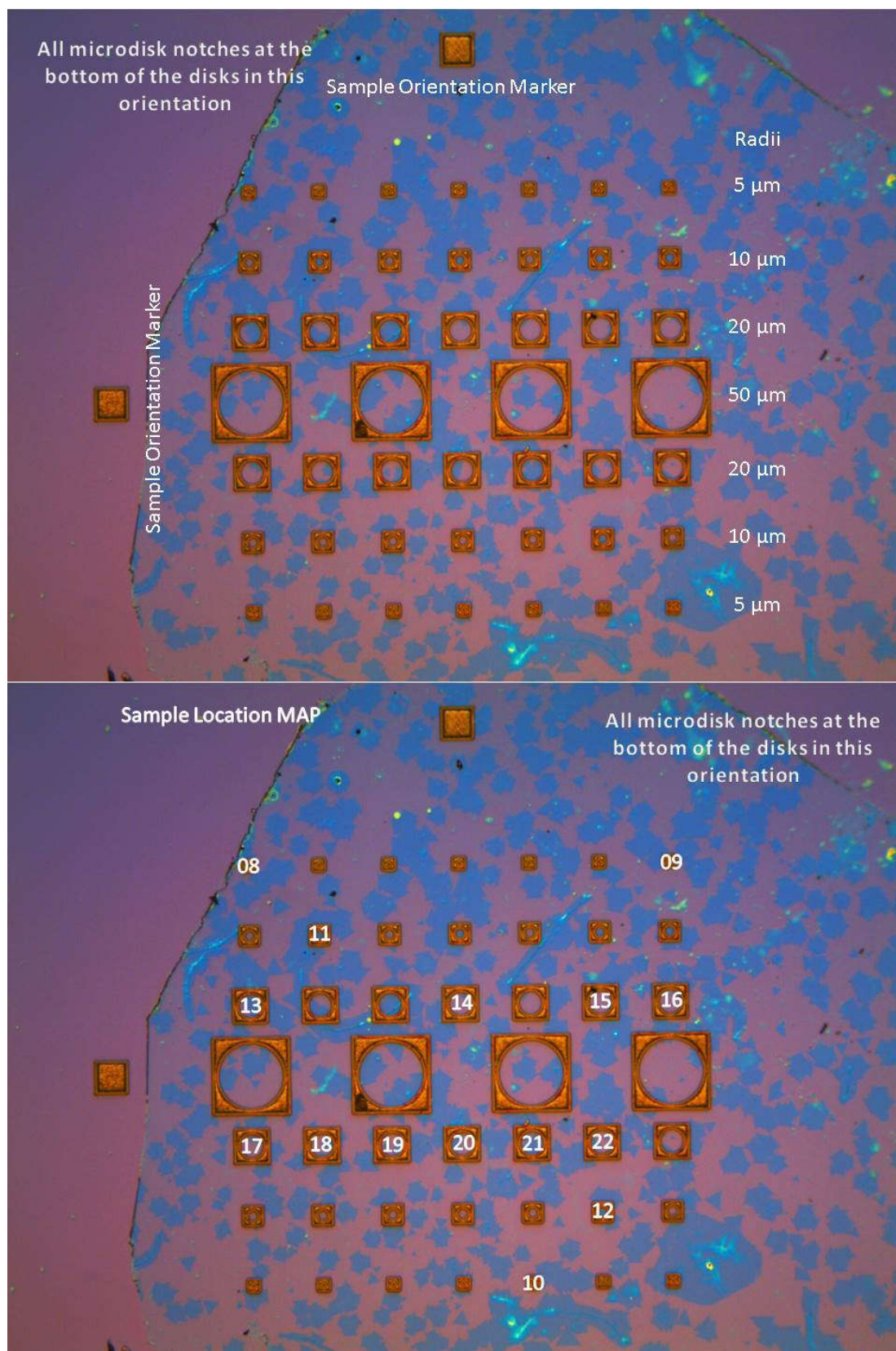
ID - jcr4-4-r20-02

Sample 07
20 μm Radius



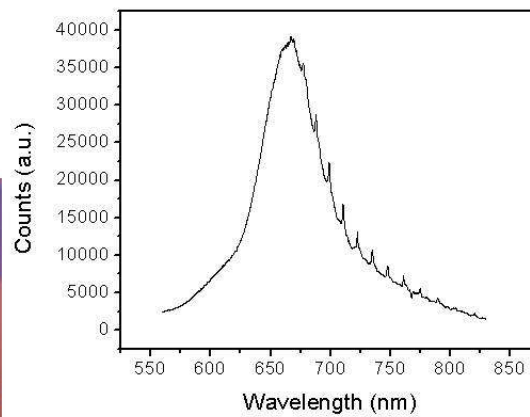
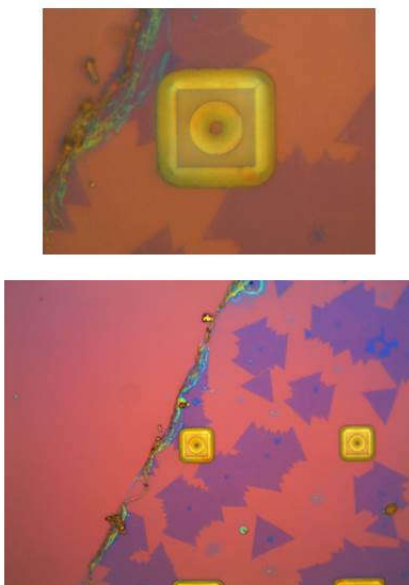
Chip 2





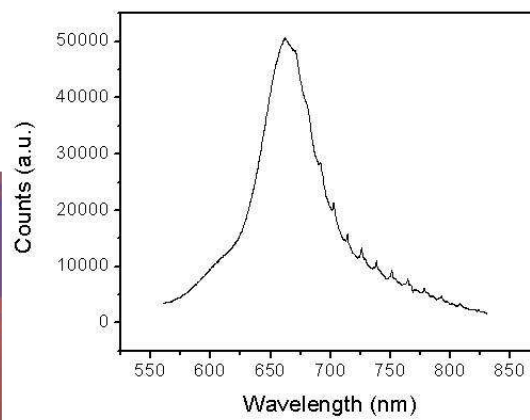
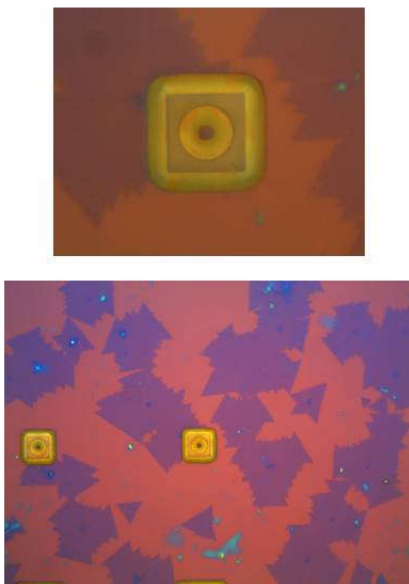
ID – jcr4-2-r5-01

Sample 08
5 μm Radius



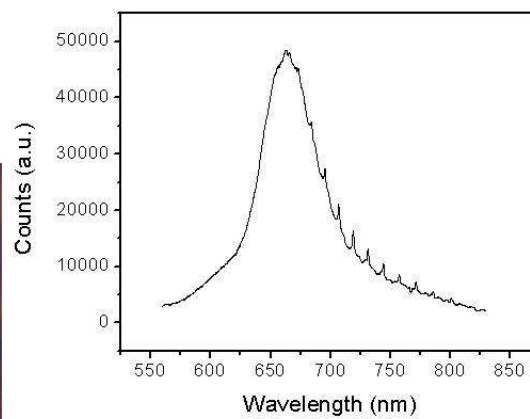
ID – jcr4-2-r5-02

Sample 09
5 μm Radius



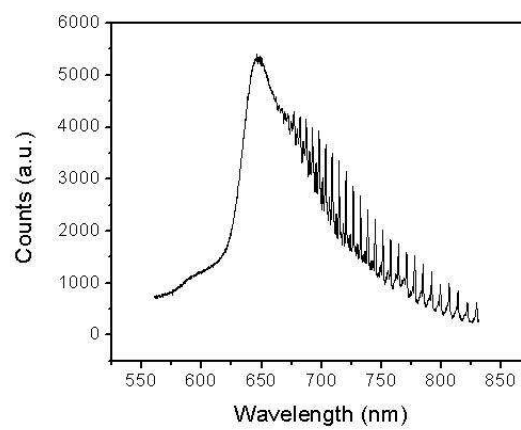
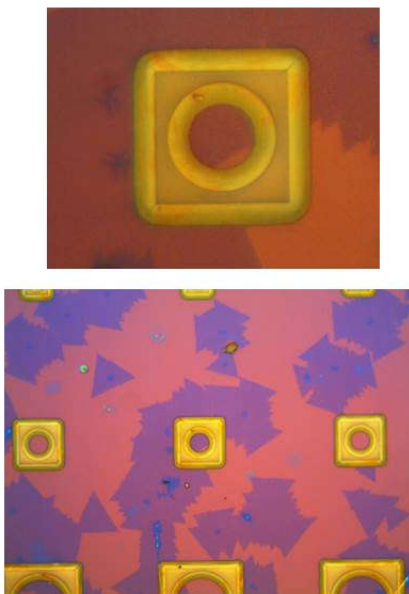
ID – jcr4-2-r5-03

Sample 10
5 μm Radius



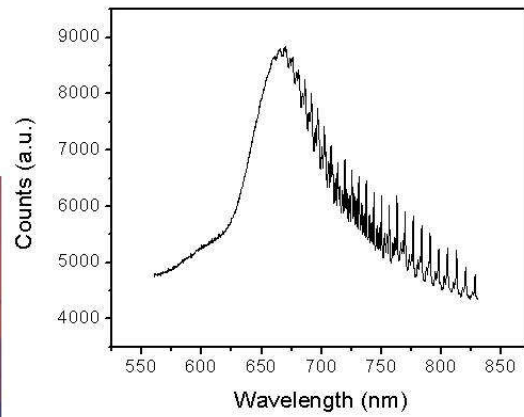
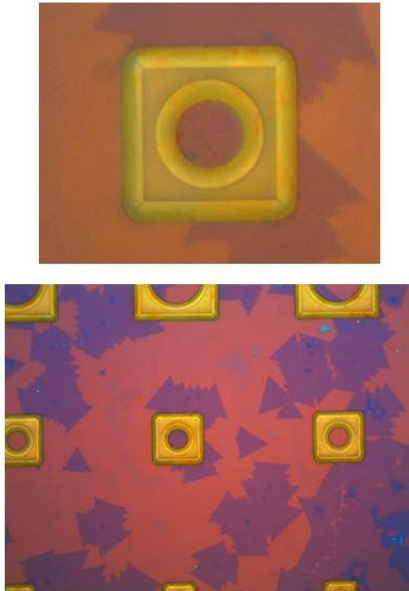
ID – jcr4-2-r10-01

Sample 11
10 μm Radius



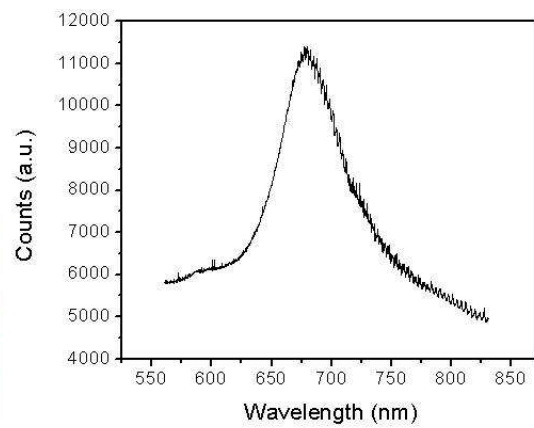
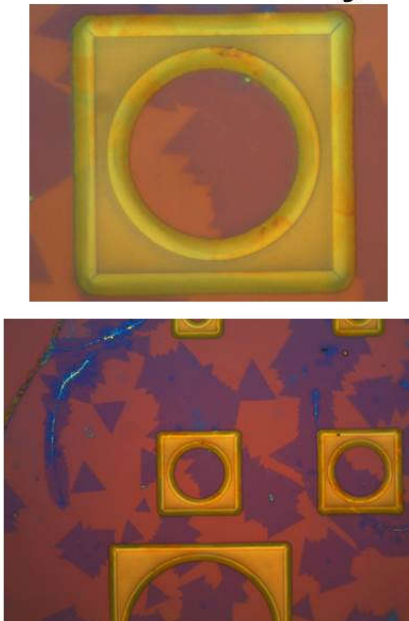
ID – jcr4-2-r10-02

Sample 12
10 μm Radius



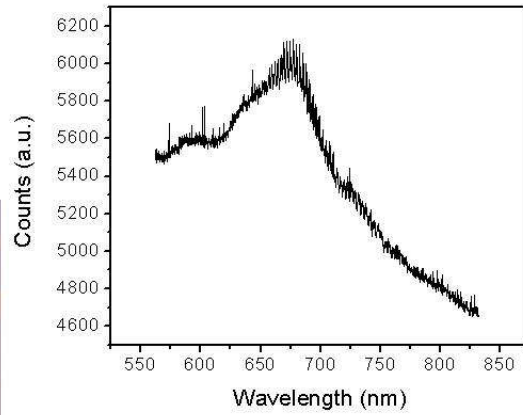
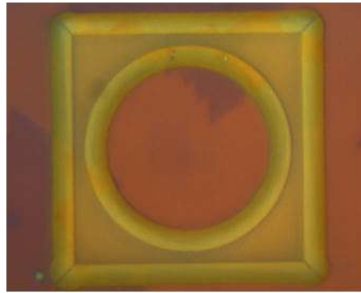
ID – jcr4-2-r20-01

Sample 13
20 μm Radius



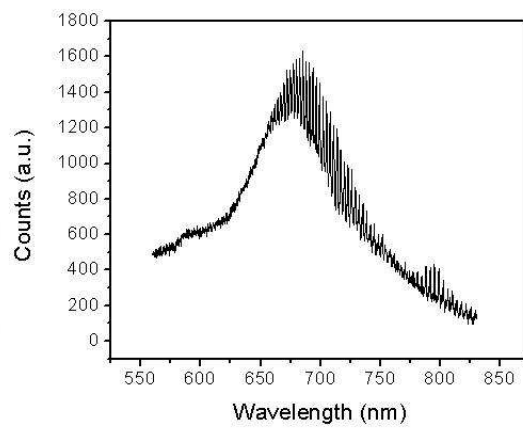
ID – jcr4-2-r20-02

Sample 14
20 μm Radius



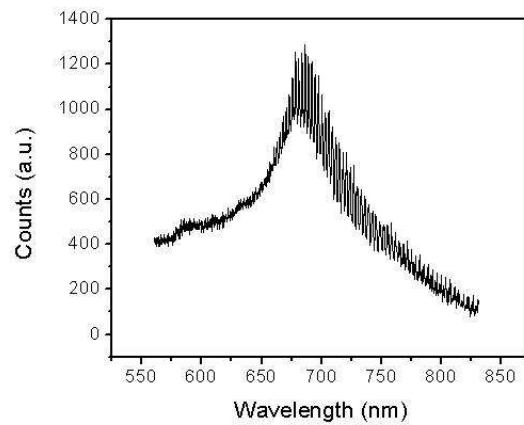
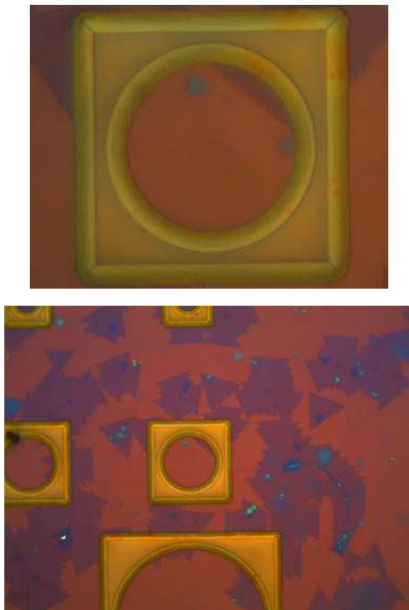
ID – jcr4-2-r20-03

Sample 15
20 μm Radius



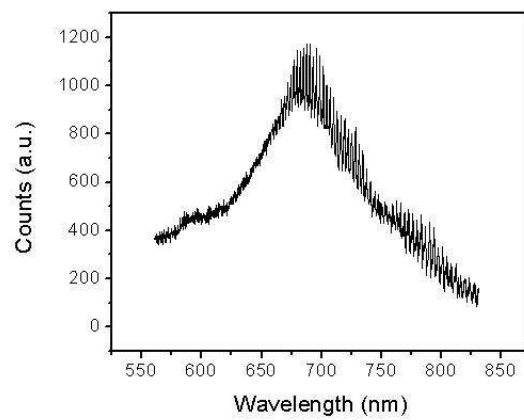
ID – jcr4-2-r20-04

Sample 16
20 μm Radius



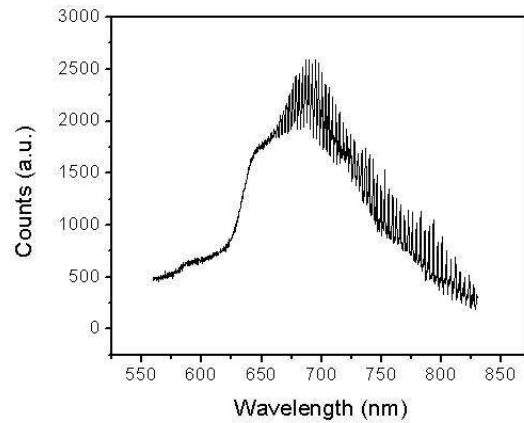
ID – jcr4-2-r20-05

Sample 17
20 μm Radius



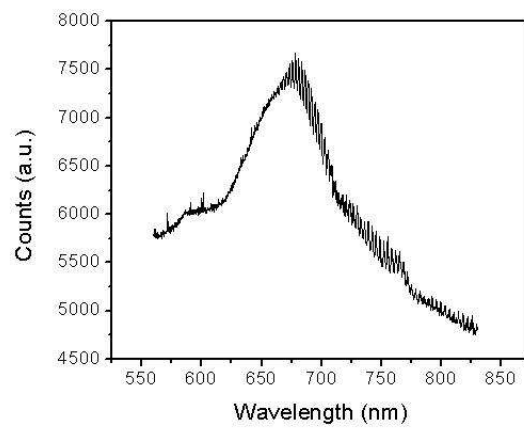
ID – jcr4-2-r20-06

Sample 18
20 μm Radius



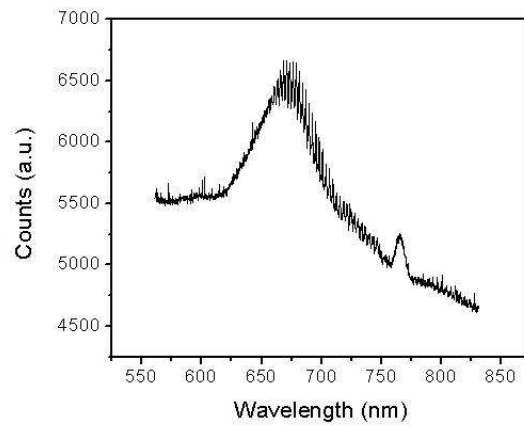
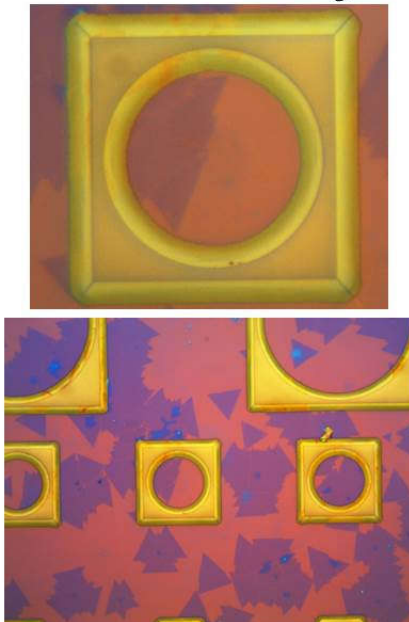
ID – jcr4-2-r20-07

Sample 19
20 μm Radius



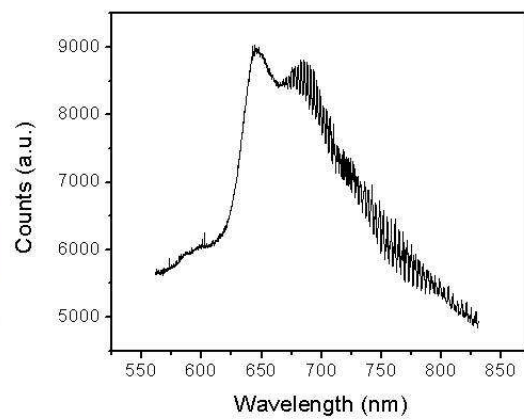
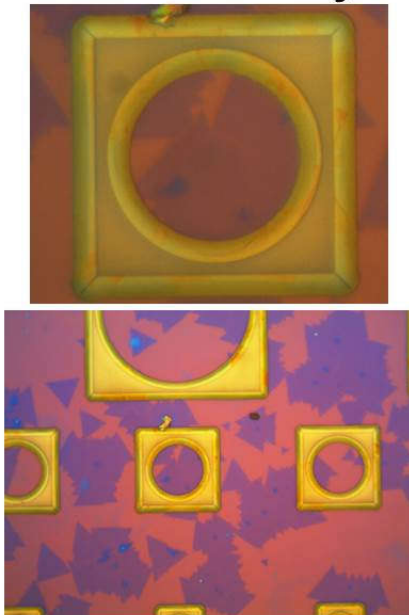
ID – jcr4-2-r20-08

Sample 20
20 μm Radius



ID – jcr4-2-r20-09

Sample 21
20 μm Radius



ID – jcr4-2-r20-10

Sample 22
20 μm Radius

